Novel Tree-Based Algorithms for Computational Electromagnetics

by

Jonatan Aronsson

A Thesis submitted to the Faculty of Graduate Studies of
The University of Manitoba
in partial fulfillment of the requirements of the degree of

Doctor of Philosophy

Department of Electrical and Computer Engineering
University of Manitoba
Winnipeg, Manitoba, Canada

Abstract

Tree-based methods have wide applications for solving large-scale problems in electromagnetics, astrophysics, quantum chemistry, fluid mechanics, acoustics, and many more areas. This thesis focuses on their applicability for solving large-scale problems in electromagnetics. The Barnes-Hut (BH) algorithm and the Fast Multipole Method (FMM) are introduced along with a survey of important previous work. The required theory for applying those methods to problems in electromagnetics is presented with particular emphasis on the capacitance extraction problem and broadband full-wave scattering.

A novel single source approximation is introduced for approximating clusters of electrostatic sources in multi-layered media. The approximation is derived by matching the spectra of the field in the vicinity of the stationary phase point. Combined with the BH algorithm, a new algorithm is shown to be an efficient method for evaluating electrostatic fields in multilayered media. Specifically, the new BH algorithm is well suited for fast capacitance extraction.

The BH algorithm is also adapted to the scalar Helmholtz kernel by using the same methodology to derive an accurate single source approximation. The result is a fast algorithm that is suitable for accelerating the solution of the Electric Field Integral Equation (EFIE) for electrically small structures.

Finally, a new version of FMM is presented that is stable and efficient from the low frequency regime to mid-range frequencies. By applying analytical derivatives to the field expansions at the observation points, the proposed method can rapidly evaluate vectorial kernels that arise in the FMM-accelerated solution of EFIE, the Magnetic Field Integral Equation (MFIE), and the Combined Field Integral Equation (CFIE).

Acknowledgements

I would like to thank my advisor, Dr. Vladimir Okhmatovski, for his support, guidance, advice, and encouragement during my Ph.D. studies. He encouraged me to enter the Ph.D. program, introduced me to the realm of computational electromagnetics and numerous challenging research problems, provided me with opportunities to collaborate with other researchers, and has taught me to become a better researcher. It has been a privilege to work under Dr. Vladimir Okhmaktovski and I can not thank him enough.

I would also like to express my appreciation for my Ph.D. committee: Dr. Joe LoVetri, Dr. Parimala Thulasiraman, and Dr. Shanker Balasubramaniam for their efforts in the evaluation of this work.

I would like to thank my colleagues and collaborators: Dr. Ian Jeffrey, Martin Cwikla, Dr. Lotfollah Shafai, Mohammad Shafieipour, Khalid Butt, and Dr. Mohammad Al-Qedra for their support and the time spent in discussing my research.

I also wish to thank my employer, the University of Manitoba, for providing me with the flexibility to pursue the Ph.D. degree.

Finally, I would like to thank my wife, Alissa, and my children, Anna and Isaac. They are my greatest source of support.

Author's Publications

The author contributed to the following publications while working towards the Ph.D. degree.

Articles in International Journals

- M. Shafieipour, I. Jeffrey, J. Aronsson, and V. Okhmatovski, On the Equivalence of RWG Method of Moments and Locally Corrected Nyström Method for Solution of the Electric Field Integral Equation, IEEE Transactions on Antennas and Propagation, Submitted

- I. Jeffrey, J. Aronsson, M. Shafieipour, and V. Okhmatovski, Error Controllable Solutions of Large Scale Problems in Elecromagnetics: MLFMA Accelerated Locally Corrected Nyström Solutions of CFIE in 3D, IEEE Antennas and Propagation Magazine, In Print

- V. Okhmatovski, J. Aronsson, and L. Shafai, A Well-Conditioned Non-Iterative Approach to Solution of the Inverse Problem, IEEE Transactions on Antennas and Propagation, vol. 60, no. 5, pp. 2418-2430, May 2012

- J. Aronsson, and V. Okhmatovski, Vectorial Low-Frequency MLFMA for the Combined Field Integral Equation, IEEE Antennas and Wireless Propagation Letters, vol. 10, pp. 532-535, 2011

- M. Al-Qedra, J. Aronsson, and V. Okhmatovski, A Novel Skin-Effect Based Surface Impedance Formulation for Broadband Modeling of 3-D Interconnects With Electric Field Integral Equation, IEEE Transactions on Microwave Theory and Techniques, vol. 58, no. 12, pp. 3872-3881, 2010

- A. Ashtari, S. Noghanian, A. Sabouni, J. Aronsson, G. Thomas and S. Pistorius, Using a priori Information for Regularization in Breast Mi-

crowave Image Reconstructional, IEEE Transactions on Biomedical Engineering, vol. 57, no. 9, pp. 2197-2208, 2010

- M. Cwikla, J. Aronsson, and V. Okhmatovski, Low-Frequency MLFMA on Graphics Processors, IEEE Antennas and Wireless Propagation Letters, vol. 9, 2010

- M. Al-Qedra, J. Aronsson, and V. Okhmatovski, Surface Integral Equation Formulation for Inductance Extraction in 3-D Interconnects, IEEE Microwave and Wireless Components Letters, vol. 20, pp. 250-252, 2010

- J. Aronsson, K. Butt, I. Jeffrey, and V. Okhmatovski, The Barnes-Hut Hierarchical Center-of-Charge Approximation for Fast Capacitance Extraction in Multilayered Media, IEEE Transactions on Microwave Theory and Techniques, vol. 58, pp. 1175-1188, 2010

- J. Aronsson, I. Jeffrey, and V. Okhmatovski, Generalization of the Barnes-Hut Algorithm for the Helmholtz Equation in Three Dimensions, IEEE Antennas and Wireless Propagation Letters, vol. 8, pp. 425-428, 2009

Articles in Conferences Proceedings

- J. Aronsson, M. Shafieipour, and V. Okhmatovski, Solution of Large Multiscale EMC Problems with Method of Moments Accelerated via Low-Frequency MLFMA, Proceedings of the IEEE International Symposium on Electromagnetic Compatibility, Aug 14-19, 2011, pp. 260-263

- J. Aronsson and V. Okhmatovski, "Comparison of Numerical Approaches to the Evaluation of Veselago Lens' Green's Function," Proceedings of the IEEE Symposium on Antennas and Propagation, Juy 3-8, 2011, pp. 1519-1521

- J. Aronsson, and V. Okhmatovski, Fast electromagnetic analysis of multiscale models with MLFMA utilizing spherical basis functions, Proceed-

ings of the 5th European Conference on Antennas and Propagation, Rome, Italy, April 11-15, 2011, pp. 3359-3362

- M. Al-Qedra, J. Aronsson, and V. Okhmatovski, A Novel Broadband Boundary Element Approach for RL-Extraction in Lossy 3D Interconnects, Proceedings of the 2010 IEEE 14th Workshop on Signal Propagation on Interconnects, May 9-12, 2010, pp. 41-42

- K. Butt, J. Aronsson, and V. Okhmatovski, Generalization of the Barnes-Hut Algorithm for Rapid Capacitance Extraction in Interconnects Embedded in Lossy Multilayered Media, Proceedings of the 2010 IEEE 14th Workshop on Signal Propagation on Interconnects, May 9-12, 2010, pp. 43-44

Conferences Abstracts

- J. Aronsson, F. Ling, and V. Okhmatovski, "Properties of Calderon Multiplicative Preconditioner Applied to Michalski-Zheng's Mixed Potential Integral Equation Formulation with Multilayered Medium Kernel," IEEE Symposium on Antennas and Propagation and URSI Radio Science Meeting, July 3-8, 2011

- V. Okhmatovski, J. Aronsson, and L. Shafai, Elimination of Inverse Problem Ill-Posedness in the Media Exhibiting Focusing Properties," IEEE Symposium on Antennas and Propagation and URSI Radio Science Meeting, July 3-8, 2011

- J. Aronsson, M. Cwikla, F. Ling, V. Okhmatovski, Implementing the Multi-level Fast Multipole Algorithm on Graphics Processors, IEEE Symposium on Antennas and Propagation and URSI Radio Science Meeting, Toronto, Canada, July 11-17, 2010

- J. Aronsson, I. Jeffrey, and V. Okhmatovski, Generalization of the Barnes-Hut Algorithm for the Helmholtz Equation in Three Dimensions, Progress In Electromagnetics Research Symposium, Moscow, Russia, Aug 18-21, 2009

Contributions

Synopsis of Scientific Contributions in This Thesis

The following novel research results are presented in this thesis.

- The Barnes-Hut Algorithm is extended to the electrostatic kernel in multi-layered dielectric media.
- The Barnes-Hut Algorithm is extended to the Helmholtz kernel.
- A new version of the Fast Multipole Method that is efficient for the evaluation of vectorial full-wave interactions from electrostatics to the high frequency regime.

Author's Contributions to Research Results included in this Thesis

Since a majority of the author's work was conducted in collaboration with other researchers, the author's own contributions are described below.

Chapter 3: The Barnes-Hut Hierarchical Center-of-Charge Approximation for Fast Capacitance Extraction in Multilayered Media

The author derived and generalized the center-of-charge concept to arbitrary number of layers from a 3-layer case study provided by his supervisor, showed that the centers-of-charge can be hierarchical clustered in layered media and, thus, applicable to the Barnes-Hut algorithm, wrote all prototypes, validated the method, and implemented a computer code library with the method.

Chapter 5: Generalization of the Barnes-Hut Algorithm for the Helmholtz Equation in Three Dimensions

The author tested the theory, wrote all prototypes, and demonstrated the applicability of the method. The author also devised an efficient interpolation

scheme which is required in any practical implementations of the method. The author implemented both HF-FMM and LF-FMM in order to compare the proposed method against them.

Chapter 7: Vectorial Low-Frequency MLFMA for the Combined Field Integral Equation

The author proposed the method and derived and formulated all of the theory. The author also wrote an implementation LF-FMM which is stable to higher frequencies than previously reported in the literature. This implementation was extended with the new method by the author.

Author's Contributions to Research Results not included in This Thesis

In addition to the primary contributions, the author contributed to many more projects, some of which were published and some that are unpublished. Out of these contributions, the author made significant contributions to, in particular, the following three journal publications.

Accelerated Locally Corrected Nyström Solutions of CFIE in 3D

The author wrote the fully error-controllable distributed memory implementation of HF-FMM and integrated it into the Locally Corrected Nyström solver. The author also wrote the parallel domain decomposition code for the solver based on a variety of partitioning algorithms.

Low-Frequency MLFMA on Graphics Processors

The author proposed the topic and decomposed the algorithm in way that is suitable for parallelization on graphics processors. The author also implemented the tree data structure and devised numerically stable algorithms for

computing the LF-FMM expansions and special functions.

A Well-Conditioned Non-Iterative Approach to Solution of the Inverse Problem

The numerical prototypes were developed by the author and in particular, the author developed and studied several numerical techniques in order to model the Veselago lens accurately. The author contributed to the description of the theory.

Contents

List of Tables

List of Figures

Chapter 1

Introduction: Tree-based Algorithms

Many complex physical problems can be approached through N-body simulation. Electromagnetic scattering computed with method of moments is one example. Another example is electrostatic analysis applied to capacitance extraction [NW91]. Other important applications areas are astrophysical simulation of galaxies [Dub96], high-Reynolds number flow through the vortex method [LK01, MG05], simulation of non-Newtonian flows [YBZ04], and molecular dynamics [JCJ+92]. When solved in a straight-forward manner, the N-body problem requires $O(N^2)$ work per evaluation. Tree-based methods typically reduce this complexity to between $O(NlogN)$ and $O(N^{3/2})$, depending on the kernel and problem parameters. The most popular of these methods are the Barnes-Hut algorithm [BH86] and the Fast Multipole Method [GR87]. While the lower computational complexity is obtained by approximating groups of bodies by some form of physical or mathematical approximation, tree-based method can often be tuned to provide accuracy levels down to a computer's machine precision and thus give the same solution accuracy as the direct $O(N^2)$ summation method.

In this chapter, we will review previous research of tree-based algorithms

for computational electromagnetics and correlate those results with the contributions that are presented in the latter chapters of this thesis.

1.1 The Barnes-Hut Algorithm

The algorithm was proposed by Barnes and Hut [BH86] in 1986 for solving large-scale gravitational N-body problems. A similar algorithm was proposed independently by Appel in 1985 [App85]. The computational complexity is reduced to $O(NlogN)$ compared to $O(N^2)$ for the direct summation of all mutual force interactions, where N is the number of bodies. The algorithm has two phases. In the first phase the tree data structure is constructed by enclosing all bodies in a cube[1]. This cube is then hierarchically sub-divided into cubic sub-cells (oct-tree in three dimensions or quad-tree in two dimensions) until there is only one body per cube. This hierarchical subdivision is done adaptively so that regions with coarse distributions of bodies are refined to a coarse level of the tree whereas denser regions have finer refinement. The tree is then traversed bottom-up and a center-of-mass location and magnitude is computed for each cube in the tree. In the second phase, the potential or force is evaluated for each body as follows; the tree is traversed top-down and at each cube $d/r < \theta$ is evaluated, where d is the width of the cube, r is the distance from the center of the cube to the observation body, and θ is the *opening angle parameter* which controls the trade-off between error and computational cost. If $d/r < \theta$ holds, the potential is computed by evaluating the center-of-mass at the cube and the traversal is terminated. Otherwise, the tree is recursively traversed to all of its children where the test is repeated at each child. The complexity is $O(NlogN)$ when θ is sufficiently large, but deteriorates when θ approaches zero in exchange for better approximation error with $\theta = 0$ being equivalent to direct summation.

[1] We use node(s), box(es), and cube(s) interchangeably to refer to part(s) of the tree data structure.

In the years following the original publication, many improvement and optimizations where proposed, including periodic boundary conditions [HBS91, Bou88] where the algorithm is combined with the Particle Mesh Ewald method [Ewa21], error control heuristics [JP89, BH89], higher-order approximations by adding multipole moments to the center-of-mass [BCPB90] or using expansions [GR87], and parallelization [HB87, MH89]. In 1994, Salmon and Warren [SW94] examined the worst-case error in greater detail and showed that the standard acceptance criteria may lead to either unacceptable errors or high computational costs in gravitational problems. They also showed that using additional multipole terms in the force evaluations outperforms the standard center-of-mass approximation when a fixed error bound is required. The conclusions in [SW94] supported the notion that the Fast Multipole Method may be a better choice when the error must be controllable. Much of the important work published from the early 90's until today have been focused on more efficient parallelizations schemes and their applicability to various hardware as well as improvements to the tree data structure.

While the tree data structure is important to the algorithm, the computational time for constructing the tree is generally negligible compared to other parts of the algorithm when it is applied to practical applications. However, some proposed modifications to the tree structure may significantly improve the overall complexity of the algorithm and most notable are binary trees and k-means clustered trees [MG05]. Binary tree have been shown to be efficient for certain application when level-skipping is utilized [WPM+02]. Instead of using a spatial oct-tree, the k-means clustering approach hierarchically clusters the bodies in a way that minimizes the approximation error for each cluster and yields better separation between the clusters compared to the oct-tree. The cost of building the tree is higher for k-means clustering in exchange for more efficient evaluation in the second phase of the algorithm. Overall, k-mean clustering have been shown to significantly improve the computational efficiency for practical datasets [AL08, MG05].

In order to solve many important large-scale problems, parallelized versions of the algorithms are needed. Thus, research into efficient parallelization has been very active since the late 1980's [HB87, MH89] until today. Today's state-of-the-art parallel implementation have tuned to run on up to 294,912 compute cores while simulating 2 billion moving bodies [WSH+12]. Implementations have been adapted to several hardware architectures, including, vector processors [Mak90], shared memory [BAD01], distributed memory [WS92, WS93, Dub96], hybrid shared-distributed memory [SAG11], graphics processors [HNY+09, BGPZ12], and custom-made hardware [IMES90, MTES94, KFM99]. The distributed memory parallelization algorithms typically work by first partitioning the bodies across the processors, and then generating a *locally essential tree* at each processor which is the union of the part of the tree containing the local bodies and the remote tree nodes that are required for evaluating the tree. Two important partitioning algorithms are the *orthogonal recursive bisection* method (ORB) [WS92] and *hashed oct-tree* (HOT) method [WS93]. The HOT method has been demonstrated to be more efficient and it partitions the space by converting every tree node and body into a *Morton key* based on its spatial location. This translates the three dimensional space (generalizable to N dimensions) into a one dimensional space-filling curve which is sequentially partitioned to create the distribution of tasks. Furthermore, since the Morton key can be computed in constant time and corresponds to a spatial location, it allows a parallel task to determine which task owns a particular part of the tree without requiring communication. The largest scale implementations use this method along with finer-scale shared memory parallelization [WSH+12].

Traditionally, the primary application area for the Barnes-Hut method has been astrophysics where it is used for gravitational force calculation and to model hydrodynamic flows to, for example, simulate galaxy formation, stellar collisions, and supernovae. Modeling of turbulent flows with the vortex model within the scope of fluid mechanics is another application area that benefits

from the adaptive nature of the Barnes-Hut algorithm. In computational electromagnetics, the algorithm has been applied to capacitance extraction and shown to be more efficient than the Fast Multipole Method [Jia04]. Its applicability to electromagnetics is extended in this thesis by the development of accurate capacitance extraction in multi-layered media (chapter 3) and low frequency scattering analysis (chapter 5).

In chapters 3 and 5, the center-of-mass concept is translated to the spectral domain where it is shown to be equivalent to matching the zeroth and first orders of the spectra at the stationary phase point [Che88]. This provides a new method for finding center-of-mass type approximations, in particular, Poisson's equation in multi-layered media (chapter 3) and the Helmholtz equation in free-space (chapter 5).

1.2 The Fast Multipole Method

The Fast Multipole Method (FMM) has achieved the greatest popularity among the tree-based algorithms and is widely used in computational engineering and science, for example, in electromagnetics [VCS03], molecular dynamics [BWS+95, GH02], quantum chemistry [WJGHG96, Dar00b], and fluid dynamics [TG08, CWD08]. It was first formulated for the Laplacian kernel in 2D by Greengard and Rokhlin in 1987 [GR87]. Extensions for the Laplacian kernel in 3D [GR88, SL91], the Helmholtz kernels in 2D [Rok90, EMRV92] and 3D [Rok93, CRW93], and other equations [DKG92, GGM93] followed in late the 1980s and early 1990s. In electromagnetics, the break-through came in 1995 when Song and Chew [SC95] proposed a $O(NlogN)$ version of FMM for the Helmholtz kernel in 3D and its extension to the Combined Field Integral Equation (CFIE), which is commonly referred to as the High-Frequency Fast Multipole Method (HF-FMM) or the Multi-Level Fast Multipole Algo-

rithm (MLFMA)[2]. HF-FMM is used to compute matrix-vector products in $O(NlogN)$ operations which arise from Method-of-Moment (MoM) discretizations of scattering problems. While HF-FMM is widely used, it is based on a far-field approximation which breaks down at low frequencies. Hence, the Low-Frequency Fast Multipole Method (LF-FMM) was developed [GHRW98] for efficient computation of scattering problems at low frequencies. FMM has also been developed for accelerating evaluation of transient wave fields generated by band-limited sources [ESM98, ESM99].

1.2.1 Brief Introduction

The idea behind FMM is to create a hierarchical tree data structure similar to the Barnes-Hut algorithm which at its root level encloses all sources or basis functions in the computational domain. An example of a two dimensional tree with 5 levels is illustrated in Figure 1.1. FMM requires that each box, B, in the tree contain two lists of boxes that are defined as follows.

- **Neighbor Set:** All boxes at the same level which are not *well-separated*[3] from B.
- **Interaction Set:** All boxes at the same level of the tree which are (i) well-separated from B and (ii) whose parents are not well-separated from the parent of B.

A formal description of the algorithm divided into six phases follows.

1. **Leaf-Node Aggregation:** For each box at the lowest level of the tree, construct an *outgoing expansion* that represents the field due to all sources or basis functions contained in the box. To define the region

[2]In this thesis, we use HF-FMM in chapters 1 thru 6, and MLFMA in chapter 7.

[3]In most implementations of FMM, a box is well-separated from B if it is at least one box width away from B. In this case, B's Neighbor Set becomes equivalent to its adjacent boxes or its "neighbors".

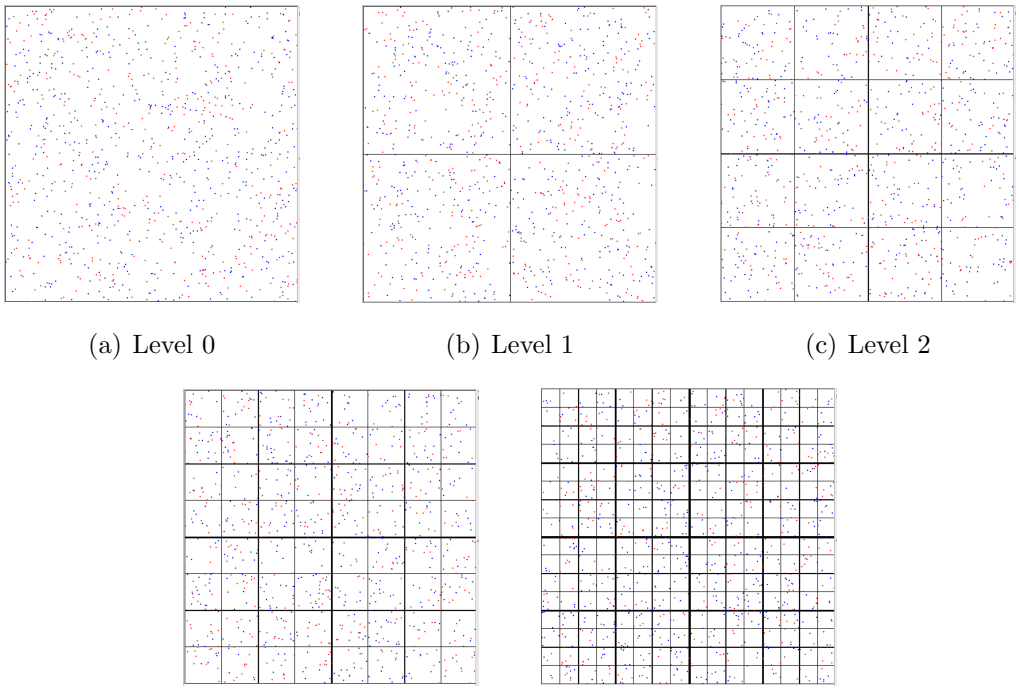

(a) Level 0 (b) Level 1 (c) Level 2

(d) Level 3 (e) Level 4

Figure 1.1: Example of a 5-level FMM tree data structure in two dimensions. Sources are illustrated as red points and observation locations as blue points. The root box (Level 0) is hierarchically subdivided until the desired resolution is reached at the leaf-level (Level 4).

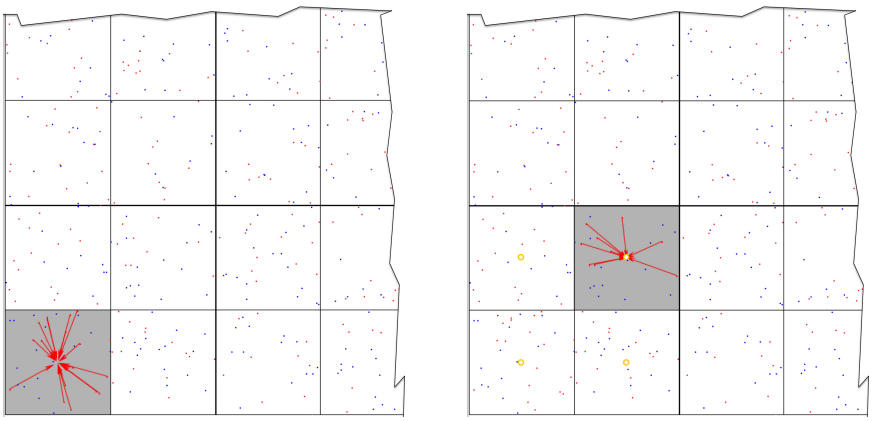

(a) (b)

Figure 1.2: Illustration of the leaf-level aggregation phase for two different boxes at level 4 (as shown in Figure 1.1). All sources are converted to outgoing expansions at each box.

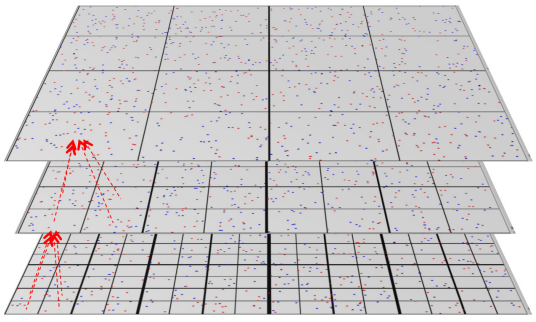

Figure 1.3: Illustration of the aggregation phase where outgoing expansions are first aggregated from level 4 to level 3 and then from level 3 to level 2.

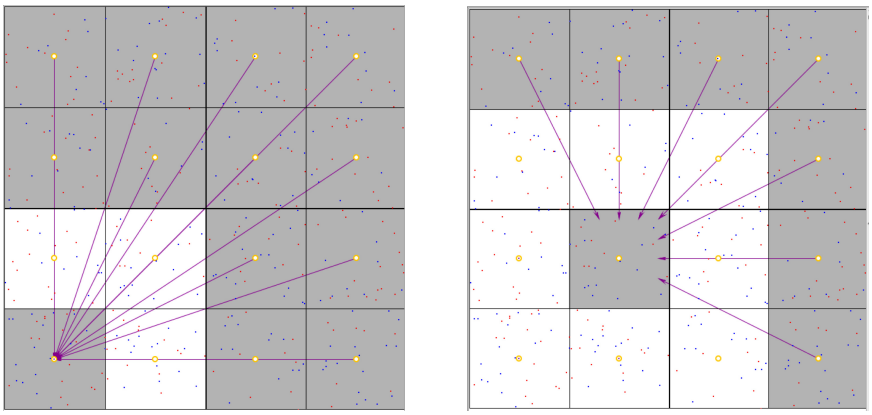

(a) (b)

Figure 1.4: Illustration of the translation phase for two different boxes at level 2 (as shown in Figure 1.1). Outgoing expansions in the interaction set are translated to an incoming expansion at each box.

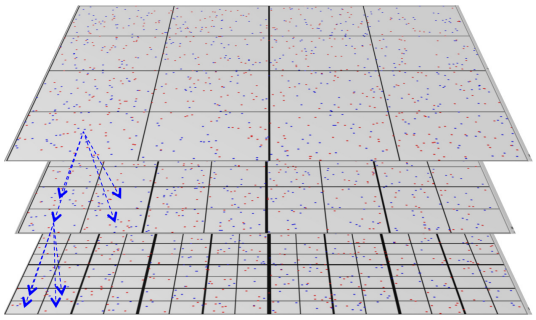

Figure 1.5: Illustration of the disaggregation phase. Incoming expansions are first disaggregated from level 2 to level 3 and then from level 3 to level 4.

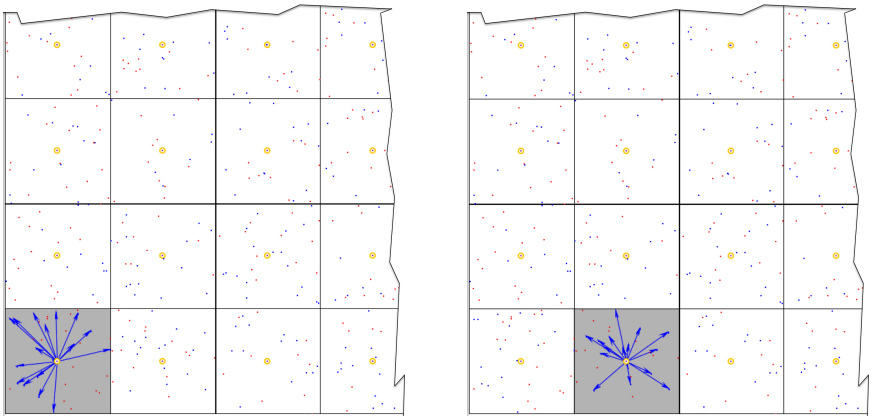

(a) (b)

Figure 1.6: Illustration of the leaf-level disaggregation phase for two different boxes at level 4 of the tree (as shown in Figure 1.1). Incoming expansions are evaluated at all observation locations in each box.

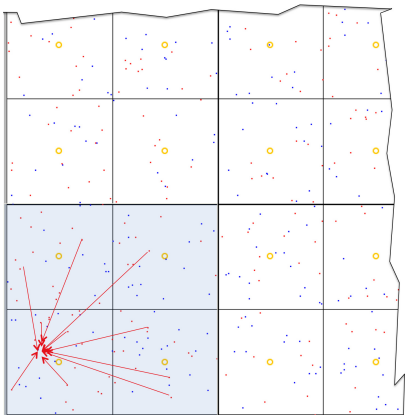

Figure 1.7: Illustration of the near-field summation phase for a single observation point at level 4 of the tree (as shown in Figure 1.1). Contributions from all sources in the near region are added to the field at the observations location by direct summation.

of validity of the outgoing expansion, the box under consideration is inscribed in a sphere (or circle in two dimensions). The outgoing expansion is then valid in the region exterior to the sphere. An illustration of this phase is shown in Figure 1.2.

2. **Aggregation:** This procedure is carried out level by level from the bottom up starting at the second lowest level. For each box, B, at level L, convert outgoing expansions at each of B's children to form outgoing expansions at B. An illustration of this phase is shown in Figure 1.3.

3. **Translation:** For each box at each level, convert all outgoing expansions in its interaction set to a incoming expansion. An illustration of this phase is shown in Figure 1.4.

4. **Disaggregation:** This procedure is carried out level by level from the top down. For each box, B, at level L, convert B's incoming expansions to incoming expansions at each of B's children at level $L+1$. An illustration of this phase is shown in Figure 1.5.

5. **Leaf-Node Disaggregation:** For each box, B, at the leaf level of the tree, evaluate B's incoming expansion at all observation locations inside B. The observation locations now contain contributions from all sources except those contained in its neighbor set. An illustration of this phase is shown in Figure 1.6.

6. **Near-Field Summation:** For each observation location, add contributions from all sources in its neighbor set. An illustration of this phase is shown in Figure 1.7.

1.2.2 The High-Frequency Fast Multipole Algorithm

The outgoing expansion in HF-FMM is the far-field signature function,

$$f_\infty(\hat{r}) = \lim_{r\to\infty} \frac{r f(\mathbf{r})}{e^{ikr}} \tag{1.1}$$

which is defined on the unit sphere and approximates the scalar field $f(\mathbf{r})$ in the far region, where $f(\mathbf{r})$ is governed by the Helmholtz equation. The $e^{-i\omega t}$ time convention is assumed here. $f_\infty(\hat{r})$ is sampled on a $N_\theta \times N_\phi$ grid on the unit sphere and stored at each box of the FMM tree, usually with $N_\phi = 2N_\theta$ or $N_\phi = 2(N_\theta - 1)$. The number of samples depends on the band-width of $f_\infty(\hat{r})$ and accuracy requirements. Since the band-width is dependent on the electrical size of a box, the number of samples per box is dependent on the level of the tree. In the aggregation phase, interpolation is used to transfer samples from boxes at the bottom levels of the tree to denser grids at higher levels of the tree. The interpolator must have a computational complexity no worse than $O(N_\theta N_\phi log(N_\theta N_\phi))$ in order to preserve the overall $O(NlogN)$ complexity[4]. Several interpolation schemes have been proposed, including expanding over spherical harmonics [CCG+06], Fourier series [Sar03], and local interpolators such as Legendre polynomials [SC00, EvdBG09]. Spherical harmonics based interpolator expand $f_\infty(\hat{r})$ over an orthonormal basis on the unit sphere by carrying out a combination of Fast Fourier Transforms (FFTs) along ϕ and a specialized one-dimensional FMM along θ [YR99]. The Fourier series based interpolator extends the unit sphere to $-\pi < \theta \leq +\pi, 0 < \phi \leq +2\pi$ by symmetry and use two-dimensional FFTs for the interpolation. While the previous two interpolators are fully error controllable to machine precision, local polynomial interpolators are only efficient when accuracies of approximately two digits are acceptable.

The incoming expansion is represented by an amplitude field, $f_0(\hat{\mathbf{r}})$, on the unit sphere which is sampled on a grid identical to the one used for $f_\infty(\hat{\mathbf{r}})$. $f_\infty(\hat{\mathbf{r}})$ is translated to form $f_0(\hat{\mathbf{r}})$,

$$f_0(\hat{\mathbf{r}}) = f_\infty(\hat{\mathbf{r}}) T_L(\hat{\mathbf{r}}, \mathbf{d}) \tag{1.2}$$

where $\mathbf{d}$ is the vector from the expansion center of $f_\infty(\hat{\mathbf{r}})$ to the expansion

[4]When applied to high-frequency scattering problems with surface discretization, the number of basis functions, N, is generally related to the electrical size of the scatter and $O(N) = O(N_\theta N_\phi)$.

center of $f_0(\hat{\mathbf{r}})$ and $T_L(\hat{\mathbf{r}}, \mathbf{d})$ is the Rokhlin translator function of degree L defined as follows.

$$T_L(\hat{\mathbf{r}}, \mathbf{d}) = \sum_{n=0}^{L} i^n (2n+1) h_n(kd) P_n(\hat{\mathbf{r}} \cdot \hat{\mathbf{d}}) \tag{1.3}$$

where h_n is the spherical Hankel function of the first kind of order n and P_n is the Legendre polynomial of degree n. Due to diagonal form of the translator $T_L(\hat{\mathbf{r}}, \mathbf{d})$ computing $f_0(\hat{\mathbf{r}})$ directly from Eqs. (1.2) and (1.3) requires only $O(N_\theta N_\phi L)$ operations. For many important problems, this results in $O(N^{3/2})$ complexity because the condition $O(N_\theta) = O(N_\phi) = O(L) = O(\sqrt{N})$ is valid at the top level of the tree. In Eq. (1.3), $\hat{\mathbf{r}}$ only enters into the calculation as $\hat{\mathbf{r}} \cdot \hat{\mathbf{d}}$ which is a function of the angle between $\hat{\mathbf{r}}$ and $\mathbf{d}$. Therefore, $T_L(\hat{\mathbf{r}}, \mathbf{d})$ can be computed in $O(N_\theta N_\phi)$ operations if it is precomputed for $O(L)$ angles and interpolated to the points on the grid. The interpolation of $T_L(\hat{\mathbf{r}}, \mathbf{d})$ have been studied in detail [BGS91, CJMS01, SC01, VC01, EG06b] and an efficient error controllable method is presented in [HS08]. The disaggregation is analogous to the aggregation and the same interpolation methods can be used. In the leaf-node disaggregation phase, the scalar field $f(\mathbf{r})$ is obtained at the observations points by integrating the amplitude field,

$$f(\mathbf{r}) \approx \int_S f_0(\hat{\mathbf{s}}) e^{ik\hat{\mathbf{s}}\cdot\mathbf{r}} dS(\hat{\mathbf{s}}) \tag{1.4}$$

An efficient scheme for evaluating electric and magnetic fields is presented in [CJMS01]. The corresponding vectorial far-field signature function, $\mathbf{F}_\infty(\hat{\mathbf{r}})$, is decomposed into its traverse components, $\mathbf{F}_\infty(\hat{\mathbf{r}}) = \hat{\theta} f_{\theta,\infty} + \hat{\phi} f_{\phi,\infty}$, and treated as scalar fields.

In a practical implementation of HF-FMM, the error in the solution comes from five sources: the Rokhlin translator, the choice of sample grid, the interpolator, the integration, and round-off errors. While several studies have investigated the total error in the solution and attempt to quantify it [KSC99, Dar00a, OC01, Nil04], there is no exact method for accurate estimation of the error. The existing semi-analytical methods either over-estimate the error or

are only accurate in the asymptotic cases. Other work has been focusing on the Rokhlin translator in isolation and several analytical or semi-analytical formulas for predicting L have been proposed [OC03a, CJMS01, HOC03, BPZ11], the so called excess bandwidth formula have gained the greatest popularity [CJMS01] even though it is inaccurate in many cases [DS09]. Local interpolators are a significant source of error in the disaggregation phase due to its inability to eliminate the high-order modes in the field and require careful analysis [OC03b, EG06a]. Finally, the inherent inaccuracies in the numerical implementation of many special mathematical functions often results in an error behavior which is dependent on implementation specific details. A more general method of controlling the error is by numerically searching and tabulating errors in the solution for various worst-case configurations and values of L, N_θ, and N_ϕ.

HF-FMM breaks down when the box width is less than approximately one wavelength[5]. Numerically, this breakdown is due to the exponential increase of the spherical Hankel function with increasing orders when its order exceeds its argument, which in turn leads to numerical cancellation in the integration (Eq. (1.4)). From a physical point-of-view, information about the evanescent waves is lost because only propagating waves are aggregated and therefore becomes inaccurate in the near-field region where evanescent waves are present. Reconstructing near-field behavior from far-field information is an inherently ill-conditioned problem.

1.2.3 The Low-Frequency Fast Multipole Algorithm

Due to the low frequency breakdown of HF-FMM, much work has been done towards development of LF-FMMs and several formulations have been demonstrated to be effective. Each formulation have advantages and disadvantages

[5]The breakdown of HF-FMM is dependent on accuracy. The breakdown occurs at approximately 0.3λ for 2 digits of accuracy and then increase rapidly for higher accuracies (e.g. 4λ for 6 digits and 12λ for 9 digits).

and a summary of important formulations follows.

One class of formulations are based on the spectral representation of the Green function which use both propagating and evanescent waves. Due to the properties of the spectral representation, the resulting expansions are directional and six unique expansions must be stored at each box and split into to $+x$, $-x$, $+y$, $-y$, $-z$, $+z$. Greengard and Huang [GHRW98] introduced this representation for a low frequency stable formulation that uses multipoles for storing the field expansions at each box and switches to the spectral representation in the translation. Jiang and Chew [JC04] proposed a method named Low Frequency Fast Inhomogeneous Plane Wave Algorithm (LF-FIPWA) that is also based on the spectral representation. To improve the efficiency when the box width becomes larger, the evanescent waves are partially extrapolated from the propagating waves. Once the box width becomes large enough the evanescent waves are completely absorbed into the propagating waves. LF-FIPWA was further improved in [WS05] by the use of a generalized Gaussian quadrature rule [YR98] for the evanescent part. Darve and Havé [DH04] developed a similar formulation that is based on the same direction dependent plane wave representation with a slightly different integration path. This class of methods are stable at both low and high frequencies, but require considerable memory overhead for storing six expansions at each box, and is therefore usually combined with HF-FMM.

Xuan et al. [XZAG04] proposed a broadband method called Uniform MLFMA which is based on a modified form of HF-FMM where the integration over θ on the unit sphere is shifted to the complex plane. Due to this shift the integration over θ is extended to $[-\pi + \alpha i, +\pi + \alpha i]$ and therefore additional quadrature points are required compared to HF-FMM. The Rokhlin translator is no longer known analytically and must be constructed numerically. Despite this additional overhead, the method is significantly more efficient than the directional formulations based on the spectral representation. However, it is difficult to control its error and it can only support low accuracy solution

[VGMO+04, WS05].

Bogaert et al. [BPO08] developed the Nondirective Stable Plane Wave Multilevel Fast Multipole Algorithm (NSPWMLFMA) which, like Uniform MLFMA, is based on the same underlaying formulation as HF-FMM. The integration path is shifted to the complex plane where the location of the path is determined by an analytic expression. Instead of sampling the plane waves on fixed grids like the previous formulations, their locations are determined numerically with the QR algorithm. While this leads to an error controllable representation, the interpolations in the aggregation and disaggregation phases must be carried out with dense matrices. Therefore, it quickly becomes inefficient when the box size increases and it must be combined with HF-FMM to remain efficient at all frequencies. A variation of the method was presented in [BO09a, BO09b] where the Green function is expanded over pseudo-spherical harmonics in a way that allows for sampling of plane waves on a uniform grid. FFTs are then used for the aggregation and disaggregation phases which significantly improve the asymptotic complexity. However, additional overhead is introduced because a denser grid is required at each box.

In [SH07, VGHS07], Shanker et al. developed a formulation based on Cartesian harmonics called Accelerated Cartesian Expansions (ACE). The field is expanded over Taylor series by using Cartesian tensors. ACE is efficient in the quasi-static regime but rapidly becomes inefficient at higher frequencies due to the difficulty in approximating oscillatory kernels with Taylor series. Its strength lies its simplicity and that it can relatively easily be adapted to many types of kernels. Combined with HF-FMM, it can be used for efficient broadband analysis [VHSV09, VSA09, VSV08].

The formulation that has been studied in the greatest detail, in particular in the mathematics community, is the classical LF-FMM based on partial-wave expansions which form a basis over elementary solutions to the three dimensional Helmholtz equation. These elementary solutions are expressed in terms of spherical harmonics and spherical Bessel and Hankel functions.

The expansions at each box is represented by $P^2 - 1$ coefficients and is said to be of order P. Aggregation, disaggregation, and translations are carried out by re-expanding the coefficients and requires the computation of so called *re-expansion coefficients*. Explicit expressions for the re-expansion coefficients can be obtained via *Clebsch-Gordan coefficients* [Ste61, AS64] or *Wigner 3-j symbols* [AS64, ED95] which leads to $O(P^6)$ operations for the re-expansion [ED95]. This can be improved to $O(P^5)$ by using symmetries and special properties [GD05]. While this is acceptable for sub-wavelength interactions, it quickly becomes impractical for higher frequencies where the expressions are also numerically unstable. Improved $O(P^4)$ schemes can be derived by computing the re-expansion coefficients via recurrence relations. When combined with HF-FMM [JC05, CCG+06, GD09], $O(P^4)$ and $O(P^5)$ are sufficient for efficient analysis with low-order basis functions when two or three digits of accuracy is sufficient. However, if higher accuracy is required or if it is not combined with HF-FMM, the complexity must to be improved to $O(P^3)$ or ideally, $O(P^2 logP)$ in order to maintain a computationally efficient implementation. The complexity can be reduced to $O(P^3)$ by rotating the spherical coordinate system and perform the translation along the z-axis followed by a second rotation to the original coordinate system. Due to symmetrical properties of the translation coefficients, $O(P^3)$ coefficients remain non-zero when the translation is carried out along the z-axis. This technique is called *point-and-shoot* and its main challenge is that the rotation suffers from numerical stability issues. An efficient recurrence relation for performing the rotation is presented in [GD05] but starts to break down around $P \approx 30$ when double precision arithmetic is used[6]. According to Greengard et al., recurrence relations of orders up to $P \approx 160$ have been implemented by their group and hints on their implementation were provided in [GG09][7]. Gimbutas and Greengard

[6]This was determine by our implementation of the method since its stability is not discussed in [GD05].

[7]We developed a recurrence relation based on those hints combined with well-known

[GG09] recently developed a novel method that is based on pseudo-spectral projections and numerically stable to beyond $P = 1000$. The recurrence relations are computationally more efficient than pseudo-spectral projections for values of P where they are stable. Though this formulation of LF-FMM can yield efficient implementations, it is complicated compared to the previous versions of LF-FMMs.

Chew recently derived a vectorial form of the elementary spherical basis and its corresponding addition theorem [Che07, Che08, LC10] which only requires two components of the full vectorial form of EFIE to be stored in memory or three components for a mixed potential form of EFIE [LCJQ12]. In previous work, three or four components were stored in memory, thus this method yields a memory saving of 25% or 33% depending on the formulation of the EFIE. In chapter 7 of this thesis, the vectorial form is extended to MFIE and CIFE in addition to EFIE. Furthermore, without any loss in efficiency, our formulation only requires one component to be stored in memory regardless of the vectorial form which is equivalent to an additional memory saving of 50% to 67% compared to Chew's vectorial formulation.

1.2.4 Parallelization of the Fast Multipole Method

Many parallelization strategies for FMM have been proposed for multiple hardware architectures, including distributed memory architectures [DJV+01, HAS02, KP05b], shared memory [OSVW99], hybrid shared and distributed memory [PPY+12], and graphics processors [CAO10]. Over the past decade, much research has been focusing on efficient load balancing for distributed memory architectures, primarily by exploring partitioning strategies for the hierarchical tree data structure and algorithmic refactoring to overlap computation with communication [KP05a, FO08a]. The partitioning strategies can

properties of the associated Legendre polynomials which appears to be stable up to $P \approx 180$ in our implementation.

be classified into spatial partitioning, directional partitioning, and hierarchical partitioning. In spatial partitioning, the tree is partitioned between the processors so that each box is assigned to a single processor. This approach works well for non-oscillatory kernels where the expansion order remain constant throughout the tree, for instance, the Laplacian kernel and the Helmholtz kernel in the quasi-static regime. However, if the domain becomes electrically large where wave physics dominates, the expansion order is approximately proportional to the box width. For surface scatterers, this usually results in a computational load that is uniform for all levels of the tree. Therefore, the load becomes unevenly distributed at the top levels of the tree. Improved load balancing can be achieved by using spatial partitioning at the bottom levels of the tree and switch to directional partitioning at the higher levels [VC05, VCS03]. Directional partitioning duplicates all boxes across all processors and the expansions themselves are partitioned instead. While this approach has been successfully deployed to solve large-scale problems [VCS03], it ultimately leads to load imbalance for large numbers of processors. In order to sustain the load balance at all levels hierarchical partitioning must be used, where both spatial and directional partitioning are applied simultaneously for the intermediate levels of the tree in a hierarchical configuration [EG09, EG11, FO08b].

1.3 Outline of Thesis

This thesis is organized as follows.

In Chapter 1, we introduced the Barnes-Hut algorithm and the Fast Multipole Method. A survey of previous work related to their use in computational electromagnetics was presented.

In Chapter 2, we discuss capacitance extraction and its importance in today's electronic design automation industry. An overview of popular numerical techniques is presented and related to our contributions.

In Chapter 3, we extend the free-space center-of-charge approximation to

multi-layered media and present detailed derivations and error analysis. We show that the center-of-charge approximations can be hierarchically clustered and applied to the Barnes-Hut algorithm efficiently. Finally, the method is demonstrated for fast capacitance extraction in practical interconnects.

In Chapter 4, we transition from electrostatics to full-wave modeling. We introduce EFIE and provide a formulation that can be accelerated with tree-based algorithms.

In Chapter 5, we generalize the Barnes-Hut algorithm for rapid evaluation of time-harmonic fields and show that it can be a simple alternative to the LF-FMM.

In Chapter 6, we transition from full-wave modeling in the low frequency regime to all frequencies and discuss challenges that arise in broad-band modeling and their remedies. MFIE and CFIE are also introduced in this chapter.

In Chapter 7, we introduce a novel modification of the LF-FMM based on partial wave expansions. We show that the proposed extension is highly efficient for evaluating the vectorial fields that are arise in the solution of EFIE, MFIE, and CFIE.

In Chapter 8, we conclude this thesis and provide suggestions for future work.

Chapter 2

Capacitance Extraction

In this chapter, we introduce capacitance extraction and its importance to the analysis and manufacturing of integrated circuit's in today's electronics industry. We also present a survey of common numerical techniques for capacitance extraction and how they relate to our contributions in Chapter 3.

Since the first integrated circuits (IC) were invented there has been a need to predict parasitic effects between metal wires that connect electronic devices. The parasitic parameters are used to convert a physical design to an electric network that consists of resistors, capacitors and inductors. Voltages and currents are applied to the resulting networks to model and predict characteristics such as signal delay, signal noise, voltage drop, and other reliability and performance metrics. Signal and Power Integrity Engineers use these characteristics to simulate, validate, and optimize designs of the interconnects before they are manufactured. The semiconductor technology has evolved rapidly over the past decades and today's ICs have up to a seven billion devices manufactured and interconnected on a single semiconductor substrate or wafer [NVI13]. The high density of wires and devices as well as the nanometer scale lead to extremely complicated wiring arrangements and electromagnetic interactions. The circuits are typically embedded in layered dielectric media which increase the complexity of the electromagnetic interactions. Therefore,

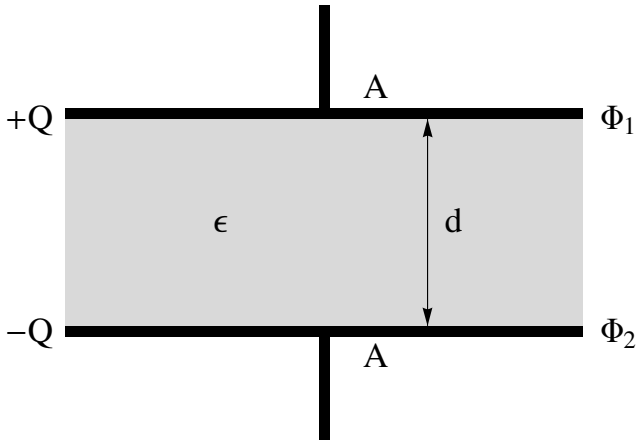

Figure 2.1: Parallel plate capacitor.

accurate estimates of parasitic parameters are paramount in order to design high-density and high performing integrated circuits. In addition, inaccurate simulations may cause severe side-effects to the signal integrity such as, ringing, high reflection loss, and excessive cross-talk.

The simplest model of a capacitor is the parallel-plate model which consists of two parallel conductive plates that are separated by a dielectric slab with permittivity ϵ and thickness d. The plates extend uniformly over an area A and have potentials Φ_1 and Φ_2. A charge of $Q_1 = +Q$ and $Q_2 = -Q$ is distributed on the plates as shown in Figure 2.1. The capacitance can then be obtained from

$$C = \frac{Q}{\Phi_1 - \Phi_2} = \epsilon \frac{A}{d} \tag{2.1}$$

This result show that the capacitance depend on the area of the conductive surface as well as the distance between the conductors and the dielectric properties of the material that separates them. In practice, the geometry of the interconnects is very complicated and capacitance between multiple conductors must be taken into account. In a network of N conductors, a capacitance matrix $\mathbf{C}$ is defined as the relationship

$$\mathbf{Q} = \mathbf{C}\mathbf{\Phi} \tag{2.2}$$

where $\mathbf{Q}$ and $\mathbf{\Phi}$ describe the charges and potentials at the conductors, respectively. The expanded form of 2.2 can be written as

$$\begin{pmatrix} Q_1 \\ Q_2 \\ \vdots \\ Q_N \end{pmatrix} = \begin{pmatrix} C_{11} & C_{12} & \dots & C_{1N} \\ C_{21} & C_{22} & \dots & C_{2N} \\ \vdots & \vdots & \ddots & \vdots \\ C_{N1} & C_{N2} & \dots & C_{NN} \end{pmatrix} \begin{pmatrix} \Phi_1 \\ \Phi_2 \\ \vdots \\ \Phi_N \end{pmatrix} \tag{2.3}$$

where the diagonal coefficients C_{ii} represents the self-capacitance of conductor i and the off diagonal coefficients C_{ij} represents the mutual capacitance between conductors i and j.

To fully characterize the conductive paths in a network, we need matrices of mutual resistances $\mathbf{R}$, inductances $\mathbf{L}$, and conductances $\mathbf{G}$, in addition to the capacitance matrix $\mathbf{C}$. An equivalent circuit model of the entire region of interest can be obtained by cascading the corresponding $\mathbf{R}$, $\mathbf{L}$, $\mathbf{C}$, and $\mathbf{G}$ matrices. In this thesis, we discuss efficient methodology for extracting the capacitance matrix, $\mathbf{C}$, in interconnects via tree based algorithms. Finally, we note that numerical techniques for capacitance extraction can in general be modified to be applicable to extraction of parasitic resistance and inductance due to duality of capacitive and inductive interactions in the quasi-static regime.

2.1 Numerical Techniques

Perhaps the most widely used capacitance extraction method involves slicing the full 3D geometry into 2D slices and computing the 2D capacitance for each slice from a large database of pre-computed values. The 2D capacitances are then cascaded to obtain the capacitance matrix for the full 3D structure. This approach is efficient and sufficiently accurate for a large fraction of the interconnects inside integrated circuits. However, the method can be highly inaccurate for interconnects where full 3D effects must be taken into account.

In those cases, 3D electrostatics field solvers are required for accurate description of the capacitive interactions. A general approach for computing the j's column of the capacitance matrix is to set jth conductor to the potential $\Phi_j = 1V$ and ground the remaining conductors,

$$\Phi_i = \begin{cases} 1 & \text{if } i = j; \\ 0 & \text{otherwise} \end{cases} \tag{2.4}$$

By solving for charges Q_i, $i = 1, ..., N$, induced on each conductor we obtain jth column of capacitance matrix, $C_{ij} = Q_i$.

Available electrostatic solver techniques include the finite-difference method [SKS+88], the finite-element method (FEM) [CB85] and integral equation (IE) methods such as the method of moments (MoM) [NW91]. These methods can solve for the electrostatic charge density with high accuracy. Both the FDM and FEM require that the field throughout the entire volume occupied by the geometry is discretized and enclosed in a bounding box, which leads to large but sparse matrix equations. IE methods only require that the surfaces of material interfaces are discretized which result in comparatively smaller matrix equations that are dense. In ICs, this involve discretization of the surfaces of the conductors and the interfaces between dielectric layers. IE methods have many advantages over FDM and FEM, including good conditioning, lower dimensionality and the capability of handling arbitrary geometries efficiently. However, due to the dense nature of the matrix equation, the computational time and memory requirements become prohibitive for large problems. To further reduce the complexity, the matrix equation is normally solved with an acceleration technique that reduce the computational complexity of a matrix-vector product from $O(N^2)$ to orders that are as low as $O(N)$ for an $N \times N$ matrix. The principle behind the acceleration methods is to compute contributions from *nearby* elements accurately and introduce mathematical approximations for contributions from *distant* elements while controlling the approximation errors. Several acceleration matrix vector product algorithms have been developed, most notably are the fast multipole method

(FMM) [NW91], precorrected-FFT [BBJ94, PW97], and matrix compression methods [KL97, GJ04].

Integrated circuits are most commonly implemented as planar 3D metal structures embedded in stratified medium of the silicon substrate. Several attempts have been made to extend the free-space kernel in FMM to incorperate the stratified dielectric media so that only surfaces of conductors are discretized with MoM [JMM95, JMM96, PC04]. By eliminating the boundaries between dielectric layers, a substantial reduction of computational time and memory is realized. However, these methods are difficult to implement due to the complicated mathematical machinery require to factorize the pertinent Green's function.

2.2 Barnes-Hut Accelerated Capacitance Extraction

In the next chapter, we introduce a new capacitance extraction algorithm that is accelerated with the BH algorithm. It provides several desirable properties, including

- Acceleration of the pertinent matrix vector products to $O(NlogN)$ time and memory which matches the fast multipole method.
- Inclusion of the stratified dielectric media effects so that only the surfaces of conductors are discretized.
- Simplicity of implementation compared to the FMM for stratified media.
- Enables the use of the BH algorithm which in itself has desirable properties such as being inherently adaptive and easy to parallelize.

Chapter 3

The Barnes-Hut Hierarchical Center-of-Charge Approximation for Fast Capacitance Extraction in Multilayered Media

The Barnes-Hut algorithm is widely used in astrophysics for solving large gravitational N-body problems using $O(N \log N)$ time and memory. This reduction in computational cost is achieved by a hierarchical application of the classical center-of-mass approximation. As both gravitational and electrostatic potentials are subject to a $1/R$ dependence, the Barnes-Hut algorithm is also a natural choice for rapidly evaluating interactions between charged particles. The contribution of this paper is an extension of the Barnes-Hut hierarchical clustering to the acceleration of charge interactions in stratified media. We derive and validate a closed-form expression for the shift of the center-of-charge location induced by the physical inhomogeneities and show that proper positioning of the center-of-charge ensures $O(1/R^3)$ error decay in the field approximation. Hierarchical applications of the proposed clustering approximation is demonstrated for the construction of $O(N \log N)$ Method-of-Moment based capacitance extractors.

3.1 Introduction

When designing interconnect layouts at the chip, package and board integration levels, microwave engineers continue to adopt an approach where parasitic RLCG parameters of the nets are evaluated using quasi-static extractors. These parameters are then used to create SPICE-compatible circuit models which account for the distributed electromagnetic coupling mechanisms between the nets of the layout. Combined with non-linear device models, the circuit models of the distributed passive structures can be used to accurately predict crosstalk, ringing, ground bounce, time of flight and various other parameters critical for the electronic design of high-speed propagation channels.

In method-of-moments [1] based extractors the number of unknowns N in-

troduced by discretization of the interconnect geometry leads to $O(N^2)$ computational complexity. The direct $O(N^2)$ solution makes numerical extraction of RLCG parameters practically impossible for complicated designs involving a large number of nets. Under these circumstances, the computational complexity of method-of-moments can be reduced to $O(N \log N)$ with the aid of hierarchical tree-based fast algorithms.

Fast algorithms of this nature also play an important role in astrophysics, fluid dynamics, and various other areas of computational physics where the demand for fast solutions to large problems has produced several tree-based hierarchical acceleration schemes [2]. These methods include Appel's algorithm [3], the Barnes-Hut algorithm [4], and the fast multipole method [5, 6]; all of which reduce the associated computational complexity of the N-body problem from $O(N^2)$ to $O(N \log N)$. The fast multipole method is perhaps the most popular of these acceleration schemes as it is capable of achieving full machine precision, a feature that neither Appel's algorithm nor the Barnes-Hut algorithm can boast. In comparison, the low-order nature of the Barnes-Hut algorithm may allow for a faster and more memory efficient solution than the fast multipole method. As a result the Barnes-Hut algorithm may be the method of choice when only two digits of accuracy are desired [7]. This level of accuracy is often sufficient in low order method-of-moments [1] discretizations of the electrostatic integral equation that arise in RLCG parameter extraction. This makes the Barnes-Hut algorithm an attractive acceleration scheme for large interconnect networks [7, 8, 9, 10, 11, 12, 13, 14, 15].

The presence of multilayered media makes it difficult to apply fast algorithms to the capacitance extraction problem. Complications arise due to the way fast algorithms mathematically represent the pertinent Green's function. The lowest degree of complication is incurred by random-walk based algorithms [16]; algorithms based on QR-compression of rank-deficient matrices [17, 18]; hierarchical algorithms proposed in [19, 20]; and direct hierarchical solvers [21, 22, 23]. FFT-based acceleration schemes such as the pre-corrected

FFT algorithm [24, 25] (also known as the adaptive integral method [26, 27]) and the conjugate gradient FFT algorithm [28] may have more serious problems in the presence of stratified media as they are known to partially lose their efficiency for such inhomogeneities [29]. Finally, the extension of tree-based hierarchical methods such as the fast multipole method, Appel's algorithm, or the Barnes-Hut algorithm to general layered media is significantly more complicated than any of the algorithms previously mentioned. Hierarchical methods generally rely on an analytic factorization of the pertinent Green's function, and while several modifications of the fast multipole method algorithm for solving Poisson's equation in multilayered media have been proposed in the past [12, 13, 14, 15], such modifications for the Barnes-Hut algorithm have not yet been developed.

Assuming that the layered media Green's function is known, any direct $O(N^2)$ solution to the N-body problem is kernel independent. In our previous publications [30, 31, 32] we have presented a point-based capacitance extractor. This extractor was deemed to be kernel-independent since the Barnes-Hut algorithm was applied using a free-space center-of-charge approximation. When working in a multilayered medium, the free-space center-of-charge approximation entails notably higher error than an equivalent multilayer center-of-charge approximation that accounts for the subtrate inhomogeneities. In [33] it was shown that for a group of charged particles located within a domain crossing a single dielectric interface the center-of-charge shifts with respect to its location in homogeneous media by a distance proportional to the difference in relative permittivities of the media above and below the interface. In this paper we provide a complete extension to [33] by proposing a systematic methodology for determining the center-of-charge location for an arbitrary distribution of charged sources embedded in a general multilayered media.

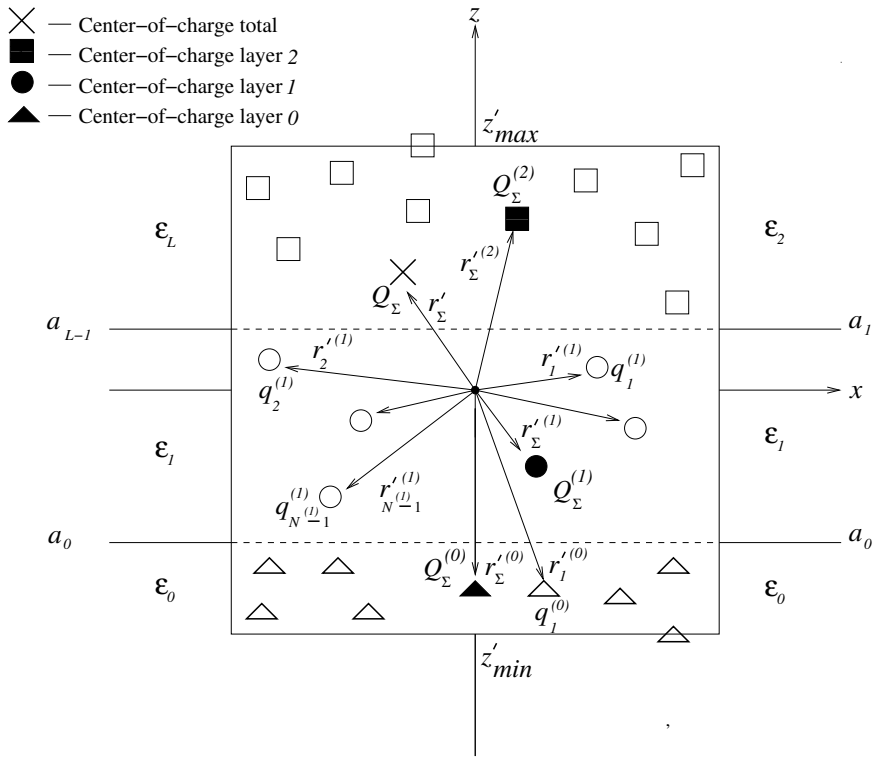

Figure 3.1: Group of arbitrary charged sources situated in general multilayered media. Different markers depict groups of charges confined within distinct layers. Solid black markers denote partial centers-of-charge for distinct layers.

3.2 Derivation of the Center-of-Charge in Layered Media

3.2.1 The Spatial Center-of-Charge Approximation

Consider a stratified media consisting of L layers sequentially indexed $l = 0, 1, \ldots, L-1$ in the direction of increasing coordinate z transverse to the layer interfaces. Let the lth layer contain N^l point charges q_0^l through $q_{N^l-1}^l$ situated at the coordinates $\boldsymbol{r}_0'^l$ through $\boldsymbol{r}_{N^l-1}'^l$ as shown in Fig. 3.1. The point source elevations are assumed to be confined to the interval $z' \in [z'_{min}, z'_{max}]$.

The electrostatic potential $G_m^l(\boldsymbol{r}, \boldsymbol{r}')$ observed at a point $\boldsymbol{r}$ in layer m due to a point charge of one Coulomb situated at $\boldsymbol{r}'$ in layer l satisfies Poisson's equation [34]

$$\begin{aligned} \nabla^2 G_m^l(\boldsymbol{r}, \boldsymbol{r}') &= -\frac{1}{\varepsilon_0 \epsilon_m} \delta(\boldsymbol{r} - \boldsymbol{r}'), \\ a_{m-1} \leq z \leq a_m, &\quad a_{l-1} \leq z' \leq a_l, \end{aligned} \tag{3.1}$$

where $0 \leq l \leq L-1$, a_m is the z coordinate of the mth dielectric interface, ε_0 is the free-space permittivity and where ϵ_m is the relative permittivity in layer m (Fig.3.1). The potential $G_m^l(\boldsymbol{r}, \boldsymbol{r}')$ must be continuous and satisfy continuity of the normal component of the electric displacement $\boldsymbol{D} = -\varepsilon_0 \epsilon_r \nabla \Phi$ across the dielectric interfaces located at $z = a_m$, *i.e.,*

$$G_{m+1}^l = G_m^l, \quad \epsilon_{m+1} \partial_z G_{m+1}^l = \epsilon_m \partial_z G_m^l, \tag{3.2}$$

where $m = 0, \ldots, L-2$ and the operator ∂_x above and throughout the paper denotes differentiation with respect to a variable x.

As each layer l contains N^l point charges, the total field observed at $\boldsymbol{r}$ in layer m can be written as a superposition of individual charge contributions

$$\Phi_m(\boldsymbol{r}) = \sum_{l=0}^{L-1} \sum_{n=0}^{N^l-1} q_n^l G_m^l(\boldsymbol{r}, \boldsymbol{r}_n'^l). \tag{3.3}$$

To accelerate the N-body problem via the Barnes-Hut algorithm, we must approximate the electrostatic potential $\Phi_m(\boldsymbol{r})$ produced by N point sources with the electrostatic potential $\Psi_m^\ell(\boldsymbol{r})$ of a single point charge Q_Σ placed at $\boldsymbol{r}'_\Sigma = x'_\Sigma \hat{x} + y'_\Sigma \hat{y} + z'_\Sigma \hat{z}$ in some layer ℓ,

$$\Psi_m^\ell(\boldsymbol{r}, \boldsymbol{r}'_\Sigma) = Q_\Sigma G_m^\ell(\boldsymbol{r}, \boldsymbol{r}'_\Sigma). \tag{3.4}$$

In the classical free-space problem, the center-of-charge value Q_Σ^{fs} and location $\boldsymbol{r}_\Sigma'^{fs}$ are computed as the net charge and weighted average position respectively

$$Q_\Sigma^{fs} = \sum_{l=0}^{L-1} \sum_{n=0}^{N^l-1} q_n^l, \quad \boldsymbol{r}_\Sigma'^{fs} = \frac{1}{Q_\Sigma} \sum_{l=0}^{L-1} \sum_{n=0}^{N^l-1} q_n^l \boldsymbol{r}_n'^l. \tag{3.5}$$

This paper is devoted to determining the value Q_Σ and the location $\boldsymbol{r}'_\Sigma$ of the center-of-charge approximation in layered media such that the approximate potential is $O(1/R^3)$ accurate, *i.e.*,

$$\Phi_m(\boldsymbol{r}) = \Psi_m^\ell(\boldsymbol{r}, \boldsymbol{r}'_\Sigma) + O(1/R^3), \tag{3.6}$$

where $R = |\boldsymbol{r} - \boldsymbol{r}'|$ and $\boldsymbol{r}'_\Sigma$ is located in layer ℓ.

For clarity we outline the procedure used to determine the center-of-charge approximation in layered media:

- We show that if a box contains charged sources that spans multiple z-directed dielectric layers, the location of the center-of-charge along the x and y coordinates is the same as if the sources were located in a homogeneous space. This is achieved by:
  - Converting the layered media Green's function to its spectral representation over the x and y coordinates. This representation becomes Ewald's identity [35] in the absence of inhomogeneities over the z coordinate.
  - Expanding the Green's function spectrum into a Taylor series representation at the stationary phase point [34, 35].
  - Determining the net charge Q_Σ and lateral coordinates $\boldsymbol{\rho}'_\Sigma$ of the center-of-charge by matching its monopole and dipole moments (zero-th and first Taylor series terms) to those of the true field.
- The center-of-charge location z'_Σ is obtained by matching dipole moments of the true and center-of-charge fields over the z coordinate as follows:
  - The solution of the ordinary differential equation in each layer satisfied by the spectral Green's function is written for the true and approximating field spectra as a sum of common and forced solutions.

– Equating the monopole and dipole moments of the solutions to the differential equation in each layer for the true and approximating fields yields the sought location of the center-of-charge elevation z'_Σ.

3.2.2 The Spectral Center-of-Charge Approximation

In order to satisfy the spatial center-of-charge approximation (3.6) we will match the spectrum of the center-of-charge approximation to the spectrum of the charge distribution near the stationary phase point [34, 35]. Therefore we write the solution of (3.1) as a Fourier transform

$$G_m^l(\boldsymbol{r},\boldsymbol{r'}) = \frac{1}{4\pi^2}\int_{\alpha=0}^{2\pi}\int_{\lambda=0}^{\infty} d\alpha d\lambda\lambda \tilde{g}_m^l(\lambda,z,z')e^{-i\boldsymbol{\lambda}\cdot(\boldsymbol{\rho}-\boldsymbol{\rho'})}, \tag{3.7}$$

where $\boldsymbol{\rho} = x\hat{\boldsymbol{x}} + y\hat{\boldsymbol{y}}$, $\boldsymbol{\rho'} = x'\hat{\boldsymbol{x}} + y'\hat{\boldsymbol{y}}$ are the respective locations of the observation and source points in the XY-plane and where $\boldsymbol{\lambda} = k_x\hat{\boldsymbol{k}}_{\boldsymbol{x}} + k_y\hat{\boldsymbol{k}}_{\boldsymbol{y}}$ is the position vector of a point in the spectral domain (commonly referred to as k-space) with $k_x = \lambda\cos\alpha$ and $k_y = \lambda\sin\alpha$ [34]. In (3.7), $\tilde{g}_m^l(\lambda,z,z') = g_m^l(\lambda,z,z')e^{-i\boldsymbol{\lambda}\cdot\boldsymbol{\rho'}}$, where $g_m^l(\lambda,z,z')$ is the true 2D spectrum of $G_m^l(\boldsymbol{r},\boldsymbol{r'})$. From (3.3) and (3.7) the net potential resulting from all point charges in the system can be written as

$$\begin{aligned}\Phi_m(\boldsymbol{r}) = \frac{1}{4\pi^2}\int_0^{2\pi}\int_0^{\infty} d\alpha d\lambda\lambda \\ \sum_{l=0}^{L-1}\sum_{n=0}^{N^l-1} q_n^l\tilde{g}_m^l(\lambda,z,z_n'^l)e^{-i\boldsymbol{\lambda}\cdot(\boldsymbol{\rho}-\boldsymbol{\rho}_n'^l)}.\end{aligned} \tag{3.8}$$

Using the method of stationary phase [35] it is possible to show that in (3.8) the stationary phase point $\lambda = 0$ of the Green's function provides a dominant contribution to the field $\Phi_m(\boldsymbol{r})$ at distant observation locations $|\boldsymbol{r}| \gg 1$ [35]. Following [35], we factor the integrand in (3.8) into a slowly varying part

$$\phi_m(\lambda,\alpha) = \sum_{l=0}^{L-1}\sum_{n=0}^{N^l-1} q_n^l\lambda\tilde{g}_m^l(\lambda,z,z_n'^l)e^{i\boldsymbol{\lambda}\cdot\boldsymbol{\rho}_n'^l}, \tag{3.9}$$

and a rapidly oscillating part $e^{-i\boldsymbol{\lambda}\cdot\boldsymbol{\rho}}$. Thus (3.8) becomes

$$\Phi_m(\boldsymbol{r}) = \frac{1}{4\pi^2}\int_0^{2\pi}\int_0^{\infty} d\alpha d\lambda \phi_m(\lambda,\alpha) e^{-i\boldsymbol{\lambda}\cdot\boldsymbol{\rho}}. \tag{3.10}$$

Similarly, the approximate potential (3.4) can be expanded as

$$\begin{aligned}\Psi_m^{\ell}(\boldsymbol{r},\boldsymbol{r}'_{\Sigma}) = Q_{\Sigma} G_m^{\ell}(\boldsymbol{r},\boldsymbol{r}'_{\Sigma}) = \\ \frac{1}{4\pi^2}\int_0^{2\pi}\int_0^{\infty} d\alpha d\lambda \psi_m^{\ell}(\lambda,\alpha) e^{-i\boldsymbol{\lambda}\cdot\boldsymbol{\rho}},\end{aligned} \tag{3.11}$$

where $\psi_m^{\ell}(\lambda)$ is the slowly varying part in the approximating field spectrum

$$\psi_m^{\ell}(\lambda,\alpha) = Q_{\Sigma}\lambda \tilde{g}_m^{\ell}(\lambda, z, z'_{\Sigma}) e^{i\boldsymbol{\lambda}\cdot\boldsymbol{\rho}'_{\Sigma}}. \tag{3.12}$$

In order to achieve $O(1/R^3)$ error in (3.6) it is sufficient to match the slowly varying spectra in (3.9) and (3.12) to first order in the vicinity of the stationary phase point $\lambda = 0$. Detailed error analysis supporting this claim is provided in the Appendix. Expanding each spectrum into Taylor's series about $\lambda = 0$ and equating up to the first order terms we wish to enforce

$$\phi_m(0,\alpha) + \lambda\partial_\lambda\phi_m(0,\alpha) = \psi_m^{\ell}(0,\alpha) + \lambda\partial_\lambda\psi_m^{\ell}(0,\alpha) \tag{3.13}$$

Satisfying (3.13) in the vicinity of the stationary phase point implies satisfying (3.6) as shown in the Appendix. The location $\boldsymbol{r}'_{\Sigma}$ and value Q_{Σ} of the approximating point charge provide four degrees of freedom and we can select their values such that the truncated true field expansion on the left hand side of (3.13) matches the truncated approximating field expansion on the right side of (3.13). This matching procedure is described next.

3.2.3 Equations for the Center-of-Charge in Layered Media

In order to enforce (3.13) from (3.9) and (3.12) we note that the first order expansion of the product of two functions is equal to the product of the first order

expansions of the same functions (where second order terms are neglected), and re-write the first-order equivalence (3.13) as follows

$$\begin{aligned} &Q_\Sigma \left[\hat{g}_m^\ell(0,z,z'_\Sigma) + \lambda\partial_\lambda \hat{g}_m^\ell(0,z,z'_\Sigma)\right][1+\boldsymbol{\lambda}\cdot\boldsymbol{\rho}'_\Sigma] = \\ &\sum_{l=0}^{L-1}\sum_{n=0}^{N^l-1}\left[q_n^l \hat{g}_m^l(0,z,z'^l_n) + \lambda\partial_\lambda \hat{g}_m^l(0,z,z'^l_n)\right][1+\boldsymbol{\lambda}\cdot\boldsymbol{\rho}'^l_n], \end{aligned} \tag{3.14}$$

In (3.14) $\hat{g}_m^\ell$ and $\hat{g}_m^l$ are used to denote the respective products $\lambda\tilde{g}_m^\ell$ and $\lambda\tilde{g}_m^l$. Retaining only the zeroth and first order λ terms we obtain the following relationships

$$Q_\Sigma \hat{g}_m^\ell(0,z,z'_\Sigma) = \sum_{l=0}^{L-1}\sum_{n=0}^{N^l-1} q_n^l \hat{g}_m^l(0,z,z'^l_n), \tag{3.15}$$

$$Q_\Sigma \hat{g}_m^\ell(0,z,z'_\Sigma)\boldsymbol{\rho}'_\Sigma = \sum_{l=0}^{L-1}\sum_{n=0}^{N^l-1} q_n^l \hat{g}_m^l(0,z,z'^l_n)\boldsymbol{\rho}'^l_n, \tag{3.16}$$

$$Q_\Sigma \partial_z \hat{g}_m^\ell(0,z,z'_\Sigma) = \sum_{l=0}^{L-1}\sum_{n=0}^{N^l-1} q_n^l \partial_z \hat{g}_m^l(0,z,z'^l_n). \tag{3.17}$$

The above four equations (vector equation (3.16) constitutes two equations) can be satisfied through the appropriate choice of the four parameters Q_Σ, x'_Σ, y'_Σ, and z'_Σ characterizing the center-of-charge value and its location.

3.2.4 Determining Q_Σ and $\boldsymbol{\rho}'_\Sigma$

Satisfying relationships (3.15)-(3.17) begins by observing that for any of the observation layers $m = 0, \ldots, L-1$ the Green's function spectrum $\hat{g}_m^\ell(0,z,z')$ at $\lambda = 0$ remains constant for any source point location z' and source layer index ℓ. By virtue of this property equations (3.15) and (3.16) are trivially satisfied when the approximating charge Q_Σ and its transverse coordinates $\boldsymbol{\rho}'_\Sigma = (x'_\Sigma, y'_\Sigma)$ are chosen as

$$Q_\Sigma = \sum_{l=0}^{L-1}\sum_{n=0}^{N^l-1} q_n^l, \quad \boldsymbol{\rho}'_\Sigma = \frac{1}{Q_\Sigma}\sum_{l=0}^{L-1}\sum_{n=0}^{N^l-1} q_n^l \boldsymbol{\rho}'^l_n. \tag{3.18}$$

It is apparent from (3.5) that the system (3.18) represents the classical formulas for the center-of-charge in homogenous 2D space. This will confirm an intuitive physical result: the z dependent inhomogeneity of the layered media should not affect the value Q_Σ or coordinate $\boldsymbol{\rho}'_\Sigma$ of the center-of-charge transverse to the inhomogeneity. In what follows we will show that a solution to (3.17) provides a value of Q_Σ that is consistent with (3.18).

3.2.5 Determining z'_Σ

While equations (3.15) and (3.16) were satisfied by choosing the net charge Q_Σ and its lateral coordinates x'_Σ, y'_Σ as if the sources were situated in a homogeneous medium, determining the center-of-charge location z'_Σ by satisfying (3.17) entails a notably more complicated procedure which is described below.

The differential equation for $\tilde{g}^l_m(\lambda, z, z')$

Without loss of generality, we assume that all source points have zero transverse coordinate, *i.e.*, $\boldsymbol{\rho}'^l_n = 0$, $\boldsymbol{\rho}'_\Sigma = 0$. In order to distinguish between the spectrum of this special case and the spectrum when non-zero transverse coordinates are present we introduce the spectral functions

$$\dot{\phi}_m(\lambda) = \sum_{l=0}^{L-1} \sum_{n=0}^{N^l-1} q^l_n \hat{g}^l_m(\lambda, z, z'^l_n), \tag{3.19}$$

$$\dot{\psi}^\ell_m(\lambda) = Q_\Sigma \hat{g}^\ell_m(\lambda, z, z'_\Sigma), \tag{3.20}$$

for the true, and approximating field spectra, respectively.

By substituting the spectrum (3.7) into Poisson's equation (3.1) it is easy to show that the point spectrum $\tilde{g}^l_m(\lambda, z, z') = \hat{g}^l_m(\lambda, z, z')/\lambda$ satisfies the following ordinary differential equation

$$\begin{gathered} \frac{d^2 \tilde{g}^l_m(\lambda, z, z')}{dz^2} - \lambda^2 \tilde{g}^l_m(\lambda, z, z') = -\frac{1}{\varepsilon_0 \epsilon_m} \delta(z - z'), \\ a_{m-1} \le z \le a_m, \quad a_{l-1} \le z' \le a_l, \end{gathered} \tag{3.21}$$

and the spectral domain analog of boundary conditions (3.2)

$$\begin{aligned}\tilde{g}^l_{m+1}(\lambda, a_m, z') &= \tilde{g}^l_m(\lambda, a_m, z'),\\ \epsilon_{m+1}\partial_z\tilde{g}^l_{m+1}(\lambda, a_m, z') &= \epsilon_m\partial_z\tilde{g}^l_m(\lambda, a_m, z'),\end{aligned} \tag{3.22}$$

where $m, l = 0, \ldots, L-2$.

The solution of this system can be written in its most general form as a sum of the common and particular solutions to the ordinary differential equation for both the true and approximating fields in layer m as

$$\begin{aligned}\dot{\phi}_m(\lambda) = &\frac{C^-_m(\lambda)e^{-\lambda(z-a_{m-1})}}{2\varepsilon_0\epsilon_m} + \frac{C^+_m(\lambda)e^{-\lambda(a_m-z)}}{2\varepsilon_0\epsilon_m}\\ &+ \sum_{n=0}^{N^m-1}\frac{q^{(m)}_n e^{-\lambda|z-z'^{(m)}_n|}}{2\varepsilon_0\epsilon_m},\end{aligned} \tag{3.23}$$

$$\begin{aligned}\dot{\psi}^\ell_m(\lambda) = &\frac{D^{-,\ell}_m(\lambda)e^{-\lambda(z-a_{m-1})}}{2\varepsilon_0\epsilon_m} + \frac{D^{+,\ell}_m(\lambda)e^{-\lambda(a_m-z)}}{2\varepsilon_0\epsilon_m}\\ &+ \frac{\delta_{m\ell}Q_\Sigma e^{-\lambda|z-z'_\Sigma|}}{2\varepsilon_0\epsilon_m},\end{aligned} \tag{3.24}$$

where $\delta_{\ell'\ell}$ is the Kronecker's delta, $a_{m-1} \le z \le a_m$ and where the superscript notation (m) is used to indicate that charge values and positions are located in layer m. Here we extend our definition of the geometry such that $a_{-1} = -\infty$ and $a_{L-1} = \infty$. The choice of index value $\ell = 0, 1, \ldots, L-1$ places the center-of-charge in any one of the layers. Additionally, as the electrostatic potential must vanish at $\pm\infty$ we note that C^+_{L-1}, $D^{+,\ell}_{L-1}$, C^-_0 and $D^{-,\ell}_0$ must all be identically zero.

Having explicitly written equations for the spectra (3.23) and (3.24) we may draft a plan for enforcing their first order equality as follows: First we will determine explicit forms for first-order approximations of (3.23) and (3.24) in terms of the unknown coefficients $C^{+/-}_m$ and $D^{+/-,\ell}_m$. Next we will use the boundary conditions (3.22) to solve for the coefficients $C^{+/-}_m$ and $D^{+/-,\ell}_m$ which will allow us to equate the first-order expansions of (3.23) and (3.24) and solve for z'_Σ.

First Order Expansions for $\dot{\boldsymbol{\phi}}$ and $\dot{\boldsymbol{\psi}}$

For clarity we consider the specific case of a three-layered medium. Our motivation is two-fold: First, there is no loss of generality as the steps taken hold for the general L layer case, and second, explicitly solving the three-layer case provides significant insight into the solution of the problem. For the purpose of compact notation we have found it beneficial to cast (3.23) and (3.24) into matrix form

$$\dot{\boldsymbol{\phi}}(\lambda) = \mathbf{E}(\lambda) \cdot \mathbf{C}(\lambda) + \mathbf{Q}(\lambda), \tag{3.25}$$

$$\dot{\boldsymbol{\psi}}(\lambda) = \mathbf{E}(\lambda) \cdot \mathbf{D}^{\ell}(\lambda) + Q_{\Sigma} e^{-\lambda |z - z'_{\Sigma}|} \mathbf{d}^{\ell}. \tag{3.26}$$

where the arrays $\dot{\boldsymbol{\phi}}$ and $\dot{\boldsymbol{\psi}}$ are given by

$$\begin{aligned} \dot{\boldsymbol{\phi}}(\lambda) &= \left[\begin{array}{ccc} \dot{\phi}_2(\lambda) & \dot{\phi}_1(\lambda) & \dot{\phi}_0(\lambda) \end{array} \right]^t, \\ \dot{\boldsymbol{\psi}}(\lambda) &= \left[\begin{array}{ccc} \dot{\psi}_2(\lambda) & \dot{\psi}_1(\lambda) & \dot{\psi}_0(\lambda) \end{array} \right]^t \end{aligned} \tag{3.27}$$

while the coefficient arrays $\mathbf{C}$ and $\mathbf{D}^{\ell}$ are given by

$$\mathbf{C}(\lambda) = \left[\begin{array}{cccc} C_2^-(\lambda) & C_1^+(\lambda) & C_1^-(\lambda) & C_0^+(\lambda) \end{array} \right]^t, \tag{3.28}$$

$$\mathbf{D}^{\ell}(\lambda) = \left[\begin{array}{cccc} D_2^{-,\ell}(\lambda) & D_1^{+,\ell}(\lambda) & D_1^{-,\ell}(\lambda) & D_0^{+,\ell}(\lambda) \end{array} \right]^t, \tag{3.29}$$

where t denotes matrix transposition. In (3.25) and (3.26), the $L \times (2L-2)$ matrix $\mathbf{E}$ provides weights for the $2L-2$ unknown coefficients in $\mathbf{C}$ and $\mathbf{D}^{\ell}$ in each of the L layers (the coefficients C_{L-1}^+, $D_{L-1}^{+,\ell}$, C_0^- and $D_0^{-,\ell}$ are ommited as they are identically zero). We also note that our convention is such that the equation for layer $L-1$ corresponds to row 0 of the matrix. For the three layer case the matrix $\mathbf{E}$ is simply

$$\mathbf{E}(\lambda) = \left[\begin{array}{cccc} \frac{e^{-\lambda(z-a_1)}}{2\varepsilon_0 \epsilon_2} & 0 & 0 & 0 \\ 0 & \frac{e^{-\lambda(a_1-z)}}{2\varepsilon_0 \epsilon_1} & \frac{e^{-\lambda(z-a_0)}}{2\varepsilon_0 \epsilon_1} & 0 \\ 0 & 0 & 0 & \frac{e^{-\lambda(a_0-z)}}{2\varepsilon_0 \epsilon_0} \end{array} \right], \tag{3.30}$$

while the vectors $\mathbf{Q}$ and $\mathbf{d}^\ell$ are

$$\mathbf{Q}(\lambda) = \begin{bmatrix} \sum_{n=0}^{N^{(2)}-1} \frac{q_n^{(2)} e^{-\lambda|z-z_n'^{(2)}|}}{2\varepsilon_0\epsilon_2} \\ \sum_{n=0}^{N^{(1)}-1} \frac{q_n^{(1)} e^{-\lambda|z-z_n'^{(1)}|}}{2\varepsilon_0\epsilon_1} \\ \sum_{n=0}^{N^{(0)}-1} \frac{q_n^{(0)} e^{-\lambda|z-z_n'^{(0)}|}}{2\varepsilon_0\epsilon_0} \end{bmatrix}, \mathbf{d}^\ell = \begin{bmatrix} \frac{\delta_{2\ell}}{2\varepsilon_0\epsilon_2} \\ \frac{\delta_{1\ell}}{2\varepsilon_0\epsilon_1} \\ \frac{\delta_{0\ell}}{2\varepsilon_0\epsilon_0} \end{bmatrix}. \tag{3.31}$$

We recall that we are seeking to satisfy (3.17) which was derived as a consequence of first order spectral matching in (3.13). Therefore we require first order expansions of $\dot{\boldsymbol{\phi}}$ and $\dot{\boldsymbol{\psi}}$. These expansions can be written in terms of the first order expansions of each term in (3.25) and (3.26)

$$\dot{\boldsymbol{\phi}}(\lambda) \simeq (\mathbf{E_0} + \lambda\mathbf{E_1}) \cdot (\mathbf{C_0} + \lambda\mathbf{C_1}) + (\mathbf{Q_0} + \lambda\mathbf{Q_1}), \tag{3.32}$$

$$\dot{\boldsymbol{\psi}}(\lambda) \simeq (\mathbf{E_0} + \lambda\mathbf{E_1}) \cdot (\mathbf{D_0^\ell} + \lambda\mathbf{D_1^\ell}) + Q_\Sigma(1 \mp \lambda(z - z'_\Sigma))\mathbf{d}^\ell \tag{3.33}$$

where $\lambda \to 0$. In the above equations, matrix subscripts are used to denote which term in the corresponding expansion each matrix represents; and of course once the equations are expanded, only terms up to first order are retained. Also, in (3.33) the '$-$' or '$+$' sign is chosen when $z > z'_\Sigma$ and $z < z'_\Sigma$ respectively. From (3.30) it follows that for three layers $\mathbf{E_0}$ and $\mathbf{E_1}$ are given by

$$\mathbf{E_0} = \frac{1}{2\varepsilon_0} \begin{bmatrix} \frac{1}{\epsilon_2} & 0 & 0 & 0 \\ 0 & \frac{1}{\epsilon_1} & \frac{1}{\epsilon_1} & 0 \\ 0 & 0 & 0 & \frac{1}{\epsilon_0} \end{bmatrix},$$

$$\begin{aligned} \mathbf{E_1} = z\mathbf{E_1'} + \mathbf{E_1''} = & \frac{z}{2\varepsilon_0} \begin{bmatrix} \frac{-1}{\epsilon_2} & 0 & 0 & 0 \\ 0 & \frac{1}{\epsilon_1} & \frac{-1}{\epsilon_1} & 0 \\ 0 & 0 & 0 & \frac{1}{\epsilon_0} \end{bmatrix} \\ & + \frac{1}{2\varepsilon_0} \begin{bmatrix} \frac{a_1}{\epsilon_2} & 0 & 0 & 0 \\ 0 & \frac{-a_1}{\epsilon_1} & \frac{a_0}{\epsilon_0} & 0 \\ 0 & 0 & 0 & \frac{-a_0}{\epsilon_0} \end{bmatrix}, \end{aligned} \tag{3.34}$$

while from (3.31) $\mathbf{Q_0}$ and $\mathbf{Q_1}$ are

$$\mathbf{Q_0} = \begin{bmatrix} \frac{Q_\Sigma^{(2)}}{2\varepsilon_0\epsilon_2} \\ \frac{Q_\Sigma^{(1)}}{2\varepsilon_0\epsilon_1} \\ \frac{Q_\Sigma^{(0)}}{2\varepsilon_0\epsilon_0} \end{bmatrix},$$

$$\begin{aligned} \mathbf{Q_1} = \mp z\mathbf{Q_1'} \pm \mathbf{Q_1''} &= \mp \frac{z}{2\varepsilon_0} \begin{bmatrix} \frac{Q_\Sigma^{(2)}}{\epsilon_2} \\ \frac{Q_\Sigma^{(1)}}{\epsilon_1} \\ \frac{Q_\Sigma^{(0)}}{\epsilon_0} \end{bmatrix} \pm \frac{1}{2\varepsilon_0} \begin{bmatrix} \frac{Q_\Sigma^{(2)} z_\Sigma'^{(2)}}{\epsilon_2} \\ \frac{Q_\Sigma^{(1)} z_\Sigma'^{(1)}}{\epsilon_1} \\ \frac{Q_\Sigma^{(0)} z_\Sigma'^{(0)}}{\epsilon_0} \end{bmatrix} \\ &= \mp z\mathbf{Q_0} \pm \mathbf{Q_1''} \end{aligned} \tag{3.35}$$

In (3.35), the values Q_Σ^l and $z_\Sigma'^l$ denote the net charges and corresponding centers of charge for the sources contained in each layer l

$$Q_\Sigma^l = \sum_{n=0}^{N^l-1} q_n^l, \quad z_\Sigma'^l = \frac{1}{Q_\Sigma^l} \sum_{n=0}^{N^l-1} q_n^l z_n'^l, \quad l = 0, \ldots, L-1. \tag{3.36}$$

Also, in (3.35) the top sign is chosen when $z > z'_{max}$ and the bottom sign is chosen when $z < z'_{min}$ where we recall that globally the point charges are confined to the interval $z'_{min} \leq z_n'^l \leq z'_{max}$ for any n and l. As will be shown in the sequel, this apparently limiting assumption is made so that *the expressions obtained do not depend on the observation location z provided that $z > z'_{max}$ or $z < z'_{min}$*. While the strict validity of the derivations that follow will only hold when $z > z'_{max}$ or $z < z'_{min}$, in the Appendix we show that the derived center-of-charge approximation is still $O(1/R^3) = O(1/\rho^3)$ accurate when $z'_{min} \leq z \leq z'_{max}$. As a result, the values $\mathbf{Q_0}$ and $\mathbf{Q_1}$ can be obtained by considering only the partial per-layer net charges Q_Σ^l positioned at the per-layer centers of charge elevations $z_\Sigma'^l$ given by (3.36). The consequence is that we can always work with a single equivalent point charge Q_Σ^l in each layer l placed at the per-layer center-of-charge $z_\Sigma'^l$.

First Order Expansions for $C_m^{+/-}$ and $D_m^{+/-,\ell}$

In general, the equations (3.25) and (3.26) relate the fields in L layers to $2L-2$ coefficients $\mathbf{C}$ and $\mathbf{D}^\ell$. The $2L-2$ coefficients can be determined by satisfying the continuity of the potential and normal deterivative of the electric flux across each of the $L-1$ interfaces in (3.22).

The special case of a three-layer system corresponding to the matrix (3.30), and the vectors (3.31) produces a 4×4 system of equations for each of the unknown coefficient vectors $\mathbf{C}$ and $\mathbf{D}^\ell$

$$\bar{\mathbf{E}}(\lambda) \cdot \mathbf{C}(\lambda) = \bar{\mathbf{Q}}(\lambda), \tag{3.37}$$

$$\bar{\mathbf{E}}(\lambda) \cdot \mathbf{D}^\ell(\lambda) = Q_\Sigma \bar{\mathbf{d}}^\ell(\lambda). \tag{3.38}$$

where the first $L-1$ rows of the $(2L-2) \times (2L-2)$ matrix $\bar{\mathbf{E}}(\lambda)$ are multiplicative terms for the coefficients $\mathbf{C}(\lambda)$ and $\mathbf{D}^\ell(\lambda)$ when enforcing continuity of the spectral potential at each interface $a_{L-2}, \ldots, a_0$. The following $L-1$ rows arise when enforcing continuity of the normal derivative of the potential spectra. For three layers this matrix can be written as

$$\bar{\mathbf{E}}(\lambda) = \begin{bmatrix} \frac{1}{\epsilon_2} & \frac{-1}{\epsilon_1} & \frac{-e^{-\lambda(a_1-a_0)}}{\epsilon_1} & 0 \\ 0 & \frac{e^{-\lambda(a_1-a_0)}}{\epsilon_1} & \frac{1}{\epsilon_1} & \frac{-1}{\epsilon_0} \\ -1 & -1 & e^{-\lambda(a_1-a_0)} & 0 \\ 0 & e^{-\lambda(a_1-a_0)} & -1 & -1 \end{bmatrix}. \tag{3.39}$$

In a similar fashion, the size $2L-2$ column vectors $\bar{\mathbf{Q}}(\lambda)$ and $\bar{\mathbf{d}}^\ell(\lambda)$ are constructed from the parts of the boundary equations that are independent of $\mathbf{C}(\lambda)$ and $\mathbf{D}^\ell(\lambda)$ respectively. For three layers they may be written as

$$\bar{\mathbf{Q}}(\lambda) = (-1)\times \begin{bmatrix} \sum_{n=0}^{N^{(2)}-1} q_n^{(2)} \frac{e^{-\lambda(z_n'^{(2)}-a_1)}}{\epsilon_2} - \sum_{n=0}^{N^{(1)}-1} q_n^{(1)} \frac{e^{-\lambda(a_1-z_n'^{(1)})}}{\epsilon_1} \\ \sum_{n=0}^{N^{(1)}-1} q_n^{(1)} \frac{e^{-\lambda(z_n'^{(1)}-a_0)}}{\epsilon_1} - \sum_{n=0}^{N^{(0)}-1} q_n^{(0)} \frac{e^{-\lambda(a_0-z_n'^{(0)})}}{\epsilon_0} \\ \sum_{n=0}^{N^{(2)}-1} q_n^{(2)} e^{-\lambda(z_n'^{(2)}-a_1)} + \sum_{n=0}^{N^{(1)}-1} q_n^{(1)} e^{-\lambda(a_1-z_n'^{(1)})} \\ \sum_{n=0}^{N^{(1)}-1} q_n^{(1)} e^{-\lambda(z_n'^{(1)}-a_0)} + \sum_{n=0}^{N^{(0)}-1} q_n^{(0)} e^{-\lambda(a_0-z_n'^{(0)})} \end{bmatrix}, \tag{3.40}$$

$$\bar{\mathbf{d}}^{\ell}(\lambda) = \begin{bmatrix} \frac{-\delta_{2\ell}e^{-\lambda(z'_{\Sigma}-a_1)}}{\epsilon_2} + \frac{\delta_{1\ell}e^{-\lambda(a_1-z'_{\Sigma})}}{\epsilon_1} \\ \frac{-\delta_{1\ell}e^{-\lambda(z'_{\Sigma}-a_0)}}{\epsilon_1} + \frac{\delta_{0\ell}e^{-\lambda(a_0-z'_{\Sigma})}}{\epsilon_0} \\ -\delta_{2\ell}e^{-\lambda(z'_{\Sigma}-a_1)} - \delta_{1\ell}e^{-\lambda(a_1-z'_{\Sigma})} \\ -\delta_{1\ell}e^{-\lambda(z'_{\Sigma}-a_0)} - \delta_{0\ell}e^{-\lambda(a_0-z'_{\Sigma})} \end{bmatrix}. \tag{3.41}$$

Solving for the coefficients C and $\mathbf{D}^{\ell}$

In order to find the first two terms in the Taylor expansion of $\mathbf{C}(\lambda)$ and $\mathbf{D}^{\ell}(\lambda)$ we can approximate the true coefficients as

$$\mathbf{C}(\lambda) = \bar{\mathbf{E}}^{-1}(\lambda) \cdot \bar{\mathbf{Q}}(\lambda) \simeq (\bar{\mathbf{E}}_{\mathbf{0}} + \lambda\bar{\mathbf{E}}_{\mathbf{1}})^{-1} \cdot (\bar{\mathbf{Q}}_{\mathbf{0}} + \lambda\bar{\mathbf{Q}}_{\mathbf{1}}), \tag{3.42}$$

$$\mathbf{D}^{\ell}(\lambda) = \bar{\mathbf{E}}^{-1}(\lambda) \cdot Q_{\Sigma}\bar{\mathbf{d}}^{\ell} \simeq (\bar{\mathbf{E}}_0 + \lambda\bar{\mathbf{E}}_1)^{-1} \cdot (\bar{\mathbf{d}}_0^{\ell} + \lambda\bar{\mathbf{d}}_1^{\ell}), \tag{3.43}$$

where the matrices $\bar{\mathbf{E}}_{\mathbf{0}}$, $\bar{\mathbf{E}}_{\mathbf{1}}$; $\bar{\mathbf{Q}}_{\mathbf{0}}$, $\bar{\mathbf{Q}}_{\mathbf{1}}$; and $\bar{\mathbf{d}}_0^{\ell}$, $\bar{\mathbf{d}}_1^{\ell}$ are the first two coefficients in the Taylor expansion of (3.39), (3.40) and (3.41) respectively

$$\bar{\mathbf{E}}(\lambda) \simeq \bar{\mathbf{E}}_{\mathbf{0}} + \lambda\bar{\mathbf{E}}_{\mathbf{1}} = \begin{bmatrix} \frac{1}{\epsilon_2} & \frac{-1}{\epsilon_1} & \frac{-1}{\epsilon_1} & 0 \\ 0 & \frac{1}{\epsilon_1} & \frac{1}{\epsilon_1} & \frac{-1}{\epsilon_0} \\ -1 & -1 & 1 & 0 \\ 0 & 1 & -1 & -1 \end{bmatrix} + \lambda \begin{bmatrix} 0 & 0 & \frac{a_1-a_0}{\epsilon_1} & 0 \\ 0 & \frac{a_0-a_1}{\epsilon_1} & 0 & 0 \\ 0 & 0 & a_0-a_1 & 0 \\ 0 & a_0-a_1 & 0 & 0 \end{bmatrix}, \tag{3.44}$$

$$\bar{\mathbf{Q}} \simeq \bar{\mathbf{Q}}_{\mathbf{0}} + \lambda\bar{\mathbf{Q}}_{\mathbf{1}} = -\begin{bmatrix} \frac{Q_{\Sigma}^{(2)}}{\epsilon_2} - \frac{Q_{\Sigma}^{(1)}}{\epsilon_1} \\ \frac{Q_{\Sigma}^{(1)}}{\epsilon_1} - \frac{Q_{\Sigma}^{(0)}}{\epsilon_0} \\ Q_{\Sigma}^{(2)} + Q_{\Sigma}^{(1)} \\ Q_{\Sigma}^{(1)} + Q_{\Sigma}^{(0)} \end{bmatrix} + \lambda \begin{bmatrix} Q_{\Sigma}^{(2)}\frac{(z_{\Sigma}^{\prime(2)}-a_1)}{\epsilon_2} - Q_{\Sigma}^{(1)}\frac{(a_1-z_{\Sigma}^{\prime(1)})}{\epsilon_1} \\ Q_{\Sigma}^{(1)}\frac{(z_{\Sigma}^{\prime(1)}-a_0)}{\epsilon_1} - Q_{\Sigma}^{(0)}\frac{(a_0-z_{\Sigma}^{\prime(0)})}{\epsilon_0} \\ Q_{\Sigma}^{(2)}(z_{\Sigma}^{\prime(2)}-a_1) + Q_{\Sigma}^{(1)}(a_1-z_{\Sigma}^{\prime(1)}) \\ Q_{\Sigma}^{(1)}(z_{\Sigma}^{\prime(1)}-a_0) + Q_{\Sigma}^{(0)}(a_0-z_{\Sigma}^{\prime(0)}) \end{bmatrix}, \tag{3.45}$$

$$\bar{\mathbf{d}}^{\ell}(\lambda) \simeq \bar{\mathbf{d}}_0^{\ell} + \lambda z'_{\Sigma}\bar{\mathbf{d}}_1'^{\ell} + \lambda\bar{\mathbf{d}}_1''^{\ell} = \begin{bmatrix} \frac{-\delta_{2\ell}}{\epsilon_2} + \frac{\delta_{1\ell}}{\epsilon_1} \\ \frac{-\delta_{1\ell}}{\epsilon_1} + \frac{\delta_{0\ell}}{\epsilon_0} \\ -\delta_{2\ell} - \delta_{1\ell} \\ -\delta_{1\ell} - \delta_{0\ell} \end{bmatrix} + \lambda z'_{\Sigma} \begin{bmatrix} \frac{\delta_{2\ell}}{\epsilon_2} + \frac{\delta_{1\ell}}{\epsilon_1} \\ \frac{\delta_{1\ell}}{\epsilon_1} + \frac{\delta_{0\ell}}{\epsilon_0} \\ \delta_{2\ell} - \delta_{1\ell} \\ \delta_{1\ell} - \delta_{0\ell} \end{bmatrix} + \lambda \begin{bmatrix} \frac{-\delta_{2\ell}a_1}{\epsilon_2} - \frac{\delta_{1\ell}a_1}{\epsilon_1} \\ \frac{-\delta_{1\ell}a_0}{\epsilon_1} - \frac{\delta_{0\ell}a_0}{\epsilon_0} \\ -\delta_{2\ell}a_1 + \delta_{1\ell}a_1 \\ -\delta_{1\ell}a_0 + \delta_{0\ell}a_0 \end{bmatrix}, \tag{3.46}$$

where $\bar{\mathbf{d}}_1^{\ell} = z'_{\Sigma}\bar{\mathbf{d}}_1'^{\ell} + \bar{\mathbf{d}}_1''^{\ell}$.

From Taylor's expansion we know that

$$(\bar{\mathbf{E}}_{\mathbf{0}} + \lambda\bar{\mathbf{E}}_{\mathbf{1}})^{-1} = \bar{\mathbf{E}}_{\mathbf{0}}^{-1} - \lambda\bar{\mathbf{E}}_{\mathbf{0}}^{-1} \cdot \bar{\mathbf{E}}_{\mathbf{1}} \cdot \bar{\mathbf{E}}_{\mathbf{0}}^{-1} + \cdots, \tag{3.47}$$

and retaining terms up to first order in λ we obtain

$$\begin{aligned} \mathbf{C}(\lambda) \simeq \mathbf{C_0} + \lambda\mathbf{C_1} = \bar{\mathbf{E}}_{\mathbf{0}}^{-1} \cdot \bar{\mathbf{Q}}_{\mathbf{0}} + \\ \lambda(\bar{\mathbf{E}}_{\mathbf{0}}^{-1} \cdot \bar{\mathbf{Q}}_{\mathbf{1}} - \bar{\mathbf{E}}_{\mathbf{0}}^{-1} \cdot \bar{\mathbf{E}}_{\mathbf{1}} \cdot \bar{\mathbf{E}}_{\mathbf{0}}^{-1} \cdot \bar{\mathbf{Q}}_{\mathbf{0}}), \end{aligned} \tag{3.48}$$

$$\begin{aligned} \mathbf{D}^{\ell}(\lambda) \simeq \mathbf{D}_{\mathbf{0}}^{\ell} + \lambda\mathbf{D}_{\mathbf{1}}^{\ell} = Q_{\Sigma}\bar{\mathbf{E}}_{\mathbf{0}}^{-1} \cdot \bar{\mathbf{d}}_0^{\ell} + \lambda Q_{\Sigma} \\ (z'_{\Sigma}\bar{\mathbf{E}}_{\mathbf{0}}^{-1} \cdot \bar{\mathbf{d}}_1'^{\ell} + \bar{\mathbf{E}}_{\mathbf{0}}^{-1} \cdot \bar{\mathbf{d}}_1''^{\ell} - \bar{\mathbf{E}}_{\mathbf{0}}^{-1} \cdot \bar{\mathbf{E}}_{\mathbf{1}} \cdot \bar{\mathbf{E}}_{\mathbf{0}}^{-1} \cdot \bar{\mathbf{d}}_0^{\ell}), \end{aligned} \tag{3.49}$$

which are the desired first-order expansion for the unknown coefficients $\mathbf{C}$ and $\mathbf{D}^{\ell}$.

Equating $\dot{\phi}$ and $\dot{\psi}$ to obtain z'_{Σ}

Substituting the first-order expression for the coefficients $\mathbf{C}$ into (3.32) we obtain the desired first order approximation of the potential spectra in the vicinity of the stationary phase point

$$\begin{aligned} \dot{\boldsymbol{\phi}}(\lambda) \simeq (\mathbf{E_0} \cdot \bar{\mathbf{E}}_{\mathbf{0}}^{-1} \cdot \bar{\mathbf{Q}}_{\mathbf{0}} + \mathbf{Q_0}) + \lambda(\mathbf{E_1} \cdot \bar{\mathbf{E}}_{\mathbf{0}}^{-1} \cdot \bar{\mathbf{Q}}_{\mathbf{0}} + \\ \mathbf{E_0} \cdot \bar{\mathbf{E}}_{\mathbf{0}}^{-1} \cdot \bar{\mathbf{Q}}_{\mathbf{1}} - \mathbf{E_0} \cdot \bar{\mathbf{E}}_{\mathbf{0}}^{-1} \cdot \bar{\mathbf{E}}_{\mathbf{1}} \cdot \bar{\mathbf{E}}_{\mathbf{0}}^{-1} \cdot \bar{\mathbf{Q}}_{\mathbf{0}} + \mathbf{Q_1}), \end{aligned} \tag{3.50}$$

where $\lambda \to 0$.

A similar substitution of the first order representation for $\mathbf{D}^\ell$ into (3.33) provides the approximating center-of-charge potential spectrum in the vicinity of $\lambda = 0$

$$\begin{aligned}\dot{\boldsymbol{\psi}}^\ell(\lambda) \simeq & Q_\Sigma(\mathbf{E_0}\cdot\bar{\mathbf{E}}_\mathbf{0}^{-1}\cdot\bar{\mathbf{d}}_0^\ell + \mathbf{d}^\ell) + \\ & \lambda Q_\Sigma[z'_\Sigma\mathbf{E_0}\cdot\bar{\mathbf{E}}_\mathbf{0}^{-1}\cdot\bar{\mathbf{d}}_1'^\ell + \mathbf{E_0}\cdot\bar{\mathbf{E}}_\mathbf{0}^{-1}\cdot\bar{\mathbf{d}}_1''^\ell \\ & - \mathbf{E_0}\cdot\bar{\mathbf{E}}_\mathbf{0}^{-1}\cdot\bar{\mathbf{E}}_\mathbf{1}\cdot\bar{\mathbf{E}}_\mathbf{0}^{-1}\cdot\bar{\mathbf{d}}_0^\ell \\ & + \mathbf{E_1}\cdot\bar{\mathbf{E}}_\mathbf{0}^{-1}\cdot\bar{\mathbf{d}}_0^\ell \mp (z - z'_\Sigma)\mathbf{d}^\ell],\end{aligned} \tag{3.51}$$

where $\lambda \to 0$. The choice of sign in (3.51) is again taken using '$-$' when $z > z'_\Sigma$ and '$+$' when $z < z'_\Sigma$.

Previously we have shown that the equations for the center-of-charge in layered media (3.15) and (3.16) could be satisfied by selecting Q_Σ and $\boldsymbol{\rho}'_\Sigma$ as in (3.18). We must now verify that this selection of Q_Σ consistently satisfies (3.17). Equating the zeroth order terms of (3.50) and (3.51) gives

$$Q_\Sigma(\mathbf{E_0}\cdot\bar{\mathbf{E}}_\mathbf{0}^{-1}\cdot\bar{\mathbf{d}}_0^\ell + \mathbf{d}^\ell) = (\mathbf{E_0}\cdot\bar{\mathbf{E}}_\mathbf{0}^{-1}\cdot\bar{\mathbf{Q}}_\mathbf{0} + \mathbf{Q_0}). \tag{3.52}$$

An involved analysis of this system of equations shows that each row of the equation is satisfied precisely when the center-of-charge value is selected as sum of net charges in the individual layers

$$Q_\Sigma = Q_\Sigma^{(0)} + Q_\Sigma^{(1)} + Q_\Sigma^{(2)}, \tag{3.53}$$

independent of which layer ℓ contains Q_Σ. This is exactly the value derived in (3.18).

Finally, we can determine the elevation of the center-of-charge z'_Σ by matching the first order coefficients in the Taylor series expansion of the approximating field in (3.51) and the true field (3.50)

$$\begin{aligned}[&\mathbf{E_0}\cdot\bar{\mathbf{E}}_\mathbf{0}^{-1}\cdot(z'_\Sigma\bar{\mathbf{d}}_1'^\ell + \bar{\mathbf{d}}_1''^\ell) - \mathbf{E_0}\cdot\bar{\mathbf{E}}_\mathbf{0}^{-1}\cdot\bar{\mathbf{E}}_\mathbf{1}\cdot\bar{\mathbf{E}}_\mathbf{0}^{-1}\cdot\bar{\mathbf{d}}_0^\ell \\ &\quad + (z\mathbf{E}'_\mathbf{1} + \mathbf{E}''_\mathbf{1})\cdot\bar{\mathbf{E}}_\mathbf{0}^{-1}\cdot\bar{\mathbf{d}}_0^\ell \mp (z - z'_\Sigma)\mathbf{d}^\ell]Q_\Sigma = \\ &[\mathbf{E_0}\cdot\bar{\mathbf{E}}_\mathbf{0}^{-1}\cdot\bar{\mathbf{Q}}_\mathbf{1} - \mathbf{E_0}\cdot\bar{\mathbf{E}}_\mathbf{0}^{-1}\cdot\bar{\mathbf{E}}_\mathbf{1}\cdot\bar{\mathbf{E}}_\mathbf{0}^{-1}\cdot\bar{\mathbf{Q}}_\mathbf{0} \\ &\quad + (z\mathbf{E}'_\mathbf{1} + \mathbf{E}''_\mathbf{1})\cdot\bar{\mathbf{E}}_\mathbf{0}^{-1}\cdot\bar{\mathbf{Q}}_\mathbf{0} \mp (z\mathbf{Q_0} - \mathbf{Q}''_\mathbf{1})].\end{aligned} \tag{3.54}$$

It can be shown that the terms containing the observation point elevation z in the right and left hand sides of the equation (3.54) simplify *i.e.,*

$$z(\mathbf{E}'_{\mathbf{1}} \cdot \bar{\mathbf{E}}_{\mathbf{0}}^{-1} \cdot \bar{\mathbf{d}}_0^{\ell} \mp \mathbf{d}^{\ell}) Q_{\Sigma} = z(\mathbf{E}'_{\mathbf{1}} \cdot \bar{\mathbf{E}}_{\mathbf{0}}^{-1} \cdot \bar{\mathbf{Q}}_{\mathbf{0}} \mp \mathbf{Q}_{\mathbf{0}}), \tag{3.55}$$

provided that Q_{Σ} is selected as in (3.53) and $z > z'_{max}$ or $z < z'_{min}$. From equations (3.54) and (3.55) one can see that the center-of-charge elevation z'_{Σ} relates the following vectors

$$\begin{aligned} &\mathbf{E_0} \cdot \bar{\mathbf{E}}_{\mathbf{0}}^{-1} \cdot (\bar{\mathbf{Q}}_{\mathbf{1}} - \bar{\mathbf{d}}_1^{\prime\prime\ell}) - \mathbf{E_0} \cdot \bar{\mathbf{E}}_{\mathbf{0}}^{-1} \cdot \bar{\mathbf{E}}_{\mathbf{1}} \cdot \bar{\mathbf{E}}_{\mathbf{0}}^{-1} \cdot (\bar{\mathbf{Q}}_{\mathbf{0}} - \bar{\mathbf{d}}_0^{\ell}) + \\ &\mathbf{E}''_{\mathbf{1}} \cdot \bar{\mathbf{E}}_{\mathbf{0}}^{-1} \cdot (\bar{\mathbf{Q}}_{\mathbf{0}} - \bar{\mathbf{d}}_0^{\ell}) \pm \mathbf{Q}''_{\mathbf{1}} = [\mathbf{E_0} \cdot \bar{\mathbf{E}}_{\mathbf{0}}^{-1} \cdot \bar{\mathbf{d}}_1^{\prime\ell} \pm \mathbf{d}^{\ell}] Q_{\Sigma} z'_{\Sigma}. \end{aligned} \tag{3.56}$$

Each row of this system of equations relates the charge values and locations in each observation layer m corresponding to each row of the system. It is clear that in each observation layer, the relationships have the same dependence on z'_{Σ} and so we must assume that there is a value of z'_{Σ} that simulatenously satifies the equations. Picking any m allows us to solve for z'_{Σ} as

$$\begin{aligned} &z'_{\Sigma} = \\ &[\mathbf{E_0} \cdot \bar{\mathbf{E}}_{\mathbf{0}}^{-1} \cdot (\bar{\mathbf{Q}}_{\mathbf{1}} - \bar{\mathbf{d}}_1^{\prime\prime\ell}) - \mathbf{E_0} \cdot \bar{\mathbf{E}}_{\mathbf{0}}^{-1} \cdot \bar{\mathbf{E}}_{\mathbf{1}} \cdot \bar{\mathbf{E}}_{\mathbf{0}}^{-1} \cdot (\bar{\mathbf{Q}}_{\mathbf{0}} - \bar{\mathbf{d}}_0^{\ell}) + \\ &\mathbf{E}''_{\mathbf{1}} \cdot \bar{\mathbf{E}}_{\mathbf{0}}^{-1} \cdot (\bar{\mathbf{Q}}_{\mathbf{0}} - \bar{\mathbf{d}}_0^{\ell}) \pm \mathbf{Q}''_{\mathbf{1}}]_m / ([\mathbf{E_0} \cdot \bar{\mathbf{E}}_{\mathbf{0}}^{-1} \cdot \bar{\mathbf{d}}_1^{\prime\ell} \pm \mathbf{d}^{\ell}]_m Q_{\Sigma}). \end{aligned} \tag{3.57}$$

In fact, it is true that each value of m will give the same value of z'_{Σ}.

Eliminating non-physical solutions

As is clear from (3.57) the solution of the center-of-charge location z'_{Σ} is dependent on the layer location of the center-of-charge ℓ. Consequently, there are $L-1$ solutions to (3.57) corresponding to $\ell = 0, \ldots, L-1$. We have numerically validated for numerous point distributions in anywhere from two to hundreds of layers that only one of the $L-1$ solutions for z'_{Σ} will satisfy the assumption that z'_{Σ} is located in layer ℓ. The other $L-2$ solutions explicitly

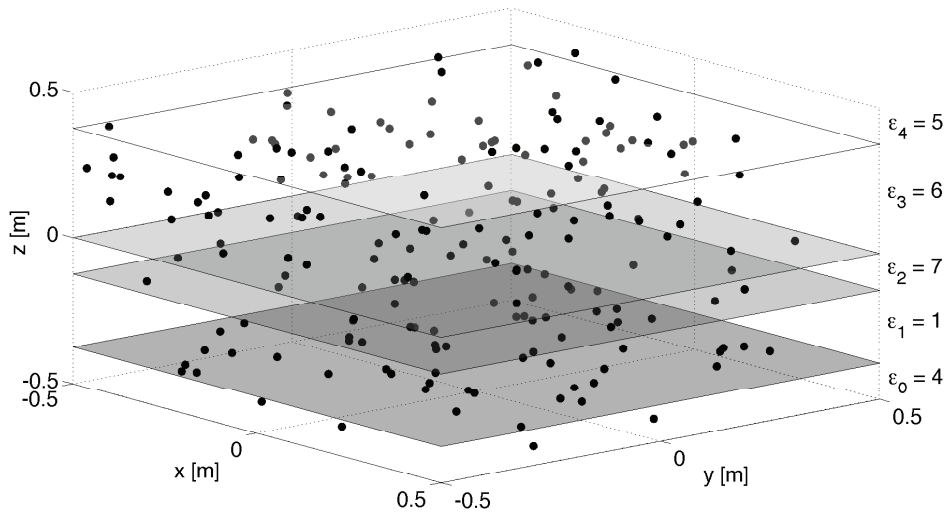

Figure 3.2: Random charge distribution of 200 point charges situated in a 5-layer medium. This distribution is used in the first set of experiments reported in the numerical results section.

violate this assumption by providing a value of z'_Σ located in some layer other than ℓ.

Comments

Although the methodology presented in the previous sections appears complicated, using the resulting expressions to determine an accurate center-of-charge location in layered media is straight-forward. It suffices to compute Q_Σ and $\boldsymbol{\rho}'_\Sigma$ from (3.18) followed by solving (3.57) with appropriately constructed matrices and vectors for the layered media under consideration.

3.3 Numerical results

3.3.1 Error behavior of the clustering approximation

In the following numerical examples we analyze the error behavior of the Barnes-Hut clustering approximation in multilayered media and compare it to the case when the effect of the inhomogeneity on the location of the center-of-charge is neglected.

Consider a random distribution of $N = 200$ charged points sources each carrying a random charge between 0 and 1 Coulomb and situated in a five-layered medium ($L = 5$) as shown in Fig. 3.2. The point coordinates are confined to a cube of size $c = 1[m]$. Associating the origin of the coordinate system with the cube's center, we compute the relative error in the electrostatic potential $\Phi(\boldsymbol{r}(R,\theta,\phi))$ given by (3.3) due to the Barnes-Hut clustering approximation $\Psi(\boldsymbol{r}(R,\theta,\phi),\boldsymbol{r}'_\Sigma)$ in (3.4) provided that the net charge Q_Σ, and its location $\boldsymbol{r}'_\Sigma$ are selected according to (3.18) and (3.57). The dependence of the error on angle θ is shown in Fig. 3.3 for radii of $R = 1[m]$, $R = 10[m]$, and $R = 100[m]$. The error is computed as the average relative error over all ϕ angles

$$\delta_\theta(R,\theta,\boldsymbol{r}'_\Sigma) = \int_0^{2\pi} \frac{|\Phi(\boldsymbol{r}(R,\theta,\phi)) - \Psi(\boldsymbol{r}(R,\theta,\phi),\boldsymbol{r}'_\Sigma)|}{2\pi|\Phi(\boldsymbol{r}(R,\theta,\phi))|} d\phi, \tag{3.58}$$

as a function of θ. For comparison, we show the same angular distribution of the relative error but in the case of the free-space clustering approximation $\Psi(\boldsymbol{r}(R,\theta,\phi),\boldsymbol{r}'^{fs}_\Sigma)$ with $\boldsymbol{r}'^{fs}_\Sigma$ given in (3.5). From the figure we observe that for most angles the multilayer center-of-charge produces an error significantly lower than the free-space center-of-charge at the same distance. Specifically, at $10[m]$ the multilayer center-of-charge produces an error nearly one-hundred times smaller than the equivalent free-space center-of-charge.

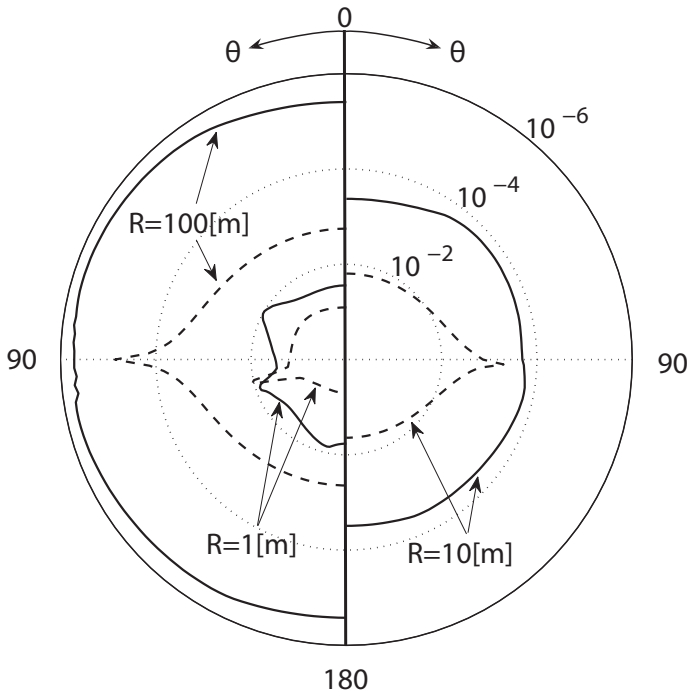

Figure 3.3: Plot of the relative error $\delta_\theta(R, \theta, \boldsymbol{r}'_\Sigma)$ versus angle θ for observation radiuses $R = 1[m]$, $R = 10[m]$, and $R = 100[m]$. The solid lines represent the relative error due to the novel clustering approximation (3.18), (3.57). The dashed lines represent the relative error due to the clustering approximation computed with the free-space formula (3.5).

For our next experiment we numerically demonstrate that for the same 200 point charge distribution, the z-coordinate of the center-of-charge computed according to formula (3.57) is indeed the location which yields the minimum error in the approximation of the true field (3.3) by the single-source field (3.4). For the purpose of this experiment we choose coordinates x'_Σ and y'_Σ according to the free-space formulae (3.18) and computed the average of the relative error

$$\delta(R, \tilde{\boldsymbol{r}}_\Sigma) = \int_0^{2\pi} \int_0^{\pi} \frac{|\Phi(\boldsymbol{r}(R,\theta,\phi)) - \Psi(\boldsymbol{r}(R,\theta,\phi), \tilde{\boldsymbol{r}}_\Sigma)|}{4\pi|\Phi(\boldsymbol{r}(R,\theta,\phi))|} \sin\theta d\theta d\phi, \tag{3.59}$$

as a function of coordinate $\tilde{z}_\Sigma$, (*i.e.*, $\tilde{\boldsymbol{r}}_\Sigma = x'_\Sigma \hat{\boldsymbol{x}} + y'_\Sigma \hat{\boldsymbol{y}} + \tilde{z}_\Sigma \hat{\boldsymbol{z}}$), within the span of the box height, $\tilde{z}_\Sigma \in [-c/2, c/2]$. The plot of the relative error $\delta(R, \tilde{\boldsymbol{r}}_\Sigma)$ versus the coordinate $\tilde{z}_\Sigma$ is shown in Fig. 3.4 for three observation radii. One can see that the theoretically predicted center-of-charge (3.57) coincides with the minimum of the numerically evaluated average relative error in the field approximation, i.e. at $\tilde{z}_\Sigma = z'_\Sigma$.

The dependence of the average relative error (3.59) on the radius of observation R is depicted in Fig. 3.5. One can observe when the inhomogeneity is properly accounted for the relative error $\delta(R, \boldsymbol{r}'_\Sigma)$ exhibits a $O(1/R^2)$ dependence while the relative error $\delta(R, \boldsymbol{r}'^{fs}_\Sigma)$ of the field approximation ignoring the effect of multilayered media on the location of the center-of-charge decays only as $O(1/R)$. It is also interesting to note that the error level achieved in the inhomogeneous model at $R = 10[m]$ is not observed in the free-space model until $R = 1000[m]$.

Our next experiment is to demonstrate that the clustering of charged sources in a multilayered media can be performed hierarchically in the same fashion as it can be done in free space. This property constitutes validating an extension of the hierarchical Barnes-Hut algorithm to the case of multilayered media, a fact that must be verified before the methodology we have presented can be applied to the acceleration of the capacitance extraction

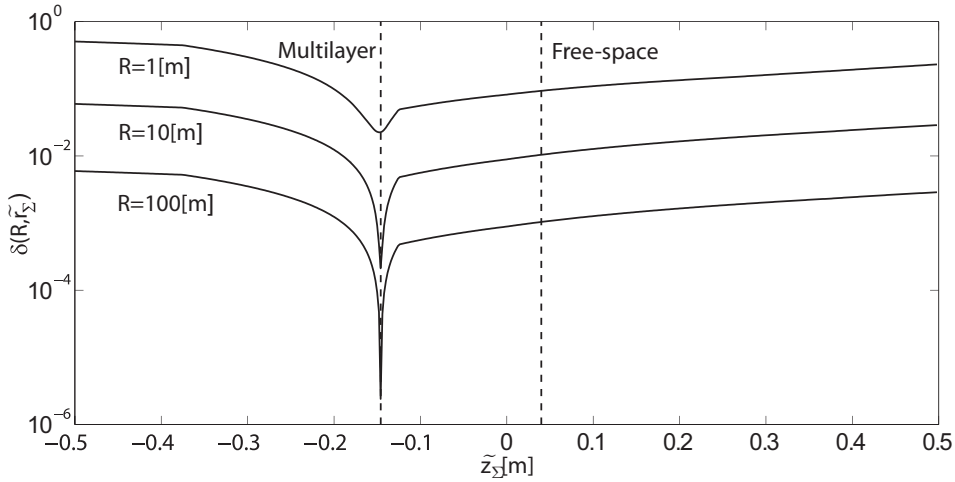

Figure 3.4: Plot of the relative error $\delta(R, \tilde{\boldsymbol{r}}_\Sigma)$ versus $\tilde{z}_\Sigma$ for observation radiuses $R = 1[m]$, $R = 10[m]$, and $R = 100[m]$. The vertical markers indicates the theoretical location of the center-of-charge elevation z'_Σ given by (3.57) and the center-of-charge elevation z'^{fs}_Σ in (3.5).

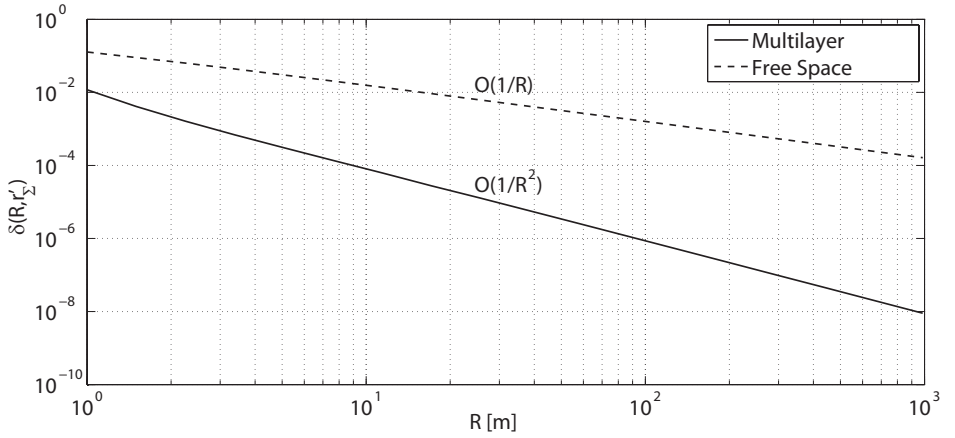

Figure 3.5: Plot of the average relative error $\delta(R, \boldsymbol{r}'_\Sigma)$ versus R for the value of center-of-charge elevation z'_Σ computed using formula (3.57) accounting for the inhomogeneity of multilayered space and the elevation of the center-of-charge z'^{fs}_Σ assuming the space to be homogeneous.

problem. A discussion of the hierarchical clustering performed by the Barnes-Hut algorithm is beyond the scope of this paper. Interested readers may find a sufficient discussion in [4].

For the purpose of this demonstration we consider a charged, perfectly conducting cube $1[m]$ in size, situated in a 4-layered media (Fig. 3.6). The surface of the cube is discretized using a triangular mesh of $P = 192$ patches with equal charge values assigned to the barycenter of each triangle. A two-level hierarchical partitioning of the geometry (2-level oct-tree) is also shown in Fig. 3.6. A box that bounds the entire geometry is selected as the root of the oct-tree and is denoted as Level 0 (in this case the cube itself coincides with the root of the tree). The cube is divided into eight Level 1 boxes that contain 24 triangles each. Level 2 boxes are then produced by subdividing each Level 1 box into eight boxes containing 2, 4, or 6 triangular patches depending on their location in the tree as shown in Fig. 3.6.

We begin hierarchically determining the center-of-charge of the cube by clustering the triangles in each of the 64 boxes at Level 2 of the oct-tree. This is accomplished by determining their respective centers-of-charge and net charges according to formulae (3.18) and (3.57). We then determine the centers-of-charge in each of the 8 boxes at Level 1 in two alternative ways. First, consider a box at Level 1 that spans layers 3 and 4 as shown in Fig. 3.6. For this box, we take each of the 24 individual patches it contains and compute its center-of-charge directly. In this fashion, the computed center-of-charge z'_Σ for the selected Level 1 box was computed from (3.57) as $0.739583[m]$. In comparison, we compute the center-of-charge of the same Level 1 box from (3.57) by using the 8 centers-of-charge computed for its Level 2 children. The center-of-charge elevation we obtain is $z'^h_\Sigma = 0.739582[m]$, where the superscript 'h' is used to denote that the result was obtained via 'hierarchical' clustering. The difference in the last digit between z'_Σ and z'^h_Σ can be attributed to round-off error in single precision arithmetic. Similarly, it has been verified that the center-of-charge for the root box at Level 0 computed directly and hierarchically also

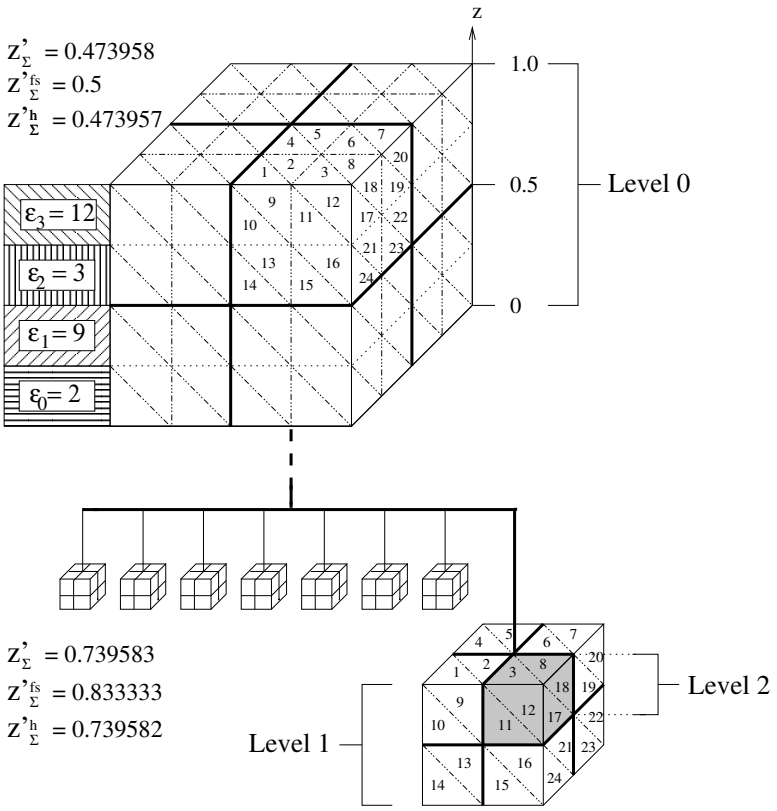

Figure 3.6: Group of arbitrary charged sources situated in general multilayered media. Different markers depict groups of charges confined within distinct layers. Larger size markers denote partial centers-of-charge for distinct layers.

coincide. A direct computation using each of the $P = 192$ sources contained in the root box gives a center-of-charge elevation $z'_\Sigma = 0.473958[m]$ while the center-of-charge of the Level 0 box determined from the 8 centers-of-charge of its Level 1 children gives $z^{th}_\Sigma = 0.473957[m]$. The computed values of the center-of-charges are also summarized in Fig. 3.6.

This numerical demonstration shows that hierarchical clustering of charged sources in multilayered media can be performed using the multilayer center-of-charge analogously to the case of a homogeneous medium.

3.3.2 Capacitance extraction comparison against Ansoft's Q3D Extractor

In order to validate our proposed center-of-charge clustering approximation and demonstrate its practical significance, we incorporated our method into the Barnes-Hut accelerated capacitance extraction algorithm described in [30] and conducted capacitance extraction for 7 nets of IBM's Plasma package[1] depicted in Fig. 3.7. The first column of the resulting capacitance matrix was compared with the one obtained with Ansoft's Q3D Extractor [36] and those results are given in Table I. The weakest mutual capacitance is observed between nets 1 and 6 with over 30 times attenuation compared to the self capacitance. The difference in that interaction compared to Q3D Extractor did not exceed 2.4%. Q3D Extractor utilizes a boundary element formulation that discretizes the surfaces of both the conductors and the dielectric interfaces. This discretization allows Q3D Extractor to accelerate the matrix-vector products using the fast multipole method with the homogeneous space kernel [6]. In the example illustrated in Fig. 3.7, Q3D Extractor utilized $144,580$ elements for the conductor surface and $303,716$ elements for the dielectric interfaces. The run time for Q3D Extractor was $1,524$ seconds with a peak memory allocation of $2,400$ megabytes. The $144,580$-element surface mesh of the conductors created by the Q3D Extractor solver was subsequently utilized in the Barnes-Hut algorithm. The run time for the Barnes-Hut solver was 337 seconds with a peak memory usage of 510 megabytes. The tolerance in the diagonally preconditioned GMRES matrix equation solver was set to 0.001. The simulations were performed on a single 3.0GHz Intel Xeon E5472 CPU core.

[1] Courtesy of Alpha Group, IBM T.J. Watson Research Center.

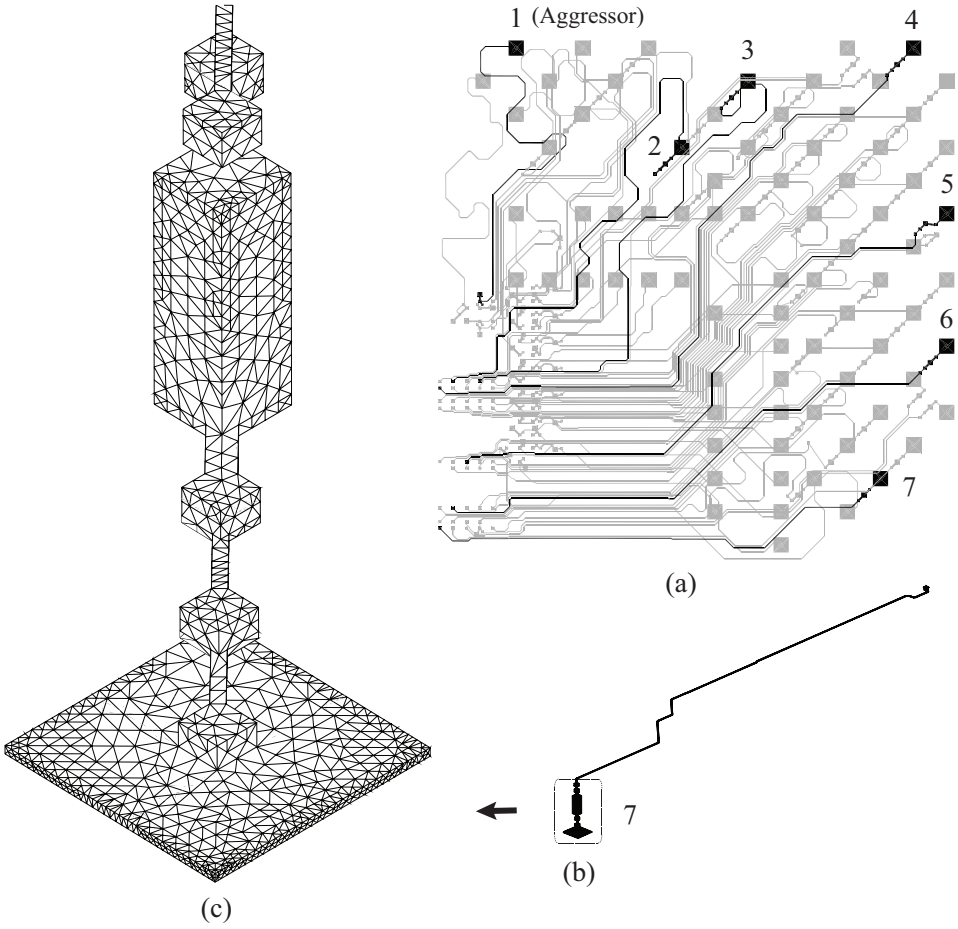

Figure 3.7: (a) A 75-net fragment of the IBM Plasma package implemented in 7-layer process with relative permittivities ϵ_0 through ϵ_8 equal to 1, 3.5, 4.4, 3.5, 4.4, 3.5, 4.4, 3.5, and 1, respectively, and the dielectric interface locations a_0 through a_7 equal to $16\mu m$, $62\mu m$, $108\mu m$, $162\mu m$, $562\mu m$, $616\mu m$, $670\mu m$ and $732\mu m$, respectively. Capacitance is extracted for the highlighted seven signal nets. (b) Close-up depiction of the 7th net geometry and its surface mesh (c) containing $15,748$ triangular elements.

Table 3.1: First column of the capacitance matrix for 7 nets of IBM's Plasma Package

	Capacitance $[fF]$						
	1	2	3	4	5	6	7
Q3D Extractor	265.3	-89.2	-26.3	-22.2	-11.6	-8.4	-8.6
Barnes-Hut	264.5	-88.7	-26.2	-22.4	-11.7	-8.6	-8.4

3.3.3 Matrix-vector product comparison against FastCap

As Ansoft's Q3D Extractor software does not provide detailed runtime statistics for individual matrix-vector products, we could not use it for comparison of its fast multipole method accelerated matrix-vector product against that in the proposed Barnes-Hut algorithm. For that purpose we utilized the FastCap [8] software which uses a similar approach for handling the conductors in multilayered media to the one implemented in Q3D Extractor. Namely, it discretizes surfaces of both the dielectric interfaces and the conductors and uses the homogeneous-space kernel fast multipole method to accelerate the matrix-vector product. The geometry of a cross-bar structure embedded in 15-layer process simulated using FastCap and our proposed algorithm is shown in Fig. 3.8. The relative permittivities of layers ϵ_0 through ϵ_{14} are equal to 1, 3.5, 1, 4.4, 1, 3.5, 1, 4.4, 1, 3.5, 1, 4.4, 1, 3.5, and 1. The elevations of layer interfaces a_0 through a_{13} are $16\mu m$, $49\mu m$, $62\mu m$, $95\mu m$, $108\mu m$, $141\mu m$, $162\mu m$, $562\mu m$, $583\mu m$, $616\mu m$, $637\mu m$, $670\mu m$, $683\mu m$, and $732\mu m$, respectively. Each of the 42 identical conductors forming the cross-bar interconnect is $200\mu m$ long, $18.9\mu m$ wide, and $12\mu m$ thick. The lateral spacing between the conductors is $18.9\mu m$ while the elevations of the bottom planes of each of the 7 metal layers are $26\mu m$, $72\mu m$, $118\mu m$, $362\mu m$, $593\mu m$, $647\mu m$, and $703\mu m$, respectively. The lateral dimensions of the layers are $2mm \times 2mm$ with the lateral geometric

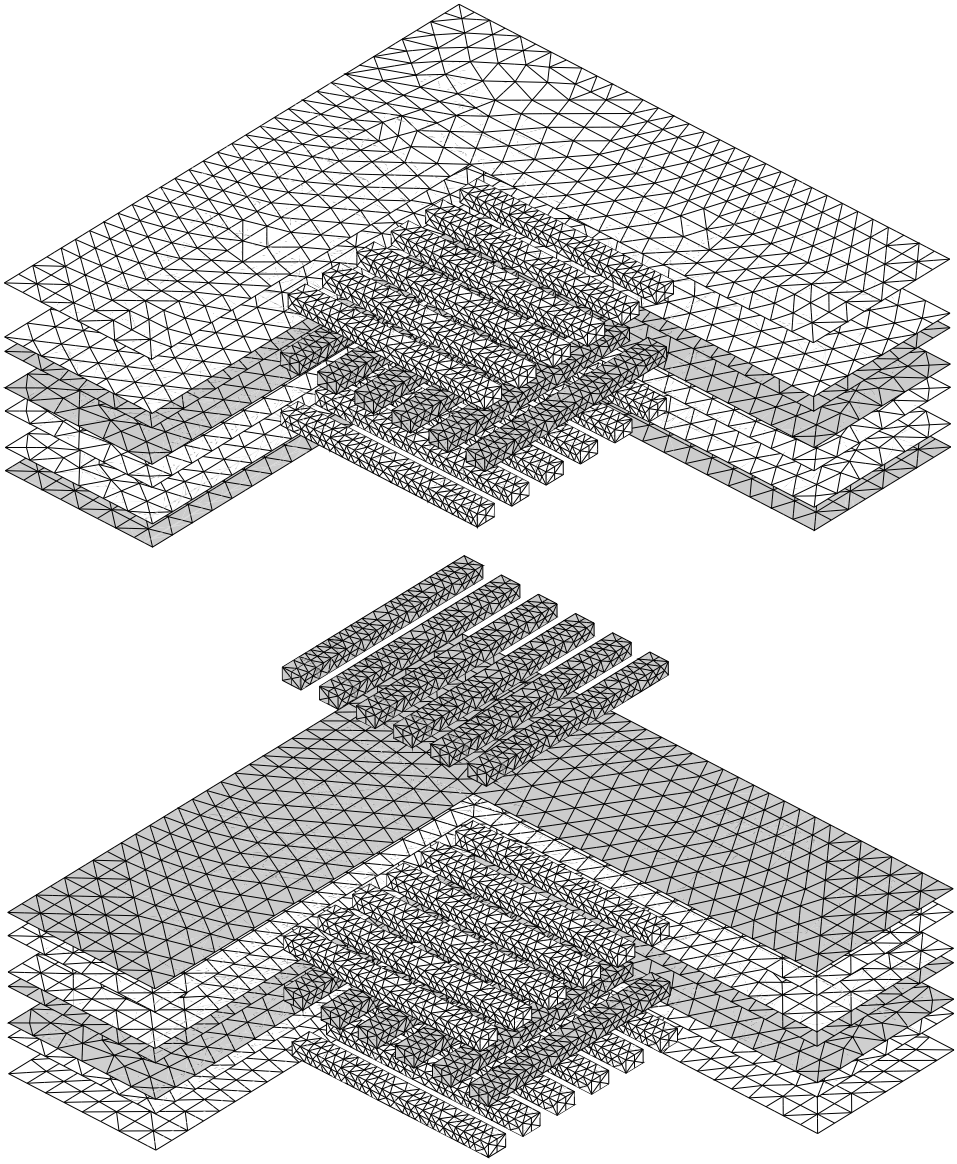

Figure 3.8: Geometry of a cross-bar interconnect of 42 conductors embedded in 15 layer process. Details of the geometry are given in the text. In addition to the $35,120$-element mesh on the conductor surfaces utilized in our proposed algorithm the figure shows fragments of the $39,968$-element surface meshes discretizing the dielectric layer interfaces in FastCap. To clarify the design only a fragment of the dielectric layer interfaces is shown.

center coinciding with that of the cross-bar interconnect. The surface of the conductors are discretized into $35,120$ elements, while the dielectric interfaces are discretized into $39,968$ elements.

In order to ensure the same order of approximation error FastCap was set to use second order multipole expansions [7]. The Barnes-Hut clustering parameter was set to $\theta = 1/(\sqrt{3}/2 + 1) = 0.54$. This value corresponds to a near interaction radius of $\sqrt{3}/2 + 1$ box widths in the Barnes-Hut tree which is equivalent to the radius used by the fast multipole method in FastCap. The preconditioner was turned off in FastCap to improve its matrix-vector product performance.

Each matrix-vector product in the Barnes-Hut solver took 0.34 seconds on average compared to 2.04 seconds for FastCap. The total memory used by the Barnes-Hut solver was 130 megabytes while the peak memory usage by FastCap was $3,900$ megabytes. In this experiment, we observed that the new Barnes-Hut clustering approximation adds approximately 2% to the overall matrix-vector product runtime compared to the free-space center-of-charge approximation. It is important to note that since the free-space center-of-charge is faster to compute, it should be used when all sources are located in a single layer.

This numerical comparison shows that the Barnes-Hut algorithm is a competitive alternative to the fast multipole method for capacitance extraction when two digits of accuracy is sufficient. We would also like to point the interested reader to the numerical results in [7] which indicate that the Barnes-Hut algorithm is approximately ten times faster than the fast multipole method for capacitance extraction in homogeneous media.

3.4 Conclusion

This paper describes an extension of the free-space center-of-charge approximation to inhomogeneous stratified media. The expressions for the new center-

of-charge (3.18) and (3.57) are easily computable from knowledge of the charge distribution in the layered medium. When computed appropriately, the multilayered center-of-charge has been shown to have the desired $O(1/R^3)$ absolute and $O(1/R^2)$ relative error behaviour. Although the asymptotic behaviour of the multilayer center-of-charge mimics that of the free-space center-of-charge in planar media, we have also shown that for fixed distances, the multilayer center-of-charge is significantly more accurate on average. Hierarchical clustering of the multilayer center-of-charge is shown to behave analogously to free-space hierarchical clustering. The extension of the proposed Barnes-Hut acceleration scheme for capacitance extraction in multilayered media is demonstrated.

3.5 Appendix: Error Analysis of the Multilayer Center-of-Charge Approximation

The error induced when approximating the true field $\Phi_m(\boldsymbol{r})$ in (3.8) by the field of the center-of-charge Ψ_m^ℓ located at $\boldsymbol{r}'_\Sigma$ in (3.11) is

$$\Phi_m(\boldsymbol{r}) - \Psi_m^\ell(\boldsymbol{r}, \boldsymbol{r}'_\Sigma) = \frac{1}{4\pi^2} \int_0^{2\pi} \int_0^\infty \Delta_m(\lambda, \alpha) e^{-i\boldsymbol{\lambda}\cdot\boldsymbol{\rho}} d\lambda d\alpha. \tag{3.60}$$

where $\Delta_m(\lambda, \alpha)$ is the difference between the true and approximate spectra (3.9) and (3.12)

$$\Delta_m(\lambda, \alpha) = \phi_m(\lambda, \alpha) - \psi_m^\ell(\lambda, \alpha). \tag{3.61}$$

Substitution of (3.9) and (3.12) into (3.60) yields

$$\begin{aligned} \Delta_m(\lambda, \alpha) = \sum_{l=0}^{L-1} \sum_{n=0}^{N^l-1} & q_n^l \hat{g}_m^l(\lambda, z, z_n'^l) e^{i\boldsymbol{\lambda}\cdot\boldsymbol{\rho}'_n} \\ & - Q_\Sigma \hat{g}_m^\ell(\lambda, z, z'_\Sigma) e^{i\boldsymbol{\lambda}\cdot\boldsymbol{\rho}'_\Sigma}. \end{aligned} \tag{3.62}$$

It is convenient to distinguish between errors incurred by clustering sources over the XY plane, $\Delta_m^\rho(\lambda, \alpha)$, and those due to clustering sources over the z

coordinate, $\Delta_m^z(\lambda)$. Then the total error may be written as

$$\Delta_m(\lambda,\alpha) = \Delta_m^\rho(\lambda,\alpha) + \Delta_m^z(\lambda), \tag{3.63}$$

where

$$\begin{aligned}\Delta_m^\rho(\lambda,\alpha) = \sum_{l=0}^{L-1}\sum_{n=0}^{N^l-1} q_n^l \hat{g}_m^l(\lambda,z,z_n'^l)(e^{i\boldsymbol{\lambda}\cdot\boldsymbol{\rho}_n'} - 1) \\ -Q_\Sigma \hat{g}_m^\ell(\lambda,z,z_\Sigma')(e^{i\boldsymbol{\lambda}\cdot\boldsymbol{\rho}_\Sigma'} - 1).\end{aligned} \tag{3.64}$$

$$\Delta_m^z(\lambda) = \sum_{l=0}^{L-1}\sum_{n=0}^{N^l-1} q_n^l \hat{g}_m^l(\lambda,z,z_n'^l) - Q_\Sigma \hat{g}_m^\ell(\lambda,z,z_\Sigma'), \tag{3.65}$$

Below, a detailed analysis of these two error contributions is provided. This analysis is broken into regions based on the validity of the multilayer center-of-charge approximation as discussed in the body of this work.

3.5.1 Asymptotic error at $|z| \to \infty$

First, we consider the half-space domains external to the layers containing the sources, *i.e.,* external to $z < \min(a_0, z'_{min})$ or $z > \max(a_{L-2}, z'_{max})$. In these regions, the multilayer center-of-charge approximation is strictly valid. Additionally, the z-dependent factor of the spectrum of the true, (3.23), and approximating, (3.24), fields is contained in a factor $e^{-\lambda|z|}$ which can be extracted and associated with rapidly changing part of the spectrum prior to asymptotic analysis. Therefore we represent the true and approximated field as

$$\begin{aligned}\dot{\phi}_m(\lambda) = \sum_{l=0}^{L-1}\sum_{n=0}^{N^l-1} q_n^l \hat{g}_m^l(\lambda,z,z_n'^l) = \\ e^{-\lambda|z|}\sum_{l=0}^{L-1}\sum_{n=0}^{N^l-1} q_n^l \hat{\gamma}_m^l(\lambda,z_n'^l),\end{aligned} \tag{3.66}$$

$$\dot{\psi}_m^\ell(\lambda) = Q_\Sigma \hat{g}_m^\ell(\lambda,z,z_\Sigma') = Q_\Sigma e^{-\lambda|z|}\hat{\gamma}_m^\ell(\lambda,z_\Sigma'), \tag{3.67}$$

where $m = 0$ or $m = L-1$ and where $\hat{g}_m^l = e^{-\lambda|z|}\hat{\gamma}_m^l$. Choosing the net charge according to (3.18) and the center-of-charge elevation z'_Σ according to (3.18) and (3.57) satisfies the equations (3.15) and (3.17). As a result we may write

$$\sum_{l=0}^{L-1}\sum_{n=0}^{N^l-1} q_n^l \hat{\gamma}_m^l(0, z_n'^l) = Q_\Sigma \hat{\gamma}_2^\ell(0, z'_\Sigma), \tag{3.68}$$

$$\sum_{l=0}^{L-1}\sum_{n=0}^{N^l-1} q_n^l \partial_\lambda \hat{\gamma}_m^l(0, z_n'^l) = Q_\Sigma \partial_\lambda \hat{\gamma}_2^\ell(0, z'_\Sigma), \tag{3.69}$$

and it becomes clear that the leading term in the error $\Delta_m^z(\lambda)$ near the point $\lambda = 0$ is proportional to λ^2

$$\begin{aligned}\Delta_m^z(\lambda) &= \lambda^2 e^{-\lambda|z|}\times \\ &\frac{1}{2}\left(\sum_{l=0}^{L-1}\sum_{n=0}^{N^l-1} q_n^l \partial_\lambda^2 \hat{\gamma}_m^l(0, z_n'^l) - Q_\Sigma \partial_\lambda^2 \hat{\gamma}_2^\ell(0, z'_\Sigma)\right).\end{aligned} \tag{3.70}$$

We wish to point out that the *only* dependence on z in the above equation is in the exponential term.

When $|z| \gg 1$, the error contribution to the potential difference $\Phi_m(\boldsymbol{r}) - \Psi_m^\ell(\boldsymbol{r}, \boldsymbol{r}'_\Sigma)$ from clustering sources over the z coordinate is given by

$$\begin{aligned}\frac{1}{4\pi^2}\int_0^\infty\int_0^{2\pi} \Delta_m^z(\lambda) e^{-i\boldsymbol{\lambda}\cdot\boldsymbol{\rho}} d\lambda d\alpha \sim \\ \frac{1}{2\pi}\int_0^\infty \lambda^2 e^{-\lambda|z|} J_0(\lambda\rho) d\lambda = O\left(\frac{1}{R^3}\right),\end{aligned} \tag{3.71}$$

where $\rho = |\boldsymbol{\rho}|$ and where $R = \sqrt{\rho^2 + z^2}$. In the evaluation of (3.65) the following identities where used [35], [7]

$$\frac{1}{2\pi}\int_0^{2\pi} e^{-i\boldsymbol{\lambda}\cdot\boldsymbol{\rho} - i\nu\alpha + i\nu\pi/2} d\alpha = J_\nu(\lambda\rho), \tag{3.72}$$

$$\int_0^\infty \lambda^n e^{-\lambda|z|} J_m(\lambda\rho) d\lambda \sim \frac{P_n^m(\cos\theta)}{r^{n+1}}, \tag{3.73}$$

where, $\cos\theta = z/r$.

Now consider the behavior of $\Delta_m^\rho(\lambda,\alpha)$ spectral error in the vicinity of the stationary phase point. The first-order expansion of (3.64) is

$$\begin{aligned}\Delta_m^\rho(\lambda,\alpha) = e^{-\lambda|z|}\sum_{l=0}^{L-1}\sum_{n=0}^{N^l-1} q_n^l[\hat\gamma_m^l(0,z_n'^l)+\lambda\times\\ \partial_\lambda\hat\gamma_m^l(0,z_n'^l)+\ldots][i\boldsymbol{\lambda}\cdot\boldsymbol{\rho}_n'+\ldots]-Q_\Sigma e^{-\lambda|z|}\times\\ [\hat\gamma_m^\ell(0,z_\Sigma')+\lambda\partial_\lambda\hat\gamma_m^\ell(0,z_\Sigma')+\ldots][i\boldsymbol{\lambda}\cdot\boldsymbol{\rho}_\Sigma'+\ldots].\end{aligned} \tag{3.74}$$

Provided that Q_Σ, x_Σ' and y_Σ' satisfy (3.15) and (3.16), and noting that the first order terms for any $\hat\gamma$ all have the same constant value at $\lambda=0$, the error due to clustering sources over XY simplifies to

$$\begin{aligned}\Delta_m^\rho(\lambda,\alpha) =& i\lambda^2 e^{-\lambda|z|}\sum_{l=0}^{L-1}\sum_{n=0}^{N^l-1} q_n^l\partial_\lambda\hat\gamma_m^l(0,z_n'^l)\hat{\boldsymbol{\lambda}}\cdot\boldsymbol{\rho}_n'\\ &-i\lambda^2 e^{-\lambda|z|}Q_\Sigma\partial_\lambda\hat\gamma_m^\ell(0,z_\Sigma')\hat{\boldsymbol{\lambda}}\cdot\boldsymbol{\rho}_\Sigma'.\end{aligned} \tag{3.75}$$

Thus, $\Delta_m^\rho(\lambda,\alpha)$ is proportional to λ^2 near the point $\lambda=0$ regardless of whether or not equation (3.18) is satisfied through the appropriate choice of center-of-charge elevation z_Σ' from (3.57). Expanding $\Delta_m^\rho(\lambda,\alpha)$ into a Fourier series over the spectral angle α

$$\Delta_m^\rho(\lambda,\alpha) = \lambda^2 e^{-\lambda z}\sum_{\nu=-\infty}^{+\infty}\beta_\nu e^{-i\nu\alpha}, \tag{3.76}$$

we obtain the contribution into the spatial error $\Phi_m(\boldsymbol{r})-\Psi_m^\ell(\boldsymbol{r},\boldsymbol{r}_\Sigma')$ from $\Delta_m^\rho(\lambda,\alpha)$ as

$$\begin{aligned}&\frac{1}{4\pi^2}\int_0^\infty\int_0^{2\pi}\Delta_m^\rho(\lambda,\alpha)e^{-i\boldsymbol{\lambda}\cdot\boldsymbol{\rho}}d\lambda d\alpha =\\ &\frac{1}{2\pi}\sum_{\nu=-\infty}^{+\infty}\beta_\nu e^{i\nu\pi/2}\int_0^\infty\lambda^2 e^{-\lambda z}J_\nu(\lambda\rho)d\lambda = O\left(\frac{1}{R^3}\right).\end{aligned} \tag{3.77}$$

3.5.2 Asymptotic error at $\rho\to\infty$: $z\in[z'_{min},z'_{max}]$

When the observation point elevation z lies within the source box boundaries $z'_{min}<z<z'_{max}$, the multilayer center-of-charge formulation is not strictly

valid. However, formulas of the form (3.23) and (3.24) still describe the z-dependence of the true and approximating field, respectively

$$\begin{aligned}\dot{\phi}_m(\lambda) = &\sum_{l=0}^{L-1}\sum_{n=0}^{N^l-1} q_n^l \hat{g}_m^l(\lambda, z, z_n'^l) = \frac{e^{-\lambda(z-a_{m-1})}}{2\varepsilon_0\epsilon_m} \\ &\sum_{l=0}^{L-1}\sum_{n=0}^{N^l-1} q_n^l \hat{\gamma}_m^{l-}(\lambda, z_n'^l) + \frac{e^{-\lambda(a_m-z)}}{2\varepsilon_0\epsilon_m} \\ &\sum_{l=0}^{L-1}\sum_{n=0}^{N^l-1} q_n^l \hat{\gamma}_m^{l+}(\lambda, z_n'^l) + \sum_{n=0}^{N^m-1} \frac{q_n^l e^{-\lambda|z-z_n'^m|}}{2\varepsilon_0\epsilon_m},\end{aligned} \tag{3.78}$$

$$\begin{aligned}\dot{\psi}_m^\ell(\lambda) = Q_\Sigma \hat{g}_m^\ell(\lambda, z, z_\Sigma') = &\frac{Q_\Sigma \hat{\gamma}_m^{\ell-}(\lambda, z_\Sigma')e^{-\lambda(z-a_{m-1})}}{2\varepsilon_0\epsilon_m} \\ + \frac{Q_\Sigma \hat{\gamma}_m^{\ell+}(\lambda, z_\Sigma')e^{-\lambda(a_m-z)}}{2\varepsilon_0\epsilon_m} &+ \frac{Q_\Sigma \delta_{m\ell} e^{-\lambda|z-z_\Sigma'|}}{2\varepsilon_0\epsilon_m},\end{aligned} \tag{3.79}$$

where $a_{m-1} \le z \le a_m$. By virtue of (3.15), the error $\Delta_m^z(\lambda)$ due to clustering over the z-coordinate is obtained from (3.78) and (3.79) as

$$\begin{aligned}\Delta_m^z(\lambda) = &\frac{\lambda e^{-\lambda(z-a_{m-1})}}{2\varepsilon_0\epsilon_m} \\ &\left(\sum_{l=0}^{L-1}\sum_{n=0}^{N^l-1} q_n^l \partial_\lambda \hat{\gamma}_m^{l-}(0, z_n'^l) - Q_\Sigma \partial_\lambda \hat{\gamma}_m^{\ell-}(0, z_\Sigma')\right) + \\ &\frac{\lambda e^{-\lambda(a_m-z)}}{2\varepsilon_0\epsilon_m}\left(\sum_{l=0}^{L-1}\sum_{n=0}^{N^l-1} q_n^l \partial_\lambda \hat{\gamma}_m^{l+}(0, z_n'^l) - Q_\Sigma \hat{\gamma}_m^{\ell+}(0, z_\Sigma')\right) \\ &+ \sum_{n=0}^{N^m-1} \frac{q_n^l(e^{-\lambda|z-z_n'^m|}-1)}{2\varepsilon_0\epsilon_m} - \frac{Q_\Sigma\delta_{m\ell}(e^{-\lambda|z-z_\Sigma'|}-1)}{2\varepsilon_0\epsilon_m},\end{aligned} \tag{3.80}$$

where once again we have used the fact that the first order terms of any $\hat{\gamma}$ at $\lambda = 0$ are equal and constant.

The inverse Fourier-Hankel transform of the spectral terms containing $\lambda e^{-\lambda|z-a|}$ in (3.80) are easily evaluated with aid of identity (3.73). This yields a spatial dependency proportional to the Legendre polynomial $P_1(|z-a|/\rho)/(\rho^2+(z-a)^2) = O(\rho^{-3})$ when $\rho \gg 1$. The same $O(\rho^{-3})$ spatial dependence is featured by the inverse Fourier-Hankel transform of the $e^{-\lambda|z-z'|} - 1$ terms in

(3.80) giving

$$\int_0^\infty (e^{-\lambda|z-z'|}-1)J_0(\lambda\rho)d\lambda = \frac{1}{\rho}\left(\frac{1}{\sqrt{1+(z-z')^2/\rho^2}}-1\right) = O\left(\frac{(z-z')^2}{\rho^3}\right), \tag{3.81}$$

when $\rho \gg |z-z'|$. Thus, the contribution into the spatial error $\Phi_m(\boldsymbol{r}) - \Psi_m^\ell(\boldsymbol{r},\boldsymbol{r}'_\Sigma)$ from $\Delta_m^z(\lambda)$ decays as $O(1/\rho^3)$ when the observation point elevation is within the source layers even though the error is only proportional to λ near the stationary phase point.

Analogous to the preceeding procedure, it can be shown that when $z \in [z'_{min}, z'_{max}]$ the error $\Delta_m^\rho(\lambda)$ due to clustering sources in the XY plane behaves proportionally to λ^2 near the point $\lambda = 0$. Therefore, according to (3.73) its contribution to the spatial error $|\Phi_m(\boldsymbol{r}) - \Psi_m^\ell(\boldsymbol{r},\boldsymbol{r}'_\Sigma)|$ is $O(1/\rho^3)$.

3.5.3 Asymptotic error at $\rho \to \infty$: $z \notin [z'_{min}, z'_{max}]$

Outside the interval $z \in [z'_{min}, z'_{max}]$ enclosing the sources, the choice of center-of-charge elevation (3.57) ensures a spectral match between both the zeroth and first powers of λ in the vicinity of stationary phase point $\lambda = 0$. Hence, the clustering error introduced by grouping sources over the z coordinate (3.65) is proportional to λ^2 at the point $\lambda = 0$

$$\Delta_m^z(\lambda) \simeq \lambda^2 \left(\sum_{l=0}^{L-1} \sum_{n=0}^{N^l-1} q_n^l \partial_\lambda^2 \hat{g}_m^l(0,z,z_n'^l) - Q_\Sigma \partial_\lambda^2 \hat{g}_m^\ell(0,z,z'_\Sigma) \right), \quad \lambda \to 0. \tag{3.82}$$

Once again, from identity (3.73), the error contribution from $\Delta_m^z(\lambda)$ to the total spatial approximation error $|\Phi_m(\boldsymbol{r}) - \Psi_m^\ell(\boldsymbol{r},\boldsymbol{r}'_\Sigma)|$ is $O(1/\rho^3)$.

The error (3.64) due to clustering of sources in XY plane in this region can be written analogously to (3.75) without extracting the exponential term. Then, a procedure similar to that used to obtain (3.77) proves that the error behavior is also $O(1/\rho^3)$.

Acknowledgement

The authors would like to thank Dr. Feng Ling for making his Green's function evaluation utility for multilayered media available to us.

References

[1] R. F. Harrington, *Field Computation by Moment Methods*. Wiley-IEEE Press, 1993.

[2] A. Hellemans and M. Mukerjee, "Computing the cosmos," *Spectrum, IEEE*, vol. 41, no. 8, pp. 28–34, Aug. 2004.

[3] A. W. Appel, "An efficient program for many-body simulation," *SIAM Journal on Scientific and Statistical Computing*, vol. 6, no. 1, pp. 85–103, Jan. 1985.

[4] J. Barnes and P. Hut, "A hierarchical O(N log N) force-calculation algorithm," *Nature*, vol. 324, pp. 446–449, Dec. 1986.

[5] L. Greengard and V. Rokhlin, "A fast algorithm for particle simulations," *J. Comput. Phys.*, vol. 73, no. 2, pp. 325–348, 1987.

[6] ——, "A new version of the fast multipole method for the laplace equation in three dimensions," Yale University, Tech. Rep. YALEU/DCS/RR-1115, Sept. 1996.

[7] L. Jiang, "Studies on low frequency fast multipole algorithms," Ph.D. dissertation, University of Illinois at Urbana-Champaign, 2004.

[8] K. Nabors and J. White, "Fastcap: a multipole accelerated 3-d capacitance extraction program," *Computer-Aided Design of Integrated Circuits and Systems, IEEE Transactions on*, vol. 10, no. 11, pp. 1447–1459, Nov 1991.

[9] K. Nabors, S. Kim, and J. White, "Fast capacitance extraction of general three-dimensional structures," *Microwave Theory and Techniques, IEEE Transactions on*, vol. 40, no. 7, pp. 1496–1506, Jul 1992.

[10] V. Jandhyala, E. Michielssen, and R. Mittra, "Multipole-accelerated capacitance computation for 3-d structures in a stratified dielectric medium using a closed form green's function," *Int. J. Microwave and Millimeter-Wave Computer-Aided Eng*, no. 5, pp. 68–78, 1995.

[11] ——, "A memory-efficient, adaptive algorithm for multipole-accelerated capacitance computation in a stratified dielectric medium," *International Journal of Microwave and Millimeter-Wave Computer-Aided Engineering*, vol. 6, no. 6, pp. 381–390, 1996.

[12] Y. Pan, "Development of the fast multipole method for stratified medium," Ph.D. dissertation, University of Illinois at Urbana-Champaign, 2002.

[13] Y. Pan, W. Chew, and L. Wan, "A fast multipole-method-based calculation of the capacitance matrix for multiple conductors above stratified dielectric media," *Microwave Theory and Techniques, IEEE Transactions on*, vol. 49, no. 3, pp. 480–490, Mar 2001.

[14] Y. C. Pan and W. C. Chew, "A hierarchical fast-multipole method for stratified media," *Microwave and Optical Technology Letters*, vol. 27, no. 1, pp. 13–17, 2000.

[15] L. Jiang, W. Chew, and Y. Pan, "Dcim-accelerated smfma for capacitance extraction," *Antennas and Propagation Society International Symposium, 2003. IEEE*, vol. 1, pp. 47–50 vol.1, June 2003.

[16] Y. L. L. Coz and R. B. Iverson, "A stochastic algorithm for high speed capacitance extraction in integrated circuits," *Solid State Electronics*, no. 53, pp. 1005–1012, 1992.

[17] S. Kapur and D. E. Long, "Ies3: a fast integral equation solver for efficient 3-dimensional extraction," in *ICCAD '97: Proceedings of the 1997 IEEE/ACM international conference on Computer-aided design*. Washington, DC, USA: IEEE Computer Society, 1997, pp. 448–455.

[18] D. Gope and V. Jandhyala, "Pilot: A fast algorithm for enhanced 3d parasitic capacitance extraction efficiency," *Microwave and Optical Technology Letters*, vol. 41, no. 3, pp. 169–173, 2004.

[19] W. Shi, J. Liu, N. Kakani, and T. Yu, "A fast hierarchical algorithm for 3-d capacitance extraction," *Proc. Design Automation Conf.*, pp. 212–217, 1998.

[20] ——, "A fast hierarchical algorithm for three-dimensional capacitance extraction," *Computer-Aided Design of Integrated Circuits and Systems, IEEE Transactions on*, vol. 21, no. 3, pp. 330–336, Mar 2002.

[21] T. Lu, Z. Wang, and W. Yu, "Hierarchical block boundary-element method (hbbem): a fast field solver for 3-d capacitance extraction," *Microwave Theory and Techniques, IEEE Transactions on*, vol. 52, no. 1, pp. 10–19, Jan. 2004.

[22] L. J. Jiang, B. J. Rubin, J. D. Morsey, H. T. Hu, and A. Elfadel, "Novel capacitance extraction method using direct boundary integral equation method and hierarchical approach," *IEEE Topical Meeting on Electrical Performance of Electronic Packaging*, pp. 331–334, Oct. 2006.

[23] [Online]. Available: http://www.alphaworks.ibm.com/tech/eip

[24] J. Phillips and J. White, "Efficient capacitance extraction of 3d structures using generalized pre-corrected fft methods," *IEEE Topical Meeting on Electrical Performance of Electronic Packaging*, pp. 253–256, Nov 1994.

[25] ——, "A precorrected-fft method for electrostatic analysis of complicated 3-d structures," *Computer-Aided Design of Integrated Circuits and Systems, IEEE Transactions on*, vol. 16, no. 10, pp. 1059–1072, Oct 1997.

[26] E. Bleszynski, M. Bleszynski, and T. Jaroszewicz, "A fast integral-equation solver for electromagnetic scattering problems," *Antennas and Propagation Society International Symposium, 1994. AP-S. Digest*, vol. 1, pp. 416–419 vol.1, Jun 1994.

[27] ——, "Aim: Adaptive integral method for solving large-scale electromagnetic scattering and radiation problems," *Radio Science*, vol. 31, no. 5, pp. 1225–1251, 1996.

[28] M. Catedra, R. Torres, E. Gago, and J. Basterrechea, *The CG-FFT Method: Application of Signal Processing Techniques to Electromagnetics*. Artech House, 1995.

[29] F. Ling, V. Okhmatovski, W. Harris, S. McCracken, and A. Dengi, "Large-scale broad-band parasitic extraction for fast layout verification of 3-d rf and mixed-signal on-chip structures," *Microwave Theory and Techniques, IEEE Transactions on*, vol. 53, no. 1, pp. 264–273, Jan. 2005.

[30] M. Al-Qedra, P. Saleh, F. Ling, and V. Okhmatovski, "Barnes-Hut accelerated capacitance extraction via locally corrected nyström discretization," *IEEE Topical Meeting on Electrical Performance of Electronic Packaging*, pp. 107–110, Oct. 2006.

[31] K. Butt, I. Jeffrey, M. Al-Qedra, F. Ling, and V. Okhmatovski, "Accurate capacitance extraction in the entire package model using a parallel kernel independent hierarchical extractor," *Signal Propagation on Interconnects, 2007. SPI 2007. IEEE Workshop on*, pp. 149–152, May 2007.

[32] K. Butt, I. Jeffrey, F. Ling, and V. Okhmatovski, "Parallel discrete complex image method for Barnes-Hut accelerated capacitance extraction in

multilayered substrates," *IEEE Topical Meeting on Electrical Performance of Electronic Packaging*, pp. 333–336, Oct. 2007.

[33] I. Jeffrey and V. Okhmatovski, "Effect of multilayered substrate on the Barnes-Hut center-of-charge clustering approximation: Half-space case study," *Signal Propagation on Interconnects, 2008. SPI 2008. 12th IEEE Workshop on*, pp. 1–4, May 2008.

[34] W. C. Chew, *Waves and Fields in Inhomogenous Media*. Piscataway, NJ: IEEE Press, 1995.

[35] W. Chew, "A quick way to approximate a Sommerfeld-Weyl-type integral [antenna far-field radiation]," *Antennas and Propagation, IEEE Transactions on*, vol. 36, no. 11, pp. 1654–1657, Nov 1988.

[36] [Online]. Available: http://www.ansoft.com/products/si/q3d_extractor

Chapter 4

Applying Tree Based Algorithms to Full-Wave Modeling

In the previous chapter, we extended the Barnes-Hut (BH) algorithm to handling of electrostatic interactions in stratified media. In Chapter 5, we will show that the BH algorithm can be also applied to full-wave electromagnetic modeling. In this chapter, we introduce full-wave modeling and outline the requirements that must be satisfied by an acceleration technique such as the BH algorithm.

4.1 Electric Field Integral Equation

Consider an arbitrarily shaped object that is a perfect electric conductor (PEC) and occupies volume V and with a surface S. Let $\mathbf{E}^{inc}(\mathbf{r})$ represent an incident electric field due to external sources that impinges on the object. The incident field will induce a surface current $\mathbf{J}(\mathbf{r})$ on the object, which in turn produces a scattered electric field $\mathbf{E}^{scat}(\mathbf{r})$. Since the object is a PEC,

the total electric field satisfy

$$\mathbf{E}^{scat}(\mathbf{r}) + \mathbf{E}^{inc}(\mathbf{r}) = 0, \quad \mathbf{r} \in V \tag{4.1}$$

and the boundary condition

$$\hat{\mathbf{t}} \cdot \mathbf{E}^{scat}(\mathbf{r}) + \hat{\mathbf{t}} \cdot \mathbf{E}^{inc}(\mathbf{r}) = 0, \quad \mathbf{r} \in S \tag{4.2}$$

where $\mathbf{r}$ is the observation point and $\hat{\mathbf{t}}$ is a unit vector that is tangential to the surface. The scattered field can be expressed as

$$\mathbf{E}^{scat}(\mathbf{r}) = i\omega\mu \int_S \bar{\mathbf{G}}_{e0}(\mathbf{r}, \mathbf{r}') \cdot \mathbf{J}(\mathbf{r}') dS' \tag{4.3}$$

where

$$\bar{\mathbf{G}}_{e0}(\mathbf{r}, \mathbf{r}') = \left(\bar{\mathbf{I}} + \frac{\nabla\nabla\cdot}{k^2} \right) \mathrm{G}_0(\mathbf{r}, \mathbf{r}') \tag{4.4}$$

is the electric-type dyadic Green's function and

$$\mathrm{G}_0(\mathbf{r}, \mathbf{r}') = \frac{e^{-ik|\mathbf{r}-\mathbf{r}'|}}{4\pi|\mathbf{r}-\mathbf{r}'|} \tag{4.5}$$

is the Green's function for the scalar Helmholtz equations in 3D. In (4.3), the physical meaning of $\bar{\mathbf{G}}_{e0}(\mathbf{r}, \mathbf{r}') \cdot \mathbf{J}(\mathbf{r}')$ is the electrical field at $\mathbf{r}$ due to a point current source $\mathbf{J}(\mathbf{r}')$ located at $\mathbf{r}'$. By integrating over S, we obtain the total scattered field due to the induced surface currents on the object. Substituting (4.3) into (4.2) yields the Electric Field Integral Equation (EFIE),

$$\hat{\mathbf{t}} \cdot \int_S \bar{\mathbf{G}}_{e0}(\mathbf{r}, \mathbf{r}') \cdot \mathbf{J}(\mathbf{r}') d\mathbf{r}' = \frac{i}{\omega\mu} \hat{\mathbf{t}} \cdot \mathbf{E}^{inc}(\mathbf{r}) \tag{4.6}$$

which can be solved for the unknown surface current distribution $\mathbf{J}(\mathbf{r}')$, $\mathbf{r}' \in S$.

4.2 Method of Moments

The Method of Moments (MoM) is a numerical method for solving integral and differential equations by projecting of the unknown function to a space of

known basis functions and projecting the equation to a set of test functions. This procedure casts the integral (or differential) equation into a set of linear algebraic equations with respect to expansion coefficients of the unknown function. In order to apply MoM to EFIE, the unknown current is projected to a set of basis functions as

$$\mathbf{J}(\mathbf{r}) = \sum_{n=1}^{N} a_n \mathbf{b}_n(\mathbf{r}) \tag{4.7}$$

where $\{a_n\}$ are the expansion coefficients and $\{b_n(\mathbf{r})\}$ are the basis functions. Substituting this expression into (4.6) yields

$$\sum_{n=1}^{N} a_n \int_S \hat{\mathbf{t}} \cdot \bar{\mathbf{G}}_{e0}(\mathbf{r}, \mathbf{r}') \cdot \mathbf{b}_n(\mathbf{r}') dS' = \frac{i}{\omega\mu} \hat{\mathbf{t}} \cdot \mathbf{E}^{inc}(\mathbf{r}) \tag{4.8}$$

To eliminate the dependency on $\mathbf{r}$ and to formulate a system of equations, the above relationship is *tested* with the source basis[1] by

$$\sum_{n=1}^{N} a_n \int_S dS \mathbf{b}_m(\mathbf{r}) \cdot \int_S \bar{\mathbf{G}}_{e0}(\mathbf{r}, \mathbf{r}') \cdot \mathbf{b}_n(\mathbf{r}') dS' = \frac{i}{\omega\mu} \int_S \mathbf{b}_m(\mathbf{r}) \cdot \mathbf{E}^{inc}(\mathbf{r}) dS \qquad m = 1, \ldots, N \tag{4.9}$$

We rewrite the above relationship as a concise set of linear equations

$$\sum_{n=1}^{N} Z_{mn} a_n = v_m, \quad m = 1, \ldots, N \tag{4.10}$$

where

$$Z_{mn} = \int_S dS \mathbf{b}_m(\mathbf{r}) \cdot \int_S \bar{\mathbf{G}}_{e0}(\mathbf{r}, \mathbf{r}') \cdot \mathbf{b}_n(\mathbf{r}') dS' \tag{4.11}$$

is the (m, n)'s element in the corresponding matrix and

$$v_m = \int_S \mathbf{b}_m(\mathbf{r}) \cdot \mathbf{E}^{inc}(\mathbf{r}) d\mathbf{r} \tag{4.12}$$

is the m's element of the right hand side vector.

[1] The strategy of choosing the same basis for both the source and testing functions is often referred to as Galerkin's method. MoM imposes no constraints on the testing functions, but employing Galerkin's method is generally an efficient choice.

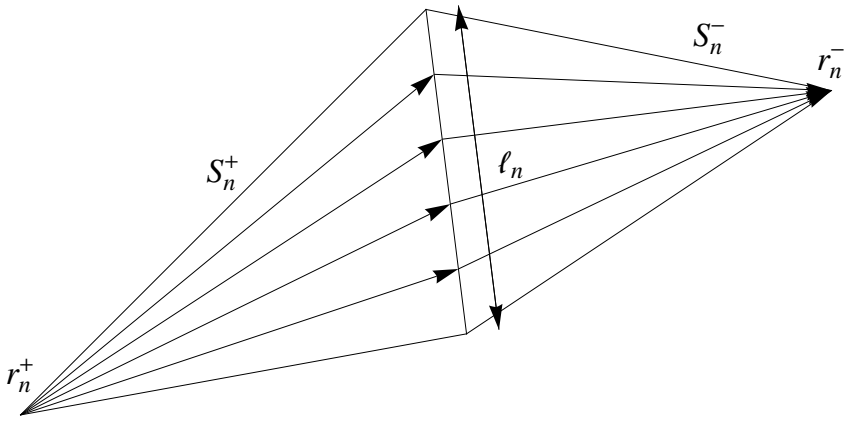

Figure 4.1: RWG basis function defined on a pair of triangles.

4.3 Basis Functions

A popular choice of basis functions in (4.7) is the Rao-Wilton-Glisson (RWG) basis [RWG82]. Each basis function is associated with a pair of triangles that share a common edge as shown in Figure 4.1 for the case of planar triangular elements. The basis functions are defined as follows:

$$\mathbf{b}_n(\mathbf{r}) = \begin{cases} \frac{\ell_n}{2A_n^+}(\mathbf{r} - \mathbf{r}_n^+), & \mathbf{r} \in S_n^+ \\ \frac{\ell_n}{2A_n^-}(\mathbf{r}_n^- - \mathbf{r}), & \mathbf{r} \in S_n^- \\ 0, & \text{otherwise} \end{cases} \tag{4.13}$$

where ℓ_n is the length of the common edge and $A_n^\pm$ are the areas of the triangles $S_n^\pm$. According to the definition of the RWG basis function the current flows continuously from triangle S_n^+ into triangle S_n^-. The continuity of the current is consistent with the physical behavior of current flow on conducting surfaces. This greatly improves the accuracy of current solution with RWG-MoM compared to alternative choices of basis functions. The surface charge density on the pair of triangles is given by the divergence of basis function,

which has the following form

$$\nabla \cdot \mathbf{b}_n(\mathbf{r}) = \begin{cases} \frac{\ell_n}{A_n^+}, & \mathbf{r} \in S_n^+ \\ -\frac{\ell_n}{A_n^-}, & \mathbf{r} \in S_n^- \\ 0, & \text{otherwise} \end{cases} \tag{4.14}$$

By applying the RWG basis to (4.11), we can limit the integration range to the triangle pair S_m and S_n and simplify as

$$Z_{mn} = \int_{S_m} dS \mathbf{b}_m(\mathbf{r}) \cdot \int_{S_n} \bar{\mathbf{G}}_{e0}(\mathbf{r}, \mathbf{r}') \cdot \mathbf{b}_n(\mathbf{r}') dS' \tag{4.15}$$

The above expression for Z_{mn} shows that the complexity of computing Z_{mn} depends on the separation distance between S_m and S_n. If S_m and S_n are overlapping or adjacent, then it is necessary to perform an analytical singularity extraction due to the singular behavior of the Green's function. On the other hand, the Green's function is smooth if S_m and S_n are *well-separated* and the integrals in (4.15) can be computed with a numerical quadrature rule.

4.4 Acceleration of MoM

Several techniques are available for solving the matrix equation resulting from (4.10) and the most general technique is to perform direct inversion of the system matrix. The computational cost for inverting a dense matrix grows as $O(N^3)$ and requires $O(N^2)$ memory. A more common technique is to use an iterative method that iteratively solves the equation by performing matrix-vector products until the solution satisfies a convergence condition. The cost of each matrix-vector product is $O(N^2)$ and by ensuring that the system is well-conditioned, the number of iterations is often much smaller than N. An iterative matrix solver does not use the system matrix explicitly and we can therefore employ matrix-free methods to accelerate the matrix-vector product. In order to show how we can apply tree based algorithms to perform the matrix-vector product, we partition the space of basis functions into *near* and

far regions so that all interactions in the far region are well-separated. Let I_m^{near} denote a set of indices such that $\{Z_{mn} : n \in I_m^{\text{near}}\}$ are the matrix elements in the m's row that are in the near region. Denote the remaining indices as I_m^{far} and rewrite (4.10) as

$$\sum_{n \in I_m^{\text{near}}} Z_{mn} a_n + \sum_{n \in I_m^{\text{far}}} Z_{mn} a_n = v_m, \quad m = 1, \ldots, N \tag{4.16}$$

Let Z_{mn}^{far} denote an accurate approximation of Z_{mn} in the far region that is obtain by numerical integration as

$$Z_{mn}^{\text{far}} = \sum_{k}^{M_m} w_{m,k} \mathbf{b}_m(\mathbf{r}_{m,k}) \cdot \sum_{j}^{M_n} w_{n,j} \bar{\mathbf{G}}_{e0}(\mathbf{r}_{m,k}, \mathbf{r}_{n,j}) \cdot \mathbf{b}_n(\mathbf{r}_{n,j}) \tag{4.17}$$

where M_i denotes the number of quadrature points on S_i and $\{\mathbf{r}_{i,k} \in S_i : k = 1, \ldots, M_i\}$ and $\{w_{i,k}\}$ are corresponding locations and weights of the quadrature points, respectively. We can now approximate (4.16) as

$$\sum_{n \in I_m^{\text{near}}} Z_{mn} a_n + \sum_{n \in I_m^{\text{far}}} Z_{mn}^{\text{far}} a_n = v_m, \quad m = 1, \ldots, N \tag{4.18}$$

We have effectively partitioned the system matrix into two matrices, $\bar{\mathbf{Z}}^{near}$ and $\bar{\mathbf{Z}}^{far}$. The number of elements in $\bar{\mathbf{Z}}^{near}$ is, in general, of order $O(N)$ and therefore, it is sufficient to accelerate the matrix-vector product $\bar{\mathbf{Z}}^{far}\mathbf{a}$. The matrix-vector product $\bar{\mathbf{Z}}^{far}\mathbf{a}$ can viewed as an N-body problem where we seek to compute the mutual interactions between all quadrature points while excluding those in the near region. Hence, we can apply a tree-based algorithm, such as BH or FMM, to compute $\bar{\mathbf{Z}}^{far}\mathbf{a}$ provided that the algorithm can approximate the pertinent Green's function kernel. The formulation in (4.17) utilizes the electric-type dyadic Green's function $\bar{\mathbf{G}}_{e0}$. In Chapter 7, we will present a version of FMM that can accelerate the $\bar{\mathbf{G}}_{e0}$ kernel directly. However, the extension to the BH algorithm that we will present in the next chapter is designed to accelerate the scalar Helmholtz kernel, G_0. Therefore, we will continue by showing that we can write EFIE in a mixed potential form where the matrix elements are defined in terms of the scalar G_0 kernel instead of the dyadic kernel $\bar{\mathbf{G}}_{e0}$ utilized thus far.

4.5 A Mixed Potential Form of EFIE

Substituting (4.4) into (4.11) yields

$$\begin{aligned} Z_{mn} &= \int_{S_m} d\mathbf{r}\mathbf{b}_m(\mathbf{r}) \cdot \int_{S_n} \left(\bar{\mathbf{I}} + \frac{\nabla\nabla}{k^2} \right) \mathrm{G}_0(\mathbf{r}, \mathbf{r}') \cdot \mathbf{b}_n(\mathbf{r}') d\mathbf{r}' \\ &= \int_{S_m} d\mathbf{r}\mathbf{b}_m(\mathbf{r}) \cdot \int_{S_n} \mathrm{G}_0(\mathbf{r}, \mathbf{r}')\mathbf{b}_n(\mathbf{r}') d\mathbf{r}' \\ &+ \int_{S_m} d\mathbf{r}\mathbf{b}_m(\mathbf{r}) \cdot \int_{S_n} \frac{\nabla\nabla}{k^2} \mathrm{G}_0(\mathbf{r}, \mathbf{r}') \cdot \mathbf{b}_n(\mathbf{r}') d\mathbf{r}' \end{aligned} \tag{4.19}$$

By applying the divergence theorem to the integrals over areas S_m and S_n and taking into consideration the fact that the RWG basis does not have current flow normal to its boundary as well as the property $\nabla \mathrm{G}_0(\mathbf{r}, \mathbf{r}') = -\nabla' \mathrm{G}_0(\mathbf{r}, \mathbf{r}')$, we can shift the gradient operator to the testing basis and the divergence operator to the source basis as

$$\begin{aligned} Z_{mn} &= \int_{S_m} d\mathbf{r}\mathbf{b}_m(\mathbf{r}) \cdot \int_{S_n} \mathrm{G}_0(\mathbf{r}, \mathbf{r}')\mathbf{b}_n(\mathbf{r}') d\mathbf{r}' \\ &+ \frac{1}{k^2} \int_{S_m} d\mathbf{r} \nabla \cdot \mathbf{b}_m(\mathbf{r}) \int_{S_n} \mathrm{G}_0(\mathbf{r}, \mathbf{r}') \nabla' \cdot \mathbf{b}_n(\mathbf{r}') d\mathbf{r}' \end{aligned} \tag{4.20}$$

The expression for Z_{mn} has been split into a vector potential term that is discretized by RWG basis functions and a surface charge density term discretized by *pulse* basis functions defined in (4.14). The above expression for the RWG MoM matrix elements is in the mixed potential form in which the first term corresponds to discretization of the magnetic vector potential and the second term to the discretization of the electric scalar potential. Equation (4.17) is a reformulation of (4.15) where the $\bar{\mathbf{G}}_{e0}$ kernel as been replaced with G_0 kernels, which greatly simplifies the numerical evaluation of the matrix elements.

4.6 An N-Body Formulation of the MoM Discretized Mixed Potential Form of EFIE

An expression for the elements in the mixed potential form of $\bar{\mathbf{Z}}^{far}$ is obtained by combining equations (4.17) and (4.20) into

$$\begin{aligned} Z_{mn}^{\text{far}} = & \sum_{k}^{M_m} w_{m,k}\mathbf{b}_m(\mathbf{r}_{m,k}) \cdot \sum_{j}^{M_n} w_{n,j}\mathrm{G}_0(\mathbf{r}_{m,k},\mathbf{r}_{n,j})\mathbf{b}_n(\mathbf{r}_{n,j}) \\ & + \frac{1}{k^2}\sum_{k}^{M_m} w_{m,k}\nabla\cdot\mathbf{b}_m(\mathbf{r}_{m,k}) \sum_{j}^{M_n} w_{n,j}\mathrm{G}_0(\mathbf{r}_{m,k},\mathbf{r}_{n,j})\nabla'\cdot\mathbf{b}_n(\mathbf{r}_{n,j}) \end{aligned} \tag{4.21}$$

We can now apply this result to formulate the $\bar{\mathbf{Z}}^{far}\cdot\mathbf{a}$ matrix vector product as an N-body problem with bodies located at quadrature points $\{\mathbf{r}_{i,k}\in S_i : k=1,\ldots,M_i, i=1,\ldots,N\}$. The procedure for evaluating the accelerated matrix-vector product is provided below.

1. Evaluate $\bar{\mathbf{Z}}^{near}\cdot\mathbf{a}$ and add the result to the solution vector.

2. Invoke the N-body solver for 4 sets of magnitudes $\{Q\}$ according to:

   - Solve for magnitudes $Q_{n,j}^{x} = w_{n,j}a_n\left(\mathbf{b}_n(\mathbf{r}_{n,j})\right)_x$ in order to obtain $A_{m,k}^{x} = \sum_n^N\sum_j^{M_n} Q_{n,j}^{x}\mathrm{G}_0(\mathbf{r}_{m,k},\mathbf{r}_{n,j})$.
   - Solve for magnitudes $Q_{n,j}^{y} = w_{n,j}a_n\left(\mathbf{b}_n(\mathbf{r}_{n,j})\right)_y$ in order to obtain $A_{m,k}^{y} = \sum_n^N\sum_j^{M_n} Q_{n,j}^{y}\mathrm{G}_0(\mathbf{r}_{m,k},\mathbf{r}_{n,j})$.
   - Solve for magnitudes $Q_{n,j}^{z} = w_{n,j}a_n\left(\mathbf{b}_n(\mathbf{r}_{n,j})\right)_z$ in order to obtain $A_{m,k}^{z} = \sum_n^N\sum_j^{M_n} Q_{n,j}^{z}\mathrm{G}_0(\mathbf{r}_{m,k},\mathbf{r}_{n,j})$.
   - Solve for magnitudes $Q_{n,j}^{\phi} = w_{n,j}a_n\nabla'\cdot\mathbf{b}_n(\mathbf{r}_{n,j})$ in order to obtain $\phi_{m,k} = \sum_n^N\sum_j^{M_n} Q_{n,j}^{\phi}\mathrm{G}_0(\mathbf{r}_{m,k},\mathbf{r}_{n,j})$.

3. Use the relationship

$$\sum_{n\in I_m^{\text{far}}} Z_{mn}a_n = \sum_{n=1}^{N} Z_{mn}^{far}a_n = \sum_{k}^{M_m} w_{m,k}\mathbf{b}_m(\mathbf{r}_{m,k})\cdot\mathbf{A}_{m,k} + \frac{1}{k^2}\sum_{k}^{M_m} w_{m,k}\phi_{m,k}\nabla\cdot\mathbf{b}_m(\mathbf{r}_{m,k}) \tag{4.22}$$

   for $m = 1,\ldots,N$ to evaluate $\bar{\mathbf{Z}}^{far}\cdot\mathbf{a}$ and add the result to the solution vector.

The above procedure decomposes the $\bar{\mathbf{Z}}\cdot\mathbf{a}$ matrix-vector product into four evaluations with an N-body solver governed by the scalar G_0 kernel. In the next chapter, we present an extension to the Barnes-Hut algorithm that is suitable for accelerating the solution of the mixed-potential form of EFIE according to the above procedure.

Chapter 5

Generalization of the Barnes-Hut Algorithm for the Helmholtz Equation in Three Dimensions

The Barnes-Hut algorithm originally developed for $O(N \log N)$ solution of N-body problem with the Laplace kernel is generalized to the case of the scalar Helmholtz kernel in three dimensions. Analogous to the center-of-charge concept used in the static algorithm, a center-of-radiation is associated with each box of the hierarchically partitioned space enclosing the sources of interest. The algorithm is applicable to the acceleration of electromagnetic interactions between sources confined to electrically small volumes. The method may be used in conjunction with the high-frequency Fast Multipole Method to eliminate its low-frequency breakdown.

5.1 Introduction

Today's wireless systems tightly integrate the antenna's radiating elements, feeding networks, and RF circuitry. Electromagnetic simulations used to validate system designs present various challenges. The most formidable of these challenges is the large size of the pertinent discrete models and multi-scale features of the designs. Among the limited computational techniques capable of conducting such simulations is the boundary-element method-of-moments [1] accelerated with broadband fast algorithms which allow for simultaneous $O(N \log N)$ evaluation of full-wave and quasi-static interactions [2].

In this paper we propose a simple alternative to the low-frequency Fast Multipole Method (FMM) [2], applicable when two digits of precision in the evaluation of the pertinent matrix-vector product is sufficient for a given discretization scheme [1]. The proposed method is based on a generalization of the Barnes-Hut (BH) algorithm [3] for rapid evaluation of electromagnetic interactions from a large group of sources enclosed in an electrically small volume. Similar to the static BH algorithm that introduces centers-of-charge in association with each box of a hierarchically partitioned volume

enclosing all static sources, the proposed full-wave version of the method introduces centers-of-radiation (CoR) in association with each box containing time-harmonic sources. The position and magnitude of the center-of-radiation in each box is determined by matching the zeroth and first order spectral moments of the true field produced by sources contained in that box to the field of a single point source acting as the CoR in the vicinity the stationary phase point [4]. Since the stationary phase point in k-space is a function of observation angle, so is the CoR. The CoR sources are shown to allow for recursive clustering necessary for the development of an $O(N \log N)$ solution of the time-harmonic N-body problem. The numerical results presented in this paper validate the method and demonstrate its error behavior in comparison with low- and high-frequency FMM [2].

5.2 Center-of-Radiation Field Approximation

Consider N time-harmonic point sources with associated phasors $q_1, q_2, ..., q_N$ varying with frequency ω and located in homogeneous space at $\boldsymbol{r'_1}, \boldsymbol{r'_2}, ..., \boldsymbol{r'_N}$. The field produced by the sources satisfies the Helmholtz equation [4]

$$\nabla^2 \phi(\boldsymbol{r}) + k_0^2 \phi(\boldsymbol{r}) = -\sum_{i=1}^{N} q_i \delta(\boldsymbol{r} - \boldsymbol{r'_i}), \quad i = 1, ..., N, \tag{5.1}$$

where k_0 is the homogeneous space wavenumber, and $\boldsymbol{r} = x\hat{\boldsymbol{x}} + y\hat{\boldsymbol{y}} + z\hat{\boldsymbol{z}}$ is the spatial position vector. The spatial solution of (5.1)

$$\phi(\boldsymbol{r}) = \sum_{i=1}^{N} \phi_i(\boldsymbol{r}) = \sum_{i=1}^{N} \frac{q_i \exp\left(-jk_0|\boldsymbol{r} - \boldsymbol{r'_i}|\right)}{4\pi|\boldsymbol{r} - \boldsymbol{r'_i}|}, \tag{5.2}$$

corresponds to the spectral solution

$$\hat{\phi}(\boldsymbol{k}) = \sum_{i=1}^{N} \hat{\phi}_i(\boldsymbol{k}) = \sum_{i=1}^{N} \frac{q_i \exp\left(j\boldsymbol{k} \cdot \boldsymbol{r'_i}\right)}{k^2 - k_0^2}, \tag{5.3}$$

where $\boldsymbol{k} = k_x \hat{\boldsymbol{k}}_{\boldsymbol{x}} + k_y \hat{\boldsymbol{k}}_{\boldsymbol{y}} + k_z \hat{\boldsymbol{k}}_{\boldsymbol{z}}$ is the position vector in k-space, $\quad j = \sqrt{-1}$. With subsequent derivations in mind we extract the exponential part of the

spectrum

$$\hat{\Phi}(\boldsymbol{k}) = \sum_{i=1}^{N} \hat{\Phi}_i(\boldsymbol{k}) = \sum_{i=1}^{N} q_i \exp(j\boldsymbol{k} \cdot \boldsymbol{r_i'}). \tag{5.4}$$

The spatial and spectral solutions are related via the three-dimensional Fourier transform

$$\phi(\boldsymbol{r}) = \frac{1}{8\pi^3} \int \int_{-\infty}^{+\infty} \int \hat{\phi}(\boldsymbol{k}) e^{-j\boldsymbol{k}\cdot\boldsymbol{r}} dk_x dk_y dk_z. \tag{5.5}$$

The far field $\phi(\boldsymbol{r})$, $r \gg 1$, of the group of sources is determined by the spectrum in the vicinity of the spectral point $\boldsymbol{k_s} = k_0\hat{\boldsymbol{r}}$ known as the stationary phase point [4]. By introducing a single point source with associated phasor Q_Σ located at $\boldsymbol{r_\Sigma}$ which we refer to as the *center-of-radiation* we can match the true field $\phi(\boldsymbol{r})$ to the field of the center-of-radiation $\psi(\boldsymbol{r})$. This is accomplished by matching the spectrum of the CoR field

$$\hat{\psi}(\boldsymbol{k}) = \frac{Q_\Sigma \exp(j\boldsymbol{k} \cdot \boldsymbol{r_\Sigma})}{k^2 - k_0^2} = \frac{\Psi(\boldsymbol{k})}{k^2 - k_0^2}, \tag{5.6}$$

to the spectrum of the true field $\hat{\phi}(\boldsymbol{k})$ in the vicinity of the stationary phase point $\boldsymbol{k_s}$. The Taylor series expansion of the spectrum of a single point source $\Phi_i(\boldsymbol{k})$ in the vicinity of $\boldsymbol{k} = \boldsymbol{k_s}$ follows from (5.4) as

$$\Phi_i(\boldsymbol{k}) = \Phi_i(\boldsymbol{k_s}) \sum_{n=0}^{\infty} \frac{[j(\boldsymbol{k} - \boldsymbol{k_s}) \cdot \boldsymbol{r_i'}]^n}{n!}, \tag{5.7}$$

where matching the zeroth order term for the true field spectra Φ and CoR field spectra Ψ requires that

$$\Psi(\boldsymbol{k_s}) = \Phi(\boldsymbol{k_s}). \tag{5.8}$$

Matching of the first order terms in the Taylor expansion of the true field spectrum and the CoR field spectrum yields

$$[(\boldsymbol{k} - \boldsymbol{k_s}) \cdot \boldsymbol{r_\Sigma}]\Psi(\boldsymbol{k_s}) = \sum_{i=1}^{N} [(\boldsymbol{k} - \boldsymbol{k_s}) \cdot \boldsymbol{r_i'}]\Phi_i(\boldsymbol{k_s}). \tag{5.9}$$

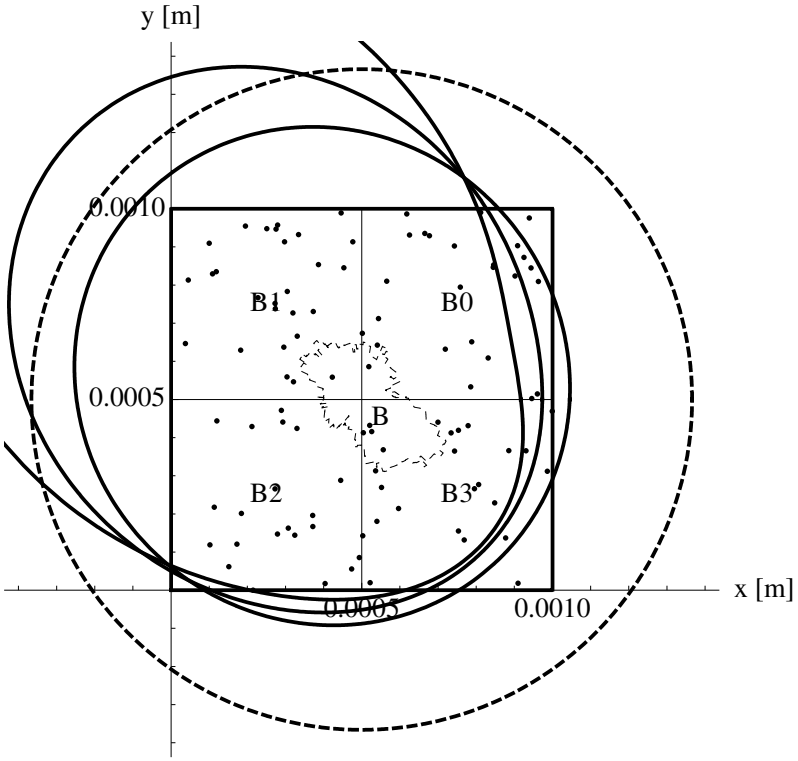

Figure 5.1: The solid lines shows the absolute distance between the center of a $1mm$ box to the CoR according to (5.10) and (5.11) as a function of observation angle φ with $\vartheta = \pi/2$ due to $N = 100$ random point sources for $k_0 = 500, 1000, 1500$. The dashed line shows the same distance when the CoRs are computed according to (5.12) for $k_0 = 1500$. The square represents the box boundaries in XY-plane and the dashed circle has a diameter of $\sqrt{3}mm$ to indicate when the CoR position falls outside the box. Point sources are projected onto XY-plane.

For arbitrary $\boldsymbol{k}$ (5.9) is satisfied when

$$\boldsymbol{r_\Sigma} = \frac{\sum_{i=1}^{N} \boldsymbol{r_i'} \Phi_i(\boldsymbol{k_s})}{\Psi(\boldsymbol{k_s})} = \frac{\sum_{i=1}^{N} \boldsymbol{r_i'} q_i \exp(j\boldsymbol{k_s} \cdot \boldsymbol{r_i'})}{\sum_{i=1}^{N} q_i \exp(j\boldsymbol{k_s} \cdot \boldsymbol{r_i'})}. \tag{5.10}$$

Having determined $\boldsymbol{r_\Sigma}$ we can solve (5.6) for Q_Σ as

$$Q_\Sigma = \frac{\Phi(\boldsymbol{k_s})}{\exp(j\boldsymbol{k_s} \cdot \boldsymbol{r_\Sigma})} = \sum_{i=1}^{N} q_i \exp(j\boldsymbol{k_s} \cdot (\boldsymbol{r_i'} - \boldsymbol{r_\Sigma})). \tag{5.11}$$

From (5.10) and (5.11) we notice that in the limit as k_0 approaches zero, the complex valued CoR reduces to the static center-of-charge. We also notice that the CoR depends on the observation direction $\hat{\boldsymbol{r}}$ since the stationary phase point changes as $\boldsymbol{k_s} = k_0\hat{\boldsymbol{r}}$. This is different from the static case where the stationary phase point $\boldsymbol{k_s} = \boldsymbol{0}$ coincides with the origin of the k-space for any observation direction $\hat{\boldsymbol{r}}$. The denominator in (5.10) may become sufficiently small so that the CoR $\boldsymbol{r_\Sigma}$ is not contained within the bounds of the box for certain directions as shown by the solid curve corresponding to $k_0 = 1500$ in Fig. 5.1. In order to ensure that the CoR is contained inside the box for each observation direction $\hat{\boldsymbol{r}}$ we introduce four CoRs by separating the N sources into four groups as $N = N_{++}(\boldsymbol{k_s}) + N_{+-}(\boldsymbol{k_s}) + N_{-+}(\boldsymbol{k_s}) + N_{+-}(\boldsymbol{k_s})$, where $N_{++}(\boldsymbol{k_s})$ is the number of sources that produce $\Phi_i(\boldsymbol{k_s})$ lying in the first quadrant of the complex plane, i.e. $\Re\Phi_i(\boldsymbol{k_s}) \geq 0$ and $\Im\Phi_i(\boldsymbol{k_s}) \geq 0$. Similarly, N_{-+}, N_{+-}, N_{--} are the number of sources producing Φ_i in the second, third, and fourth quadrants of the complex plane, respectively. If one introduces a distinct CoR for the group of sources producing Φ_i in the first quadrant as

$$\boldsymbol{r_{\Sigma,++}}(\boldsymbol{k_s}) = \frac{\sum_{i=1}^{N_{++}(\boldsymbol{k_s})} \boldsymbol{r_i'} \Phi_{i,++}(\boldsymbol{k_s})}{\sum_{i=1}^{N_{++}(\boldsymbol{k_s})} \Phi_{i,++}(\boldsymbol{k_s})}, \tag{5.12}$$

it can be shown that the CoR is guaranteed to be situated within the bounds of the box containing the sources, that is $|\Re x_{\Sigma,++}| < B/2$, $|\Im x_{\Sigma,++}| < B/2$, $|\Re y_{\Sigma,++}| < B/2$, $|\Im y_{\Sigma,++}| < B/2$, and $|\Re z_{\Sigma,++}| < B/2$, $|\Im z_{\Sigma,++}| < B/2$, B being the size of the box. Thus, the field $\phi(\boldsymbol{r})$ of N sources (5.2) is approximated

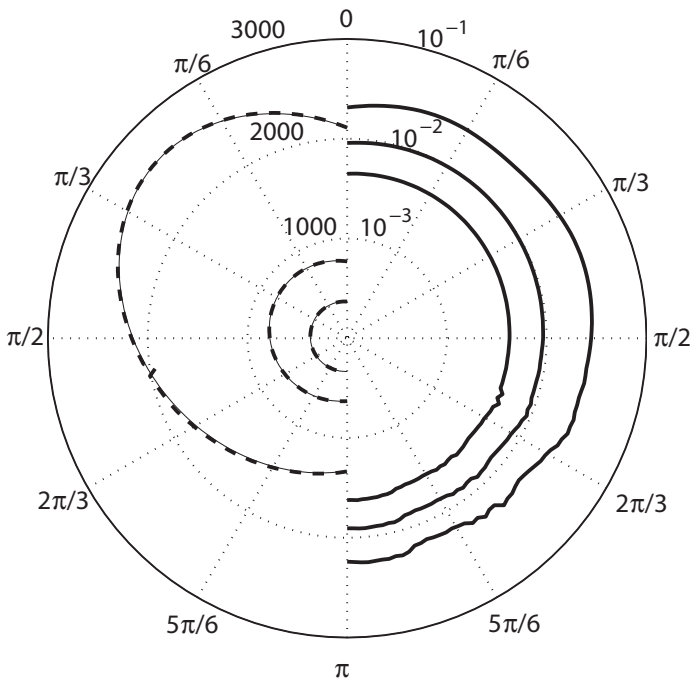

Figure 5.2: The left side shows $|\phi(\boldsymbol{r})|$ as function of observation angle φ with $\vartheta = \pi/2$ for the distribution of $N = 100$ random sources contained in a cube of size $B = 1mm$ at observation distances, $|\boldsymbol{r}|$, of $2mm$, $5mm$, and $10mm$ for $k_0 = 500$.

with four CoRs as

$$\begin{aligned}\tilde{\psi}(\boldsymbol{r}) = &\frac{Q_{\Sigma,++}(k_0\hat{\boldsymbol{r}})e^{-jk_0|\boldsymbol{r}-\boldsymbol{r}_{\boldsymbol{\Sigma},++}(k_0\hat{\boldsymbol{r}})|}}{4\pi|\boldsymbol{r}-\boldsymbol{r}_{\boldsymbol{\Sigma},++}(k_0\hat{\boldsymbol{r}})|}+\\ &\frac{Q_{\Sigma,+-}(k_0\hat{\boldsymbol{r}})e^{-jk_0|\boldsymbol{r}-\boldsymbol{r}_{\boldsymbol{\Sigma},+-}(k_0\hat{\boldsymbol{r}})|}}{4\pi|\boldsymbol{r}-\boldsymbol{r}_{\boldsymbol{\Sigma},+-}(k_0\hat{\boldsymbol{r}})|}+\\ &\frac{Q_{\Sigma,-+}(k_0\hat{\boldsymbol{r}})e^{-jk_0|\boldsymbol{r}-\boldsymbol{r}_{\boldsymbol{\Sigma},-+}(k_0\hat{\boldsymbol{r}})|}}{4\pi|\boldsymbol{r}-\boldsymbol{r}_{\boldsymbol{\Sigma},-+}(k_0\hat{\boldsymbol{r}})|}+\\ &\frac{Q_{\Sigma,--}(k_0\hat{\boldsymbol{r}})e^{-jk_0|\boldsymbol{r}-\boldsymbol{r}_{\boldsymbol{\Sigma},--}(k_0\hat{\boldsymbol{r}})|}}{4\pi|\boldsymbol{r}-\boldsymbol{r}_{\boldsymbol{\Sigma},--}(k_0\hat{\boldsymbol{r}})|}.\end{aligned} \tag{5.13}$$

The dashed curve in the interior of the box in Fig. 5.1 depicts the magnitude of CoR $|\boldsymbol{r}_{\boldsymbol{\Sigma},++}(k_0\hat{\boldsymbol{r}})|$ at $k_0B = 1.5$ for observation directions $\hat{\boldsymbol{r}}$ in XY-

Algorithm 1 Compute CoRs of a set of sources

Inputs: Set of sources $(\boldsymbol{r'_i}, q_i)$, $i = 1, \ldots, N$ and observation direction $\hat{\boldsymbol{r}}$

Output: CoRs $(\boldsymbol{r_{\Sigma,c}}, q_{\Sigma,c})$, $c = ++, -+, +-, --$, for the set of sources

1: $\boldsymbol{k_s} \leftarrow k_0\ \hat{\boldsymbol{r}}$
2: **for** each quadrant $c = ++, -+, +-, --$ **do**
3: $\quad \boldsymbol{r_{\Sigma,c}} \leftarrow \boldsymbol{0}$
4: $\quad q_{\Sigma,c} \leftarrow 0$
5: $\quad tmp1 \leftarrow 0$ $\{tmp1$ is a temporary variable$\}$
6: $\quad tmp2 \leftarrow 0$ $\{tmp2$ is a temporary variable$\}$
7: $\quad$ **for** each point source $i = 1, \ldots, N$ **do**
8: $\quad\quad \Phi \leftarrow q_i \exp(j\boldsymbol{k_s}\cdot\boldsymbol{r'_i})$
9: $\quad\quad$ **if** Φ is in quadrant c **then**
10: $\quad\quad\quad tmp1 \leftarrow tmp1 + \Phi\boldsymbol{r'_i}$; $tmp2 \leftarrow tmp2 + \Phi$
11: $\quad\quad$ **end if**
12: $\quad$ **end for**
13: $\quad \boldsymbol{r_{\Sigma,c}} \leftarrow tmp1/tmp2$
14: $\quad q_{\Sigma,c} \leftarrow tmp2/\exp(j\boldsymbol{k_s}\cdot\boldsymbol{r_{\Sigma,c}})$
15: **end for**

plane, i.e. $\hat{\boldsymbol{r}} = \cos\varphi\hat{\boldsymbol{x}} + \sin\varphi\hat{\boldsymbol{y}}$, $\varphi \in [0, 2\pi]$. One can see that for all the observation directions the CoR $\boldsymbol{r}_{\boldsymbol{\Sigma},++}$ introduced according to (5.12) stays within the bounds of the box. The left side of Fig. 5.2 shows the true field $\phi(\boldsymbol{r})$ in (5.2) and its CoR approximation $\tilde{\psi}(\boldsymbol{r})$ given by (5.13) while the right hand side of the plot shows their relative error

$$\epsilon(\boldsymbol{r}) = |\phi(\boldsymbol{r}) - \tilde{\psi}(\boldsymbol{r})|/|\phi(\boldsymbol{r})|. \tag{5.14}$$

for various ratios of box size B to the observation distance r.

5.3 Hierarchical Clustering of Sources

In order to incorporate the CoR into a BH type algorithm it is essential that the CoR approximation can be applied recursively. Let us demonstrate that this is indeed the case with both the CoR approximations (5.11) and (5.12). For that purpose let us consider the original box containing the sources as the parent box (center of the parent box is denoted with 'B' in Fig. 5.1) and denote the 8 equally sized cubes sub-dividing the parent box as the child boxes (centers of the first four child boxes are denoted as 'B0', 'B1', 'B2', 'B3' in Fig. 5.1). From (5.10) the CoR of the parent box can be rewritten as

$$\boldsymbol{r}_{\boldsymbol{\Sigma}}^{\boldsymbol{B}}(\boldsymbol{k}_{\boldsymbol{s}}) = \frac{\sum_{i=1}^{N^B} \boldsymbol{p}_i^B \Phi_i^B(\boldsymbol{k}_{\boldsymbol{s}})}{\sum_{i=1}^{N^B} \Phi_i^B(\boldsymbol{k}_{\boldsymbol{s}})} = \frac{\sum_{i=1}^{N^B} \boldsymbol{p}_i^B q_i^B \exp(j\boldsymbol{k}_{\boldsymbol{s}} \cdot \boldsymbol{p}_i^B)}{\sum_{i=1}^{N^B} q_i^B \exp(j\boldsymbol{k}_{\boldsymbol{s}} \cdot \boldsymbol{p}_i^B)}, \tag{5.15}$$

where $\boldsymbol{p}_i^B$ are locations of N^B sources contained in the parent box with respect to the system of coordinates having the origin at the parent box center. Splitting the sums in the numerator and denominator of (5.15) over child boxes and representing the position vectors $\boldsymbol{p}_i^B$ in the systems of coordinates with the origins at the child box centers we can rewrite (5.15) as

$$\boldsymbol{r}_{\boldsymbol{\Sigma}}^{\boldsymbol{B}}(\boldsymbol{k}_{\boldsymbol{s}}) = \frac{\sum_{b=1}^{8} \sum_{i=1}^{N^{Bb}} (\boldsymbol{p}_i^{Bb} + \boldsymbol{d}^{Bb}) q_i^{Bb} \exp(j\boldsymbol{k}_{\boldsymbol{s}} \cdot (\boldsymbol{p}_i^{Bb} + \boldsymbol{d}^{Bb}))}{\sum_{b=1}^{8} \sum_{i=1}^{N^{Bb}} q_i^{Bb} \exp(j\boldsymbol{k}_{\boldsymbol{s}} \cdot (\boldsymbol{p}_i^{Bb} + \boldsymbol{d}^{Bb}))}, \tag{5.16}$$

Algorithm 2 Compute CoRs for all each node in the BH tree

Input: Tree node n

Description: This algorithm computes the CoR locations and magnitudes of all the nodes in the tree rooted at n. The algorithm is called from the main program with the root node of the BH tree as the input.

1: **for** each observation direction $\hat{\boldsymbol{r}}_{\boldsymbol{d}}$, $d = 1, \ldots, M$ **do**
2: **if** n contains 1 source **then**
3: Compute the CoRs due to the source for $\hat{\boldsymbol{r}}_{\boldsymbol{d}}$ using Algorithm 3 and store the result at n
4: **else**
5: Q.**clear**() {Empty the content in queue}
6: **for** each child c_i of n, $i = 1, \ldots, 8$ **do**
7: **if** c_i is not empty **then**
8: Recursively call this algorithm on c_i
9: Q.**push**($c_i.CoRs$) {push c_i's CoRs into queue}
10: **end if**
11: **end for**
12: Compute the CoRs due to all the aggregated sources in Q for $\hat{\boldsymbol{r}}_{\boldsymbol{d}}$ using Algorithm 3 and store the result at n
13: **end if**
14: **end for**

where $\boldsymbol{p}_i^{Bb}$ is the location of i-th source contained in b-th child box with respect to the system of coordinates having the origin at this child box center and $\boldsymbol{d}^{Bb}$ is the vector from the parent box center to the b-th child box center. With the definition of the b-th child box's CoR

$$Q_{\Sigma}^{Bb}(\boldsymbol{k_s}) \exp\left(j\boldsymbol{k_s} \cdot \boldsymbol{r_{\Sigma}^{Bb}}\right) = \sum_{i=1}^{N^{Bb}} \Phi_i^{Bb}(\boldsymbol{k_s}), \tag{5.17}$$

$$\boldsymbol{r_{\Sigma}^{Bb}}(\boldsymbol{k_s}) = \frac{\sum_{i=1}^{N^{Bb}} \boldsymbol{p}_i^{Bb} \Phi_i^{Bb}(\boldsymbol{k_s})}{\sum_{i=1}^{N^{Bb}} \Phi_i^{Bb}(\boldsymbol{k_s})} = \frac{\sum_{i=1}^{N^{Bb}} \boldsymbol{p}_i^{Bb} q_i^{Bb} \exp\left(j\boldsymbol{k_s} \cdot \boldsymbol{p}_i^{Bb}\right)}{\sum_{i=1}^{N^{Bb}} q_i^{Bb} \exp\left(j\boldsymbol{k_s} \cdot \boldsymbol{p}_i^{Bb}\right)}, \tag{5.18}$$

the expression for the parent box CoR simplifies to

$$\boldsymbol{r_{\Sigma}^{B}}(\boldsymbol{k_s}) = \frac{\sum_{b=1}^{8} (\boldsymbol{r_{\Sigma}^{Bb}}(\boldsymbol{k_s}) + \boldsymbol{d}^{Bb}) e^{j\boldsymbol{k_s} \cdot (\boldsymbol{r_{\Sigma}^{Bb}}(\boldsymbol{k_s}) + \boldsymbol{d}^{Bb})} Q^{Bb}(\boldsymbol{k_s})}{\sum_{b=1}^{8} e^{j\boldsymbol{k_s} \cdot (\boldsymbol{r_{\Sigma}^{Bb}}(\boldsymbol{k_s}) + \boldsymbol{d}^{Bb})} Q^{Bb}(\boldsymbol{k_s})}. \tag{5.19}$$

Noticing that $\boldsymbol{r_{\Sigma}^{Bb}}(\boldsymbol{k_s}) + \boldsymbol{d}^{Bb}$ in (5.19) is nothing but the b-th box's CoR location in the parent box's coordinate system and denoting it as $\boldsymbol{r_{\Sigma}^{b}}(\boldsymbol{k_s})$ we obtain the expression for the parent box's CoR in terms of children's CoRs

$$\boldsymbol{r_{\Sigma}^{B}}(\boldsymbol{k_s}) = \frac{\sum_{b=1}^{8} \boldsymbol{r_{\Sigma}^{b}}(\boldsymbol{k_s}) e^{j\boldsymbol{k_s} \cdot \boldsymbol{r_{\Sigma}^{b}}(\boldsymbol{k_s})} Q^{Bb}(\boldsymbol{k_s})}{\sum_{b=1}^{8} e^{j\boldsymbol{k_s} \cdot \boldsymbol{r_{\Sigma}^{b}}(\boldsymbol{k_s})} Q^{Bb}(\boldsymbol{k_s})}. \tag{5.20}$$

Expression (5.20) shows that for the purpose of computing the parent's CoR the children's CoRs can be considered as regular sources and the standard CoR formula (5.10) applies. Hierarchical clustering can also be shown to analytically hold under partitioning of the sources based on the complex plane quadrants (Algorithm 1). To conserve space we numerically validate the hierarchical clustering of sources grouped based on quadrants of the complex plane given in (5.12). Table 1 gives the complex locations of CoR $\boldsymbol{r}_{\Sigma,++}^{B}$ obtained both directly and hierarchically using Algorithm 1 under 2-level partitioning of the box containing the sources. The CoR was computed for a random distribution of $N = 100$ time-harmonic point sources in a $1mm$ parent box B for observation direction $\hat{\boldsymbol{r}} = -0.55\hat{\boldsymbol{x}} - 0.64\hat{\boldsymbol{y}} + 0.54\hat{\boldsymbol{z}}$ and $k_0 = 500$.

Table 5.1: Parent CoRs $\boldsymbol{r}^B_{\Sigma,++}$ obtained directly and recursively from children's CoRs $\boldsymbol{r}^{Bb}_{\Sigma,++}$, $\boldsymbol{r}^{Bb}_{\Sigma,+-}$, $\boldsymbol{r}^{Bb}_{\Sigma,-+}$, $\boldsymbol{r}^{Bb}_{\Sigma,--}$, $b = 1, ..., 8$

	Directly		Recursively	
	$\Re[mm]$	$\Im[\mu m]$	$\Re[mm]$	$\Im[\mu m]$
x^B_Σ	0.543954	17.969	0.543954	17.969
y^B_Σ	0.586232	15.8741	0.586232	15.8741
z^B_Σ	0.492261	-18.1524	0.492261	-18.1524

5.4 Numerical Results and Discussion

The behavior of the BH-CoR maximum approximation error (5.14) versus wavenumber k_0 is shown in Fig. 5.3. We found numerically that the worst-case error for our proposed BH-CoR algorithm is achieved when there are two source points located in opposite corners of the source box. We evaluated the error for three values of the ratio $\theta = B/D$, D being the shortest distance from the box to observation point. While the relative error drops off as $1/D$, a drastic increases in error is observed when the electric size of the box B/λ exceeds 0.1. This indicates the quasi-static nature of the proposed algorithm. For comparison the worst-case error is also shown for the high-frequency FMM method (HF-FMM) [2]. The worst case source configuration for both FMM versions is a single point source located at the corner of the source box and evaluated with one box of separation [6]. The rapid increase in HF-FMM approximation error at lower frequencies is clearly observed. The point of intersection of the HF-FMM error curve with that of the proposed BH-CoR method illustrates that when two digits of precision suffice the latter may be used in conjunction with HF-FMM for construction of a broadband tree-based $O(N \log N)$ algorithm. With the purpose of providing a reference to an alternative low-frequency fast algorithm we also show in Fig. 5.3 the behavior of worst-case error for the low-frequency FMM (LF-FMM) for the same example. The LF-FMM error is shown for multipole expansion of orders

up to 9. One can see that the proposed BH-CoR approximation (5.14) at distances to the observation point at least five box sizes away ($\theta = 0.2$) provides accuracy of field approximation error superior to that of a fifth order LF-FMM approximation.

The CoR field approximation is inaccurate for high frequencies because of the stationary phase approximation [4] and because the field is approximated by monopole sources rather than multipole sources. In practical applications it may be desirable to combine the proposed BH-CoR method with a high-frequency method to overcome this limitation. One approach is to use BH-CoR to accelerate the near interactions of HF-FMM. The near interaction step of HF-FMM is of $O(NM)$ complexity whereas BH-CoR can perform the same step in $O(N \log M)$ complexity, assuming that all HF-FMM leaf boxes contain exactly M sources.

It should also be noted that in a practical implementation of the proposed algorithm one would only store the CoRs for a few observation angles and use local interpolation [5] of the band-limited CoR field to evaluate its value for an arbitrary angle.

5.5 Conclusion

A new tree-based algorithm for an $O(N \log N)$ solution of the N-body problem with the scalar Helmholtz kernel is proposed. In the upward tree traversal the center-of-radiation approximating the field of sources contained in a given node of the tree is computed recursively. The magnitude and complex location of the center-of-radiation is obtained by matching its field spectrum to the field spectrum of the true sources in the vicinity of the stationary phase point. The method turns identically into the Barnes-Hut algorithm in the limit as the time-harmonic frequency approaches zero and therefore can be viewed as the extension of the BH algorithm to the Helmholtz kernel. The method becomes ineffective for electric sizes exceeding 0.1 wavelengths. The practical appli-

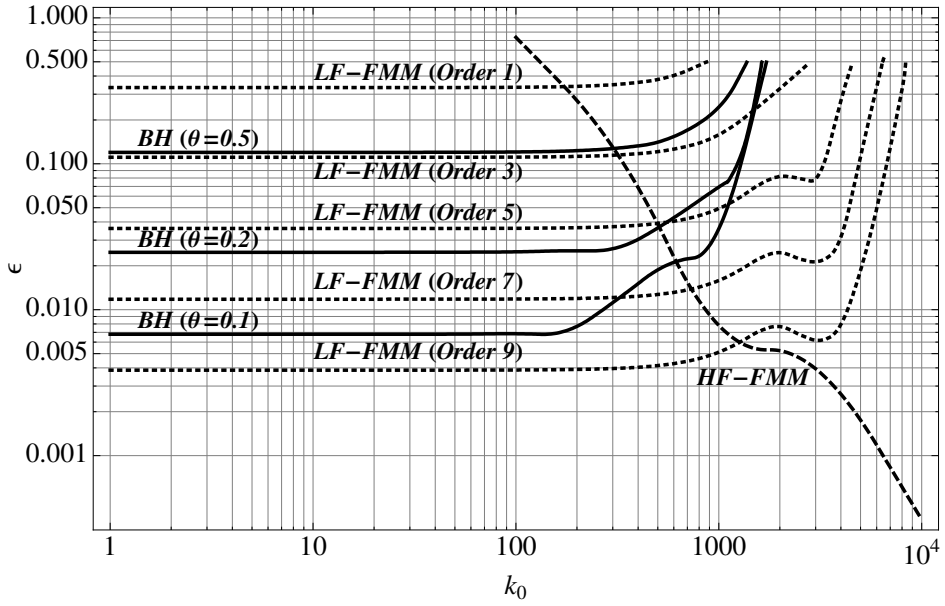

Figure 5.3: Worst-case relative error of the field approximation versus frequency by the proposed BH-CoR algorithm, high-frequency FMM and low-frequency FMM for a source box of size $B = 1mm$. The error is computed for the worst-case source configuration and by finding the observation angle which yields the maximum error.

cations of the algorithm can be found in fast characterization of electrically small structures as well as in a combined implementation with high-frequency FMM for constructing broadband full-wave electromagnetic solvers.

References

[1] Andriulli, F.P., et.al., "A Multiplicative Calderon Preconditioner for the Electric Field Integral Equation," *IEEE Trans. Antennas Propag.,* vol. 56, no. 6, pp. 2398-2412, Aug. 2008

[2] H. Cheng, et.al., "A wideband FMM for the Helmholtz equation in three dimensions" *J. Comp. Phys.* vol. 216, no. 1, pp. 300-325, July 2006.

[3] J. Barnes and P. Hut, "A Hierarchical O(n log n) force calculation algorithm," *Nature,* v. 324, Dec. 1986.

[4] W.C. Chew, *Waves and Fields in Inhomogeneous Media,* Piscataway, NJ: IEEE Press, 1995.

[5] W.C. Chew, et.al, *Fast and Efficient Algorithms in Computational Electromagnetics,* Artech House Publishers, 2000.

[6] L. Jiang, *Studies on low frequency fast multipole algorithms,* Ph.D. dissertation, University of Illinois at Urbana-Champaign, 2004.

Chapter 6

Broadband Full-Wave Modeling

In the previous chapter, we introduced an extension to the Barnes-Hut algorithm that can be applied to the solution of full-wave problems at low frequencies. Since it was based on the scalar Helmholtz kernel it was applicable to the solution of a mixed potential form of EFIE. As the frequency increases beyond the quasi-static regime, the EFIE becomes ill-posed at certain discrete frequencies which correspond to spurious resonances of the scatterer. In this chapter, we introduce the Magnetic Field Integral Equation (MFIE) and show that it can be combined with EFIE to formulate the Combined Field Integral Equation (CFIE) which is free of spurious resonances. In addition, the EFIE suffers from a low-frequency breakdown problem that leads to inaccurate results at very low frequencies, and we will discuss remedies to this problem. This will lay the foundation for the FMM algorithm that is presented in the next chapter which is applicable to the aforementioned integral equations all the way from statics up to the high frequency domain.

6.1 The Magnetic Field Integral Equation

Consider an arbitrarily shaped perfect electric conductor (PEC) with volume V and surface S. Let $\mathbf{H}^{inc}(\mathbf{r})$ represent a magnetic field due to external sources

that impinges on the object. The incident field will induce a surface current $\mathbf{J}(\mathbf{r})$ on the object, which in turn produces a scattered magnetic field $\mathbf{H}^{scat}(\mathbf{r})$. Since the object is a PEC, the total magnetic field vanishes inside object

$$\mathbf{H}^{scat}(\mathbf{r}) + \mathbf{H}^{inc}(\mathbf{r}) = 0 \quad \mathbf{r} \in V. \tag{6.1}$$

The tangential magnetic field is discontinuous across the surface that carries the electric current. This results in the following boundary condition on the surface of the object

$$\hat{\mathbf{n}} \times \mathbf{H}^{scat}(\mathbf{r}) + \hat{\mathbf{n}} \times \mathbf{H}^{inc}(\mathbf{r}) = \mathbf{J}(\mathbf{r}) \quad \mathbf{r} \in S^{+} \tag{6.2}$$

where S^{+} denotes a surface that is exterior to the object by an infinitesimally distance. The scattered field can be expressed by summing up the contributions from the induced surface currents as

$$\mathbf{H}^{scat}(\mathbf{r}) = i\omega\mu \int_{S} \bar{\mathbf{G}}_{m0}(\mathbf{r}, \mathbf{r}') \cdot \mathbf{J}(\mathbf{r}') d\mathbf{r}' \tag{6.3}$$

where

$$\bar{\mathbf{G}}_{m0}(\mathbf{r}, \mathbf{r}') = \nabla \mathrm{G}_0(\mathbf{r}, \mathbf{r}') \times \bar{\mathbf{I}} \tag{6.4}$$

is the magnetic-type dyadic Green's function and $\mathrm{G}_0(\mathbf{r}, \mathbf{r}')$ is the Green's function to the scalar Helmholtz equation given by (4.5). Substituting (6.3) into (6.2) yields

$$\hat{\mathbf{n}} \times \int_{S} \bar{\mathbf{G}}_{m0}(\mathbf{r}, \mathbf{r}') \cdot \mathbf{J}(\mathbf{r}') d\mathbf{r}' + \hat{\mathbf{n}} \times \mathbf{H}^{inc}(\mathbf{r}) = \mathbf{J}(\mathbf{r}) \quad \mathbf{r} \in S^{+} \tag{6.5}$$

In the case when the observation point is located exactly on the surface S, Cauchy's principal value method can be applied to the above equation to extract the singularity in the Green's function as

$$\frac{1}{2}\mathbf{J}(\mathbf{r}) - \hat{\mathbf{n}} \times P.V. \int_{S} \bar{\mathbf{G}}_{m0}(\mathbf{r}, \mathbf{r}') \cdot \mathbf{J}(\mathbf{r}') d\mathbf{r}' = \hat{\mathbf{n}} \times \mathbf{H}^{inc}(\mathbf{r}) \quad \mathbf{r} \in S \tag{6.6}$$

where $P.V.$ denotes the principal value integral. The above relationship is the standard formulation of MFIE and detailed derivations can be found in [Gib07]. If the object is electrically small and contain sharp edges, it is necessary to re-formulate (6.6) as discussed in [RUP01]. MFIE is only valid for closed objects, whereas EFIE is also applicable to thin and open surfaces.

6.2 The Combined Field Integral Equation

The EFIE imposes the condition of vanishing tangential electric field on the surface of the PEC object whereas the field inside the object is assumed to vanish due to analytic continuity of the fields throughout its source-free volume. This formulation, however, does not distinguish between a solid PEC object and a hollow thin-shelled PEC object. As a result, at resonant frequencies the fields from the EFIE solution for a solid PEC object will act as those from a thin-shelled resonant cavity with non-physical fields throughout its volume. Mathematically, there exist null-space solutions that satisfies the EFIE equations with zero incident field. These null-space solutions add additional current to the solution at resonant frequencies and can be interpreted as interior resonant modes of the object. The solution to EFIE becomes non-unique at the internal resonance frequencies. At frequencies close to the internal resonances EFIE becomes ill-posed and its discretization results in an ill-conditioned system of linear algebraic equations because the resonance conditions are almost satisfied.

MFIE also suffers from the internal resonances albeit these resonances occur at different frequencies than those of EFIE. The resonances in MFIE are similar in nature to the resonances of EFIE and correspond to the resonant modes of a analogous hollow cavity with perfect magnetic conductor (PMC) walls. A comprehensive analysis of the internal resonance problem for EFIE and MFIE can be found in [CTH08]. An important property is that the null-space solutions to EFIE and MFIE differs and so does the frequencies at which they occur. CFIE is formulated as a linear combination of EFIE and MFIE as

$$\text{CFIE} = \alpha \cdot \text{EFIE} + \eta(1-\alpha) \cdot \text{MFIE} \tag{6.7}$$

where α is a weighting parameter that is normally chosen within $0.2 \leq \alpha \leq 0.5$ and η is the intrinsic impedance of the surrounding space. The purpose of the η factor is to equalize MFIE to the level of EFIE. By combining EFIE and MFIE, both boundary conditions are satisfied simultaneously and the internal

resonances are eliminated. The system matrix in CFIE is generally better conditioned than for EFIE or MFIE which can significantly reduce the number of iterations for iterative matrix solvers.

6.3 Low Frequency Breakdown Problems

At low frequencies where the object is much smaller than a wavelength there is normally no benefit with using CFIE. The internal resonances do not occur in the low frequency regime since their formation require a closed path of wave propagation inside the cavity that is at least one wavelength in length. In addition, MFIE has accuracy problems at low frequencies [ZCCZ03]. Therefore, EFIE is typically used for scattering problems at low frequencies. However, EFIE also suffers from numerical instabilities at low frequencies as the level of the vector potential contribution goes below the error level of scalar potential contribution in (4.15). The ratio of the vector potential term to the scalar potential term in (4.15) is proportional to the square of the electrical length of the source basis function. Hence, when the mesh elements are much smaller than a wavelength the vector potential vanishes due to finite precision of computer arithmetic. The EFIE system matrix becomes rank deficient without the vector potential contribution since the solution to the scalar potential is non-unique.

Several methods have been proposed for elimination of the low-frequency breakdown of EFIE. The loop-tree (or loop-star) basis [LLB03, Vec99] rearranges the RWG basis functions into loops that naturally corresponds to divergence-free current and tree (star) basis functions that provide the current with non-zero divergence. This stabilizes the scalar potential term and thereby extends the validity of EFIE to lower frequencies. Augmented-EFIE (AEFIE) [QC08] and the Current and Charge Integral Equation (CCIE) [TYO06] introduce additional unknowns in order to decompose and normalize the contributions from the vector and scalar potentials. Preconditioners based on

the Calderon identities have also been shown to stabilize EFIE to very low frequencies [ACB+08, SLCM13, YJN10].

6.4 Broadband Analysis with FMM

As discussed in Chapter 1, there no universal version of FMM that is efficient at all frequencies. The popular HF-FMM is the most efficient version of FMM for full-wave modeling at high frequencies but it is unable to accelerate interactions between basis functions that are separated by less than about a half-wavelength when 2 digits of precision is required. At higher accuracy requirements, the breakdown is much more severe and renders HF-FMM inefficient. Several remedies have been proposed in the literature as surveyed in Chapter 1. In the next chapter, we will introduce a new version of FMM that is stable and efficient from the low frequency regime up to high frequency domains of 100 wavelengths in size. The method is also easily extendable to handling of the EFIE, MFIE, and CFIE kernels as well as their low-frequency modifications (e.g. AEFIE and CCIE).

Chapter 7

Vectorial Low-Frequency MLFMA for the Combined Field Integral Equation

A vectorial Low-Frequency Multi-Level Fast Multipole Algorithm (LF-MLFMA) is proposed for acceleration of interactions resultant from the Method of Moments (MoM) discretization of the Combined Field Integral Equation (CFIE). The derivatives relating the scalar Green's function to its dyadic counterparts are defined via recursive identities for scalar wave functions. The method evaluates the matrix vector product in MoM by performing three scalar LF-MLFMA passes. It is demonstrated to be stable for scatterers spanning up to 110 wavelengths in size. As the method does not impose any restrictions on the depth of the MLFMA tree, it is suitable for the solution of both broadband and multi-scale problems.

7.1 Introduction

The MLFMA is today's most powerful method for solving large-scale electromagnetic problems with the boundary-element MoM [1]. It reduces the computational work and memory in each iteration of the iterative solution of the MoM matrix equation from $O(N^2)$ to $O(N \log N)$, where N is the number of unknowns in the MoM discretization. For models that exhibits multi-scale features, however, both the underlying MoM formulation and MLFMA acceleration schemes must be modified to maintain efficiency. For the MoM this is due to the low-frequency and/or oversampling breakdown of the underlying Electric Field Integral Equation (EFIE). The common MLFMA, herein refered to as High-Frequency MLFMA (HF-MLFMA), breaks down at low frequencies due to its inability to capture the evanescent modes of the field [2]. In this paper, we propose a vectorial LF-MLFMA that is based on spherical basis functions [2, 3, 4] and show that it may be a particularly good choice for solving multi-scale problems.

Two classes of MLFMA have been proposed in the literature for accelera-

tion of interactions at low-frequencies (LF) which are suitable for combining with HF-MLFMA to construct MLFMAs that are efficient at all frequencies. The first class works with the original HF-MLFMA by extending its addition theorem to capture both the propagating and evanescent parts of the field. This has been achieved by either using translation methods that are based on the spectral representation of the Green's function [5] or by using QR compression to construct an efficient representation of the translation matrix [6]. These methods preserve the asymptotic complexity of HF-MLFMA but require additional work which makes them considerably slower than HF-MLFMA. The second class of LF-MLFMA is based on a multipole decomposition of the Green's function, where the incoming and outgoing fields are expressed as expansions of spherical basis functions [2, 3, 4]. This representation requires the use of translation operators of higher asymptotic complexity than HF-MLFMA and is therefore less efficient at high frequencies. The method is, however, efficient at low and mid frequencies which makes it suitable for the solution of multi-scale geometries up to about a hundred wavelengths in size without combing it with HF-MLFMA.

In this paper, we show that the second class of LF-MLFMA can accelerate the solution of electrically large multi-scale geometries and propose the following improvements:

- We extend LF-MLFMA to the CFIE kernel. Previous work has been limited to the EFIE kernel [4].

- We show that both the EFIE and CFIE kernels can be evaluated with the same memory requirement as the scalar kernel. The run time is increased by a factor of three or four over the scalar kernel, depending on the utilized EFIE formulation [1, 7]

7.2 Field Expansions in Scalar Low-Frequency MLFMA

Consider the following elementary spherical wave functions satisfying the scalar Helmholtz equation, $\nabla^2\psi + k^2\psi = 0$,

$$\psi_n^{m,in}(\mathbf{r}) = j_n(k_0 r)Y_n^m(\theta,\phi), \tag{7.1}$$

$$\psi_n^{m,out}(\mathbf{r}) = h_n(k_0 r)Y_n^m(\theta,\phi), \tag{7.2}$$

where $\psi_n^{m,in}$ denotes an elementary incoming spherical wave of degree n and order m, and similarly $\psi_n^{m,out}$ denotes an elementary outgoing spherical wave of degree n and order m. In (7.1), (7.2) and throughout the subsequent derivations the time-harmonic dependence $e^{-i\omega t}$ with angular frequency ω is assumed and suppressed for brevity. Functions j_n and h_n denote the spherical Bessel function of order n and the spherical Hankel function of the first kind and order n, respectively. Y_n^m denotes the spherical harmonic of degree n and order m with the following normalization

$$Y_n^m(\theta,\phi) = (-1)^m\sqrt{\frac{2n+1}{4\pi}\frac{(n-|m|)!}{(n+|m|)!}}P_n^{|m|}(\cos\theta)e^{im\phi} \tag{7.3}$$

where P_n^m is the associated Legendre function of degree n and order m.

The field Φ produced at location $\mathbf{r}$ by a spatial distribution of N point sources with locations $\mathbf{r}'_1$, $\mathbf{r}'_2$, ..., $\mathbf{r}'_N$ and magnitudes q_1, q_2, ..., q_N is given by

$$\Phi(\mathbf{r}) = \frac{ik_0}{4\pi}\sum_{k=1}^{N} q_k h_0(k_0\|\mathbf{r}-\mathbf{r}'_k\|). \tag{7.4}$$

If the sources are enclosed by a sphere S centered at origin, then the field Φ at an observation point $\mathbf{r}$ exterior to S is bandlimited [3]. Thus, it can be approximated to arbitrary precision ϵ [2] by a truncated expansion over outgoing spherical waves

$$\Phi(\mathbf{r}) \approx \sum_{n=0}^{P}\sum_{m=-n}^{n}\alpha_n^m\psi_n^{m,out}(\mathbf{r}), \quad \mathbf{r}\notin S. \tag{7.5}$$

The expansion coefficients $\{\alpha_n^m\}$ in (7.5) are given by

$$\alpha_n^m = ik \sum_{k=1}^{N} q_k \psi_n^{-m,in}(\mathbf{r}'_k), \quad \mathbf{r}_k \in S \tag{7.6}$$

and P is the truncation order determined by the electrical radius of sphere S and desired precision ϵ. Similarly, if the sources are located outside sphere S, we can approximate the field in the interior of S by expanding over incoming spherical wave functions

$$\Phi(\mathbf{r}) \approx \sum_{n=0}^{P} \sum_{m=-n}^{n} \beta_n^m \psi_n^{m,in}(\mathbf{r}), \quad \mathbf{r} \in S, \tag{7.7}$$

and expansion coefficients $\{\beta_n^m\}$

$$\beta_n^m = ik_0 \sum_{k=1}^{N} q_k \psi_n^{m,out}(\mathbf{r}'_k), \quad \mathbf{r}'_k \notin S. \tag{7.8}$$

In accordance with the addition theorem [3] the elementary spherical wave functions can be shifted to another expansion center $\mathbf{r}_c$,

$$\psi_n^{m,*}(\mathbf{r}) = \sum_{n'=0}^{P'} \sum_{m'=-n'}^{n'} \gamma_{n',n}^{m',m} \psi_{n'}^{m',*}(\mathbf{r} - \mathbf{r}_c), \tag{7.9}$$

where $*$ denotes either *in* or *out* and P' is the truncation order of the new expansion. As the expansion center changes from the origin to $\mathbf{r}_c$ the bounding sphere changes from S to S'. Thus, in order to maintain desired precision ϵ the new truncation order P' must determined based on the electrical radius of S'. Similarly, the outgoing expansion can be converted to an incoming expansion,

$$\psi_n^{m,in}(\mathbf{r}) = \sum_{n'=0}^{P'} \sum_{m'=-n'}^{n'} \kappa_{n',n}^{m',m} \psi_{n'}^{m',out}(\mathbf{r} - \mathbf{r}_c). \tag{7.10}$$

To maintain the same precision ϵ in re-expanded expressions (7.9) and (7.10) the new order P' must be chosen according to the electric radius of new bounding sphere S'. Several methods for computing the re-expansion coefficients,

$\gamma_{n',n}^{m',m}$ and $\kappa_{n',n}^{m',m}$, have been proposed in the literature [3, 2]. Direct computation of the coefficients in terms of Wigner 3-j symbols lead to $O(P'^5)$ or $O(P'^6)$ computational complexity in (7.9) and (7.10). This is acceptable for electrically small bounding regions S' and low accuracy levels ϵ [4]. The procedure, however, becomes prohibitively expensive as the electric radius of S' increases. The $O(P'^5)$ complexity can be reduced to $O(P'^4)$ by using appropriate recurrence relations in the computation of the coefficients $\kappa_{n',n}^{m',m}$ [3]. Furthermore, if the translation is carried along the z-axis, it can be shown that $\gamma_{n',n}^{m',m} = 0$ and $\kappa_{n',n}^{m',m} = 0$ for all $m \neq m'$ and $n' < |m|$ and the translation complexity is reduced to $O(P'^3)$. $O(P'^3)$ complexity can be obtained for arbitrary translation directions by first rotating the coordinate system so that the translation direction is co-linear with its z-axis and then performing a second rotation back to the original coordinate system after the translation has been done [3]. This $O(P'^3)$ translation methodology is utilized in our implementation.

Since the spherical wave functions (7.1), (7.2) are composed of standard special functions, their derivatives can be written in terms of the following recursive formulas involving the same spherical functions but of different indices

$$\begin{aligned}\partial_x \psi_n^{m,*}(\mathbf{r}) = \frac{k_0}{2}\big(&b_{n+1}^{-m-1}\psi_{n+1}^{m+1,*}(\mathbf{r}) + b_{n+1}^{m-1}\psi_{n+1}^{m-1,*}(\mathbf{r}) \\ &- b_n^m \psi_{n-1}^{m+1,*}(\mathbf{r}) - b_n^{-m}\psi_{n-1}^{m-1,*}(\mathbf{r})\big)\end{aligned} \tag{7.11}$$

$$\begin{aligned}\partial_y \psi_n^{m,*}(\mathbf{r}) = \frac{k_0}{2}\big(&-b_{n+1}^{-m-1}\psi_{n+1}^{m+1,*}(\mathbf{r}) + b_{n+1}^{m-1}\psi_{n+1}^{m-1,*}(\mathbf{r}) \\ &+ b_n^m \psi_{n-1}^{m+1,*}(\mathbf{r}) - b_n^{-m}\psi_{n-1}^{m-1,*}(\mathbf{r})\big)\end{aligned} \tag{7.12}$$

$$\partial_z \psi_n^{m,*}(\mathbf{r}) = k_0\left(a_{n-1}^m \psi_{n-1}^{m,*}(\mathbf{r}) - a_n^m \psi_{n+1}^{m,*}(\mathbf{r})\right) \tag{7.13}$$

where the coefficients are defined by

$$a_n^m = \begin{cases} \sqrt{\frac{(n+1+m)(n+1-m)}{(2n+1)(2n+3)}} & \text{if } |m| \leq n, \\ 0 & \text{otherwise.} \end{cases} \tag{7.14}$$

$$b_n^m = \begin{cases} \text{sign}(m)\sqrt{\frac{(n-m-1)(n-m)}{(2n-1)(2n+1)}} & \text{if } |m| \leq n, \\ 0 & \text{otherwise.} \end{cases} \tag{7.15}$$

and sign(x) is the signum function. The above recursive relations are key to rapid evaluation of the derivatives entering into the dyadic Green's function kernels of the EFIE and MFIE. Proofs of the above differentiation theorems (7.11)-(7.13) can be found in [3].

In scalar LF-MLFMA, expansions (7.5) and (7.7) are computed for each box in its hierarchical tree data. Equation (7.6) is used to compute the outgoing expansion coefficients at the leaf level whereas outgoing expansions at the other levels are obtained by hierarchically aggregating the leaf box expansions by using (7.9). The incoming expansions are computed by translating the outgoing expansions to incoming expansions with (7.10), level by level. The incoming expansions are finally hierarchically disaggregated down to the leaf level with (7.9) and evaluated at the observation points (7.7). By selecting P appropriately for each level, we can control the accuracy in LF-MLFMA up to $\epsilon = 10^{-12}$ in double precision arithmetic. At the same time the expansion stability considerations [2] allow us to maintain desired accuracy (down to $\epsilon = 10^{-12}$ if needed) for geometries (width of MLFMA root box) exceeding 100 wavelengths and without any restrictions on the depth of the tree.

7.3 Novel Variant of the Vectorial Low-Frequency MLFMA

In the vectorial LF-MLFMA we accelerate evaluation of the electric field, $\mathbf{E}(\mathbf{r}_\ell)$, and magnetic field, $\mathbf{H}(\mathbf{r}_\ell)$, at L locations $\mathbf{r}_\ell$, due to electric current distribution $\mathbf{J}(\mathbf{r}'_k)$ discretized over a finite number of quadrature points, $\mathbf{r}'_1$, $\mathbf{r}'_2$, ..., $\mathbf{r}'_N$

$$\mathbf{E}(\mathbf{r}_\ell) = \sum_{k=1}^{N} \left[1 + \frac{1}{k_0^2} \nabla\nabla\cdot \right] \left[h_0(k_0\|\mathbf{r} - \mathbf{r}'_k\|)\mathbf{J}(\mathbf{r}'_k) \right], \tag{7.16}$$

$$\mathbf{H}(\mathbf{r}_\ell) = \frac{1}{k_0} \sum_{k=1}^{N} \nabla \times \left[h_0(k_0\|\mathbf{r} - \mathbf{r}'_k\|)\mathbf{J}(\mathbf{r}'_k) \right], \quad \ell = 1, ..., L. \tag{7.17}$$

In the proposed algorithm, we let the expansions in LF-MLFMA approximate the magnetic vector potential, $\tilde{\mathbf{A}}(\mathbf{r})$ defined by

$$\tilde{\mathbf{A}}(\mathbf{r}) = \sum_{k=1}^{N} h_0(k_0\|\mathbf{r}-\mathbf{r}'_k\|)\mathbf{J}(\mathbf{r}'_k). \tag{7.18}$$

The vectorial expansion coefficients in the outgoing field (7.5) and incoming field (7.7) are obtained directly from (7.6) and (7.8). The upward and downward passes in vectorial LF-MLFMA are performed by three scalar LF-MLFMA passes, one for each component of the vector potential. The significant change in the proposed method lies in how the incoming expansions are evaluated at the leaf level. Rather than evaluating $\tilde{\mathbf{A}}(\mathbf{r})$, we convert $\tilde{\mathbf{A}}(\mathbf{r})$ to $\mathbf{E}(\mathbf{r})$ and $\mathbf{H}(\mathbf{r})$ by first substituting (7.18) into (7.16) and (7.17)

$$\mathbf{E}(\mathbf{r}) = \left[1 + \frac{1}{k_0^2}\nabla\nabla\cdot\right]\tilde{\mathbf{A}}(\mathbf{r}) \tag{7.19}$$

$$\mathbf{H}(\mathbf{r}) = \frac{1}{k_0}\nabla\times\tilde{\mathbf{A}}(\mathbf{r}) \tag{7.20}$$

where $\tilde{\mathbf{A}}(\mathbf{r})$ is approximated with incoming expansions at the leaf level

$$\mathbf{E}(\mathbf{r}) \approx \sum_{n=0}^{P}\sum_{m=-n}^{n}(1+\frac{1}{k_0^2}\nabla\nabla\cdot)(\boldsymbol{\beta}_n^m\psi_n^{m,in}(\mathbf{r})) \tag{7.21}$$

$$\mathbf{H}(\mathbf{r}) \approx \sum_{n=0}^{P}\sum_{m=-n}^{n}\nabla\times(\boldsymbol{\beta}_n^m\psi_n^{m,in}(\mathbf{r})). \tag{7.22}$$

After expanding the differentiation operators we can obtain scalar expression for the each component of $\mathbf{E}(\mathbf{r})$ and $\mathbf{H}(\mathbf{r})$

$$\begin{aligned} E_x(\mathbf{r}) \approx \sum_{n=0}^{P}\sum_{m=-n}^{n} &(\boldsymbol{\beta}_n^m)_x\psi_n^{m,in}(\mathbf{r}) + \frac{1}{k_0^2}(\boldsymbol{\beta}_n^m)_x\partial_{xx}\psi_n^{m,in}(\mathbf{r}) \\ &+ \frac{1}{k_0^2}(\boldsymbol{\beta}_n^m)_y\partial_{xy}\psi_n^{m,in}(\mathbf{r}) + \frac{1}{k_0^2}(\boldsymbol{\beta}_n^m)_z\partial_{xz}\psi_n^{m,in}(\mathbf{r}) \end{aligned} \tag{7.23}$$

$$\begin{aligned} H_x(\mathbf{r}) \approx \sum_{n=0}^{P}\sum_{m=-n}^{n} &-\frac{1}{k_0}(\boldsymbol{\beta}_n^m)_y\partial_z\psi_n^{m,in}(\mathbf{r}) \\ &+ \frac{1}{k_0}(\boldsymbol{\beta}_n^m)_z\partial_y\psi_n^{m,in}(\mathbf{r}) \end{aligned} \tag{7.24}$$

where expression for the fields' y and z-components are omitted for brevity. Equations (7.11)-(7.13) can be directly applied to each components of $\mathbf{E}(\mathbf{r})$ and $\mathbf{H}(\mathbf{r})$ to obtain a new set of expansions coefficients which are used by our proposed version of LF-MLFMA to evaluate the field at the observation points. We omit the derivation of the expansion coefficients in this paper as it is both straightforward and lengthy. The new leaf level incoming expansions become

$$\mathbf{E}(\mathbf{r}) \approx \sum_{n=0}^{P-2} \sum_{m=-n}^{n} \boldsymbol{\beta}_n^{m,E} \psi_n^{m,in}(\mathbf{r}) \tag{7.25}$$

$$\mathbf{H}(\mathbf{r}) \approx \sum_{n=0}^{P-1} \sum_{m=-n}^{n} \boldsymbol{\beta}_n^{m,H} \psi_n^{m,in}(\mathbf{r}) \tag{7.26}$$

In our implementation, the field coefficients $\{\boldsymbol{\beta}_n^{m,E}\}$ and $\{\boldsymbol{\beta}_n^{m,H}\}$ are computed by performing a single pass over the vector potential coefficients $\{\boldsymbol{\beta}_n^{m}\}$ and applying the recursion relations. Though the computational cost is of $O(P^2)$ it is insignificant compared to the other steps in LF-MLFMA provided all the coefficients in the recursion relations are precomputed. As a direct consequence of (7.11)-(7.13), each order of differentiation of an expansion over spherical wave functions reduces the truncation order by one. Hence, the truncation orders become $P-2$ in (7.25) and $P-1$ in (7.26). To maintain the same expansion order as the scalar version, we have increased expansion order P by 1 or 2 depending on which vector kernel is being computed. This is similar to the increase in expansion order when going from scalar high-frequency MLFMA to a vectorial one [8].

7.4 Numerical Results

To test the proposed vectorial LF-MLFMA both electrically small but highly oversampled targets and electrically large targets are examined. In the first experiment we consider a sphere of radius $1m$ centered at the origin and discretized with $1,624,640$ flat surface triangular elements. The sphere is excited

Algorithm 3 Vectorial LF-MLFMA

for $c = \{x, y, z\}$ *(loop over each component)* **do**
  for $k = 1, \ldots, N$ *(N is the number of source points)* **do**
    $q_k \leftarrow (\mathbf{J}(\mathbf{r}'_k))_c$ *(set magnitudes in (7.6))*
  end for
  Perform a full pass with scalar LF-MLFMA omitting the final evaluation at the leaf level
  for $b = 1, \ldots, B$ *(B is the number of leaf boxes)* **do**
    for $n = 0, \ldots, P, m = -n, \ldots, n$ **do**
      $(\boldsymbol{\beta}_n^m)_c \leftarrow \beta_n^m$ *(save expansion coefficients)*
    end for
  end for
end for
for $b = 1, \ldots, B$ **do**
  Convert $\{\boldsymbol{\beta}_n^m\}$ to $\{\boldsymbol{\beta}_n^{m,E}\}$ and/or $\{\boldsymbol{\beta}_n^{m,H}\}$
  Evaluate expansions (7.25) and/or (7.26) at all observation points in box b.
end for

by the volumetric current $\mathbf{j} = \mathbf{I}\ell\delta(\mathbf{r} - \mathbf{r}')$ of radial electric dipole with dipole moment $\mathbf{I}\ell = \hat{\mathbf{z}} \cdot 1A \cdot m$ and location $\mathbf{r}' = \hat{\mathbf{z}} \cdot 10m$. The time snapshots at $t = 0s$ of the current density $\mathbf{J}(\mathbf{r}) = \hat{\theta}\Re[J_\theta(\theta)e^{-i\omega t}]$ produced on the surface of the sphere by the radial electric dipole at $\omega = 2\pi \cdot 7.5GHz$ and at $\omega = 2\pi \cdot 1.5MHz$ are shown in Fig. 7.1. The solid curve corresponds to the solution obtained with the CFIE Rao-Wilton-Glisson (RWG) MoM solution and accelerated with the proposed LF-MLFMA. The CFIE-RWG formulation is weighted 0.2 to EFIE and 0.8 to MFIE and has $2,436,960$ unknowns. The analytic Mie series solution is shown with dashed lines in the same figure to validate the method. Each iteration took $1367s$ ($7.5GHz$), $781s$ ($1.5MHz$) and a breakdown of the time spent by LF-MLFMA is shown in Table 7.1. The peak memory usage in these examples were $39.9GB$ ($7.5GHz$) and $35.3GB$ ($1.5MHz$) which includes storage for 393 million non-zero element in the sparse near-field MoM impedance matrix and 604 million non-zero elements in the LU-factored preconditioner which contained 12 million non-zero elements prior to factorization. The preconditioned GMRES matrix solver converged to a residual of 10^{-4} in 27 ($7.5GHz$) and 17 ($1.5MHz$) iterations.

In the second example, we apply the proposed vectorial LF-MLFMA to accelerate the RWG-CFIE solution of a $9.2m$ rocket discretized with a surface mesh with $972,576$ triangles, which corresponds to $1,458,864$ unknowns. The target is excited by an electric dipole at $3.6GHz$ positioned on the target's geometrical axis $2m$ away from rocket's tip and directed collinear with the axis. The snap shot at $t = 0s$ of time-harmonic current density magnitude $|\mathbf{J}(\mathbf{r})| = |\Re\mathbf{J}(\mathbf{r}'_k)e^{-i\omega t}|$ is shown in Fig. 7.2. At $3.6GHz$ the length of the target spans 110λ. The total run time for this example was $17340s$. The preconditioned GMRES matrix solver converged to a final residual of $8.7 \cdot 10^{-4}$ in 18 iterations. Each matrix-vector product took $802s$ of CPU time. The MLFMA tree had 9 levels and a root box width of 110λ. The peak memory usage was $27.9GB$, which includes the storage for the sparse near-matrix with 319 million non-zero elements and the LU-factored preconditioner

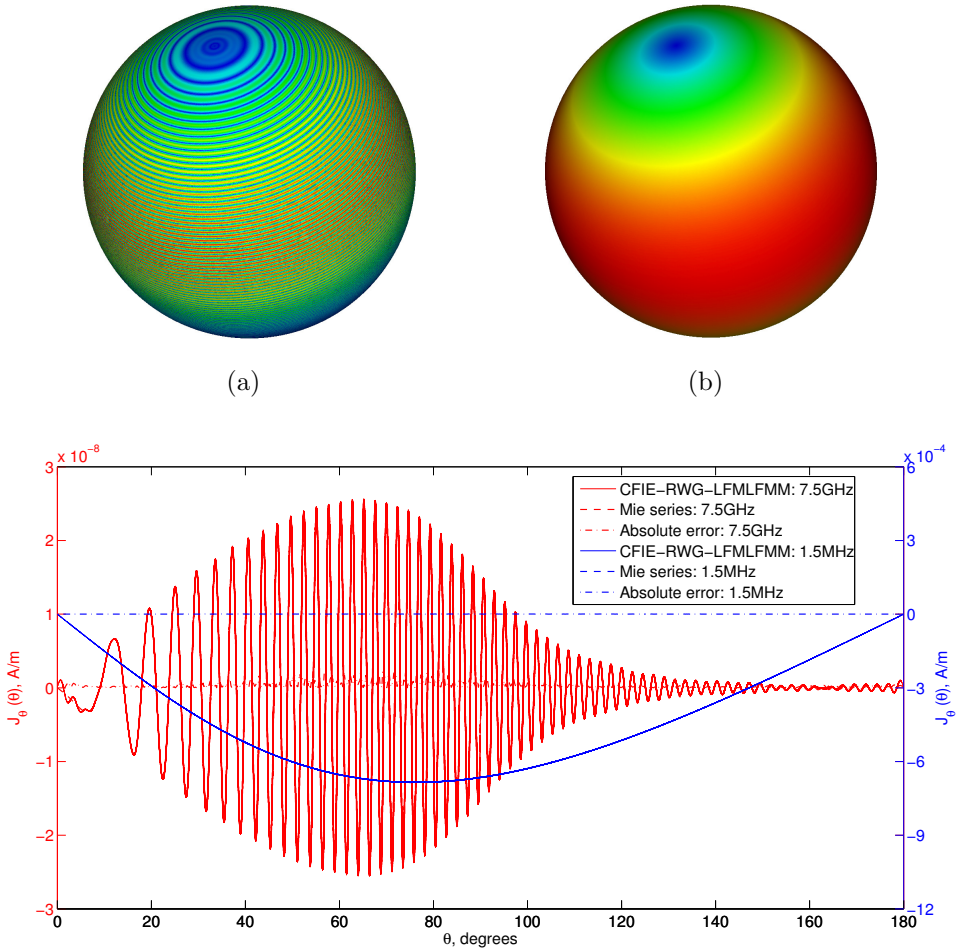

(a) (b)

(c)

Figure 7.1: A snapshot of time-harmonic current density on the surface of a sphere of radius $1m$ that is excited by a radial electric dipole at $7.5GHz$ (a) and $1.5MHz$ (b). The current density is plotted as a function of θ in (c) for the numerical solutions, the analytic solutions, and the corresponding absolute errors. The L2 error norms for the solutions are 5.7% (7.5GHz) and 0.073% (1.5MHz).

Table 7.1: Performance of the vectorial LF-MLFMA with CIFE-RWG for a $2,436,960$-unknowns sphere

Level	**l=2**	**l=3**	**l=4**	**l=5**	**l=6**	**l=7**	**l=8**
7.5*GHz*							
Time	215s	117s	87s	65.3s	71.8s	136s	669s
Order P	78	42	24	14	9	7	7
Box size (λ)	12.63	6.32	3.16	1.58	0.79	0.39	0.20
1.5*MHz*							
Time	0.16s	0.61s	2.40s	9.31s	36.8s	135s	589s
Order P	7	7	7	7	7	7	7
Box size ($10^{-6} \cdot \lambda$)	2500	1250	625	313	156	78	39

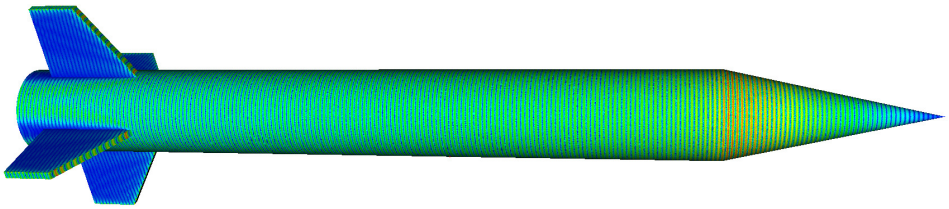

Figure 7.2: A snapshot of time-harmonic surface current density on 110λ long rocket computed using the proposed vectorial LF-MLFMA.

with 250 million non-zero elements. The EFIE and MFIE content in this CFIE simulation was 0.2 and 0.8, respectively. All simulations were carried out on a single core of a Intel Xeon 2.66GHz processor. The truncation orders were set for 2 digits of accuracy and one buffer box was used in the MLFMA tree.

7.5 Conclusion

In this paper, an extension to LF-MLFMA for efficient handling of the vectorial EFIE, MFIE, and CFIE kernels is presented. We show that the method can

be applied to targets of up to 110 wavelengths in size without combining it with HF-MLFMA. The method maintains the same memory requirement as scalar LF-MLFMA when evaluating the vectorial kernels. The CPU time is three to four times higher than for the scalar kernel depending on which EFIE formulation is being used.

References

[1] Andriulli, F.P., et.al., "A multiplicative Calderon preconditioner for the electric field integral equation," *IEEE Trans. Antennas Propag.,* vol. 56, no. 6, pp. 2398-2412, Aug. 2008.

[2] H. Cheng, et.al., "A wideband fast multipole method for the Helmholtz equation in three dimensions," *J. Comp. Phys.* vol. 216, no. 1, pp. 300-325, July 2006.

[3] N. A. Gumerov and R. Duraiswami, *Fast Multipole Methods for the Helmholtz Equation in Three Dimensions,* Elsevier, Amsterdam, 2006.

[4] L.J. Jiang and W.C. Chew "A mixed-form fast multipole algorithm," *IEEE Trans. Antennas Propag.,* vol. 53, no. 12, pp. 4145-4156, Dec. 2005.

[5] H. Wallen and J. Sarvas, "Translation procedures for broadband MLFMA," *Prog. In Electromagnetics Research,* vol. 55, pp. 47-78, 2005.

[6] I. Bogaert, et.al., "A nondirective plane wave MLFMA stable at low frequencies," *IEEE Trans. Antennas Propag.,* vol. 56, no 12; pp. 3752-3767, Dec. 2008.

[7] Z.G. Qian and W.C. Chew "Fast full-wave surface integral equation solver for multiscale structure modeling," *IEEE Trans. Antennas Propag.,* vol. 57, no. 11, pp. 3594-3601, Nov. 2009.

[8] W.C. Chew, et.al, *Fast and Efficient Algorithms in Computational Electromagnetics,* Artech House Publishers, 2000.

Chapter 8

Conclusions and Future Work

This chapter summarizes the results from the thesis and provides suggestions for future work.

8.1 Conclusions

In Chapter 3, we extended the free-space center-of-charge approximation to inhomogeneous stratified media. The new center-of-charge was shown to be easily computable from knowledge of the charge distribution in the layered media. When computed appropriately, the multilayered center-of-charge was shown to exhibit the desired absolute $O(1/R^3)$ and relative $O(1/R^2)$ error behavior, where R is the distance from a box of charges. Hierarchical clustering of the multilayer center-of-charge was shown to behave analogously to free-space hierarchical clustering. Finally, we demonstrated the proposed Barnes-Hut acceleration scheme for fast capacitance extraction.

In Chapter 5, we presented a new tree-based algorithm for the Helmholtz kernel by introducing the center-of-radiation approximation in analogy to the center-of-charge in Chapter 3. The center-of-radiation was derived by matching the field spectrum of the true sources in the vicinity of the stationary

phase point. We obtained a computationally efficient expression for finding the magnitude and location of the center-of-radiation and showed that the center-of-radiation can be applied hierarchically. The error behavior was studied and compared to LF-FMM and HF-FMM and shown to be valid in the quasi-static regime.

In Chapter 7, we proposed an extension of LF-FMM that is efficient for handling the vectorial EFIE, MFIE, and CFIE kernels. We showed that the new method maintains the same memory requirement as scalar LF-FMM when evaluating the vectorial kernels. The method was demonstrated for computational domains up to 110 wavelengths in size without combining it with HF-FMM.

8.2 Suggestions of Future Work

- Explore the extension of the center-of-charge and center-of-radiation to higher order approximations. Following the methodology shown in this thesis, we may find higher-order approximations by matching higher order moments at the stationary phase point of the field spectrum. Higher order field approximations may be generated by, for example, introducing multiple center-of-charge sources. Another direction would be to add dipole and quadrupole moments to the approximation.

- Investigate the hybridization of the center-of-radiation with the spherical wave basis functions that were presented in Chapter 7. For example, the center-of-radiation may be more efficient at box sizes that are much smaller than a wavelength where interpolation may not be required or can be simplified. However, spherical basis functions may be more efficient at the top levels as they do not require to be interpolated. Another hybridization approach would use spherical wave basis functions and let

its expansion center vary with the source distribution in a similar fashion to the center-of-radiation.

- Extend the center-of-radiation approximation to inhomogeneous stratified media. It may be possible to find an approximation by matching the spectral moments according to the procedure outlined in Chapters 3 and 5.

- Rather than computing the location of center-of-radiation, we can introduce a fixed grid of radiating sources at each box in the BH tree data structure and match the spectrum with (uniformly or non-uniformly sampled) Fourier harmonics. In particular, this may be useful for high-order approximations or for inhomogeneous media where the non-linearity makes it difficult to find the analytic location of the center-of-radiation.

- The center-of-radiation approximation breaks down beyond the quasi-static regime because the underlaying approximation in the spectral domain becomes inaccurate at higher frequencies. It may be possible to derive the center-of-radiation by using another type of approximation which does not suffer from the same problem. One direction may be to look at the phase center concept from antenna theory which is a single source approximation that valid at high frequencies.

- Investigate and optimize LF-FMM for truly multi-scale geometries. Previous work has been focused on accelerating multi-scale point-based distributions. When non-point based basis functions are used, such as the RWG basis, additional constraints are introduced based on the geometrical size for each basis function. As such, the distance at which the source and observation basis are well-separated is dependent on the properties of both the source and observation patches. The BH algorithm's adaptive nature is ideal for handing such interactions whereas FMM requires that all interactions are govern by the same separation criteria.

- Explore ways to improve the complexity of the translation procedure in LF-FMM from the $O(P^3)$ complexity to $O(P^2)$ or $O(P^2 logP)$. One approach may be to use high-frequency asymptotic when P is large.

- Explore parallelization strategies for LF-FMM which are efficient for both low and high frequencies. At high frequencies[1], the workload in LF-FMM remains approximately constant at each level of the tree. Previous work on parallelization strategies for multipole based expansions have been limited to spatial partitioning strategies where each box is assigned to a single processor. In order to sustain good load balancing at all levels, one approach would be to partition the expansions across multiple processors. Similar parallelization strategies have been presented for HF-FMM, however, those methods are not directly applicable to LF-FMM.

[1]Scatters of up to 110 wavelengths in size

APPENDIX

Appendix A

Extended Error Analysis for the Multilayered Center-of-Charge Approximation

In this appendix, we perform additional error analysis of the multilayered center-of-charge presented in Chapter 3. Specifically, the error will be studied in the L2 error norm instead of using the average relative error that was utilized in the early chapter. In addition, we will analyze the level-dependant error when the center-of-charge approximation is computed hierarchically with a Barnes-Hut tree. Reusing the notations from Chapter 3, we modify Equation (3.59) to work in the L2 sense as

$$\delta^2(R) = \frac{\int_0^{2\pi}\int_0^{\pi} |\Phi(\boldsymbol{r}(R,\theta,\phi)) - \Psi(\boldsymbol{r}(R,\theta,\phi), \boldsymbol{r}_\Sigma)|^2 \sin\theta d\theta d\phi}{\int_0^{2\pi}\int_0^{\pi} |\Phi(\boldsymbol{r}(R,\theta,\phi))|^2 \sin\theta d\theta d\phi} \tag{A.1}$$

The next set of experiments will utilize this equation.

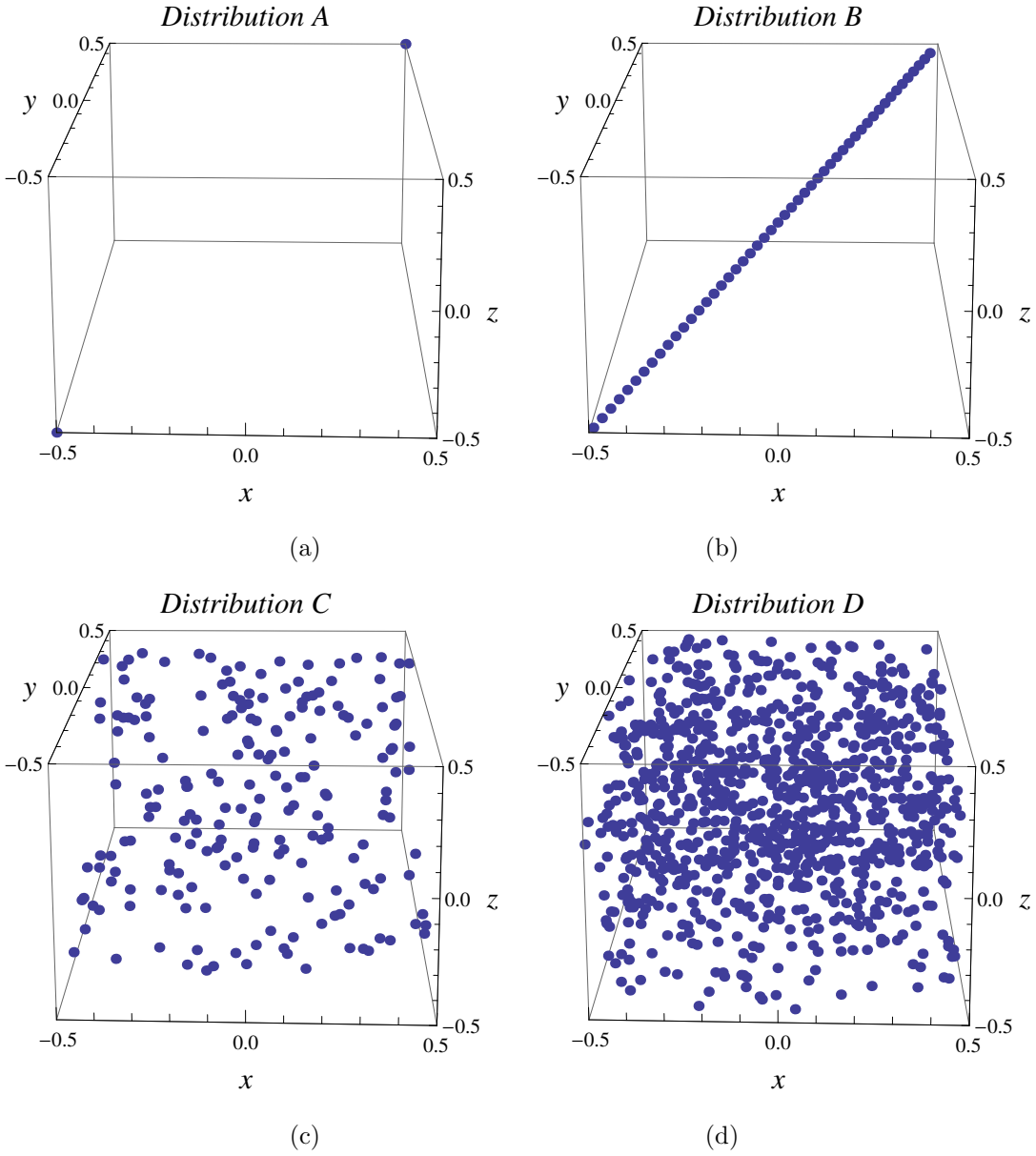

Figure A.1: Distributions of charges contained in a cube with a width of $1m$. The four distributions are two charges in opposite corners (a), 50 charges along a line (b), 200 randomly distributed charges on the surface of a plane, and 1000 randomly distributed charges throughout the volume of the box (d).

A.1 Numerical Study of the L2-Error Behavior

For the purpose of our numerical study, we consider the four distributions of charges as visualized in Figure A.1 and implemented as

- **Distribution A**: Two charges situated at opposite corners of the box, both with a charge of 1 Coulomb. This represents a worst-case configuration for the center-of-charge approximation.
- **Distribution B:** 50 charges are uniformly distributed along a line that intersects two opposite corners of the box. Each charge carries a random charge between 0 and 1 Coulomb[1].
- **Distribution C:** 200 charges are randomly distributed on the surface of a plane. Each charge carries a random charge between 0 and 1 Coulomb.
- **Distribution D:** 1000 charges are randomly distribution inside the box. Each charge carries a random charge between 0 and 1 Coulomb.

In addition to the charge distributions, we also consider three types of background media defined below according to the notation in Figure 3.1.

- **Free-space:** Vacuum with relative permittivity $\epsilon_0 = 1$.
- **Half-space:** Two layers with relative permittivities $\epsilon_0 = 2$ and $\epsilon_1 = 4$ and the dielectric interface located at $a_0 = 0m$.
- **Multilayered:** Five layers with relative permittivites ϵ_0 thru ϵ_4 equal to 2, 10, 4, 7, and 2, respectively, and the dielectric interface locations a_0 thru a_3 equal to $-0.3m$, $0m$, $0.3m$, and $0.4m$.

[1]The center-of-charge approximation requires that all charges have the same sign. When applied to a distribution of both positive and negative charges, we would introduce two center-of-charge approximations for each box.

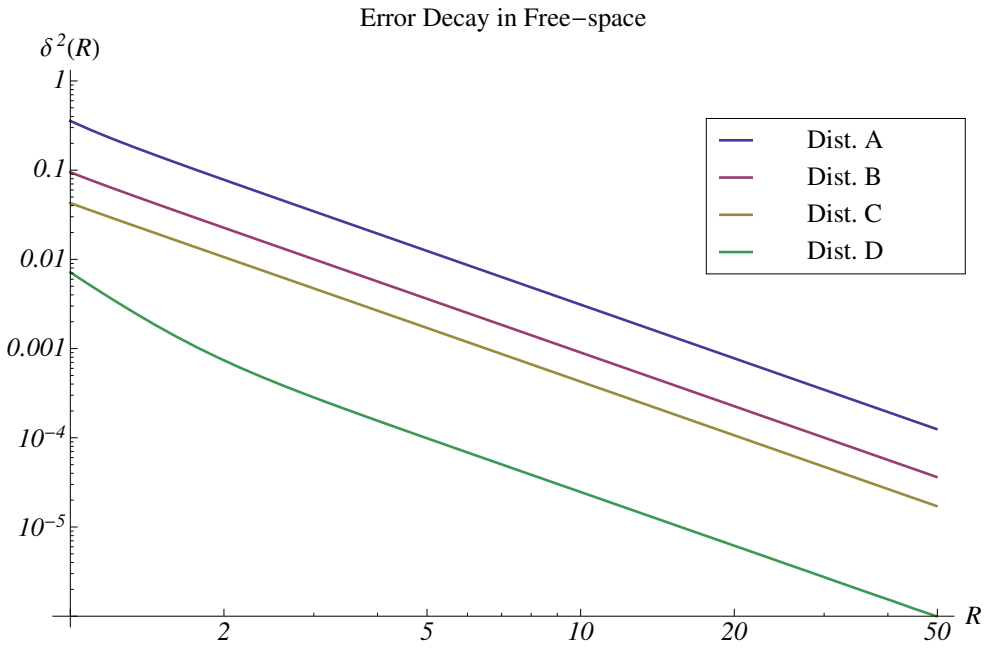

Figure A.2: Plot of $\delta^2(R)$ (A.1) as a function of observation distance R for the four charge distributions situated in free-space.

Plots A.2, A.3, and A.4 show the error behavior for each combination of the charge distributions and background media. We present these results to give the reader of this thesis additional insight in how the error decays when the L2-norm is used and also to demonstrate how various distributions of sources and layers impact the error. Finally, we note that if these results are used to implement error bounds, then the results for *distribution A* should be used since it represents the worst-case configuration.

A.2 Error in Hierarchical Clustering

In order to study the error in the hierarchical clustering when the center-of-charge approximation used in conjunction with the Barnes-Hut algorithm, we consider the charge *distribution D* situated in the 5-layered dielectric media

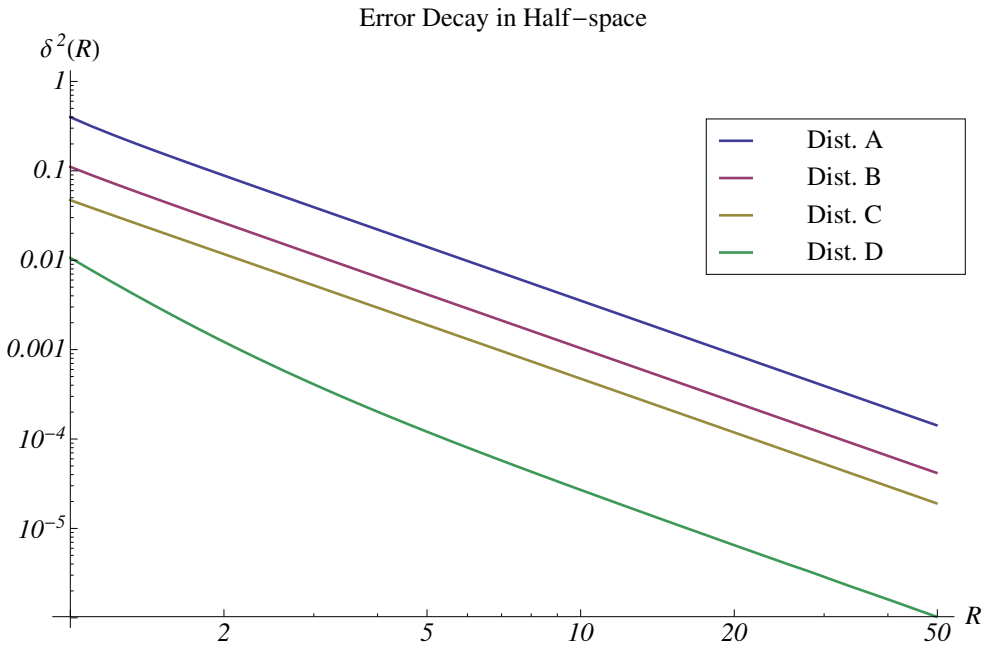

Figure A.3: Plot of $\delta^2(R)$ (A.1) as a function of observation distance R for the four charge distributions situated in half-space.

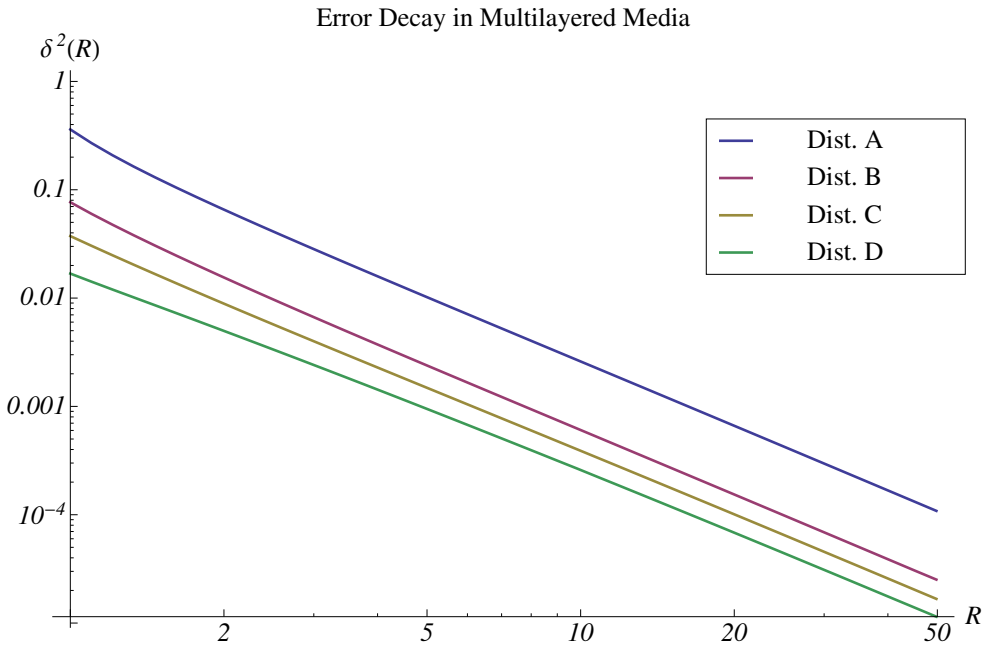

Figure A.4: Plot of $\delta^2(R)$ (A.1) as a function of observation distance R for the four charge distributions situated in a 5-layered dielectric media.

outlined in the previous section. In our first experiment, we compute the center-of-charge approximation for the box without clustering which is equivalent to a Barnes-Hut tree with a single level. This result is shown in Table A.1. For our next experiment, we build four Barnes-Hut trees that are 2 thru 5 levels deep and evaluate the center-of-charge for the root box hierarchically by traversing the tree bottom up while computing the center-of-charge approximations at each box in the tree. The results for each Barnes-Hut tree is summarized in Table A.1. These results clearly show that the hierarchical clustering does not introduce any noticeable error because the locations and magnitudes obtained by using hierarchical clustering match the directly computed approximation within the precision of computer arithmetics.

Number of levels in tree	Center-of-Charge	
	Location	Magnitude
1	x = -0.0182947850491114 y = -0.0019920112273499 z = 0.0402527052492543	520.5786350116038648
2	x = -0.0182947850491114 y = -0.0019920112273499 z = 0.0402527052492535	520.5786350116038647
3	x = -0.0182947850491114 y = -0.0019920112273499 z = 0.0402527052492531	520.5786350116038647
4	x = -0.0182947850491114 y = -0.0019920112273499 z = 0.0402527052492532	520.5786350116038647
5	x = -0.0182947850491114 y = -0.0019920112273499 z = 0.0402527052492531	520.5786350116038647

Table A.1: Center-of-charge computed hierarchically with a Barnes-Hut tree with the number of levels varying from 1 to 5.

Appendix B

Complexity Analysis of the Vectorial Low-Frequency MLFMA

This appendix provides a complexity analysis for the Vectorial Low-Frequency MLFMA that was presented in Chapter 7 of this thesis.

B.1 Relationship between Truncation Order and Level in the MLFMA Tree

The truncation order, P, in (7.5) and (7.7) are determined by the electrical size of Sphere S that enclosed all sources in a particular box and the desired accuracy ϵ. Denote the electrical size of Sphere S with kd where k is the wavenumber and d is the diameter of the sphere. The truncation order P_ℓ at level ℓ of the MLFMA tree can be represented as

$$P_\ell = \alpha k d_\ell + \beta + \gamma \log \epsilon \tag{B.1}$$

where d_ℓ is the diameter of the smallest sphere that enclose a single box at level ℓ and α, β, and γ are constants. A more detailed analysis of the truncation

Object	Integral equation	Number of boxes at level ℓ	kD	P_ℓ
Smooth	SIE	4^ℓ	$N^{1/2}$	$N^{1/2}2^{-\ell}$
Smooth	VIE	8^ℓ	$N^{1/3}$	$N^{1/3}2^{-\ell}$
Complex	SIE	4^ℓ	1	1
Complex	VIE	8^ℓ	1	1

Table B.1: Asymptotic relationship between MLFMA and solution parameters.

order can be found in [GD05]. Let us assume that we apply MLFMA to a scatterer that can be enclosed in a sphere of diameter D. The level-dependent size can then be expressed as

$$d_\ell = \frac{D}{2^\ell} \tag{B.2}$$

which leads to

$$P_\ell = \alpha \frac{kD}{2^\ell} + \beta \tag{B.3}$$

where we have absorbed $\gamma \log \epsilon$ into β under the assumption that the requested accuracy remains constant through out the computations. Asymptotically, we write the truncation number as

$$P_\ell = \begin{array}{ll} \alpha \frac{kD}{2^\ell}, & \text{if} \quad kD \gg \kappa \\ \beta, & \text{if} \quad kD \ll \kappa \end{array} \tag{B.4}$$

where κ can be assumed to be on the order of one wavelength.

B.2 Relationship between Electrical Size and Number of Unknowns

The solution of integral equations normally require that the scatterer under investigation is discretized by a minimum number of basis functions per wavelength. For the purpose of this complexity analysis we consider two scenarios

Translation method	Operations
Direct computation	$O(P^5)$
Recurrence scheme	$O(P^4)$
Point-and-shoot	$O(P^3)$
Rokhlin translator	$O(P^2 logP)$
High-frequency asymptotic [GD05]	$O(P^2 logP)$

Table B.2: Complexity of MLFMA translation algorithms.

- **Smooth Object:** The number of basis functions per wavelength remains constant everywhere. This is a typical scenario for modelling objects at high frequencies.

- **Complex Object:** The number of basis functions depends only on the geometric complexity of the object. This is a typical scenario for modelling of electrically small, but highly complex objects.

Based on these scenarios we can express the level-dependant MLFMA parameters as shown in Table B.1 for the Surface Integral Equation (SIE) and the Volume Integral Equation (VIE), both discretized with N basis functions.

B.3 Complexity of Translation

The cost of performing a translation between two expansion centers of order P is $O(P^\nu \log^\xi P)$, where ν and ξ constants that depend on the algorithm used. An overview of available translation algorithms in presented in Section 1.2.3 of this thesis and their complexities are summarized in Table B.2.

B.4 Complexity Analysis of MLFMA

For simplicity, we will begin by analyzing the complexity of the surface integral equation formulation for the smooth geometry case. The same procedure can be applied to the other scenarios and those results are summarized in Table B.3. According to the division of MLFMA described Section 1.2.1 of this thesis, we perform the complexity analysis for the each phase below.

- **Data Structures:** The creation of the data structures requires $O(NlogN)$ operations due to the fact that we need to sort the spatial locations of the basis functions into an ordering that matches the structure of the tree. The data structure can be stored in $O(N)$ memory. However, we normally store the expansion coefficients at each box of the tree in memory. Since each box at level ℓ has $P_\ell^2 - 1$ coefficients, the overall memory required is $\sum_{\ell=1}^{\log N} 4^\ell P_\ell^2 = \sum_{\ell=1}^{\log N} 4^\ell (N^{1/2}2^{-\ell})^2 = \sum_{\ell=1}^{\log N} N = O(NlogN)$.

- **Leaf-Node Aggregation:** P is constant at the leaf-level and aggregating N basis functions requires $O(N)$ operations.

- **Aggregation:** The aggregation at level ℓ requires $4^\ell P_\ell^\nu \log^\xi P_\ell$ operations. Substituting $P_\ell = N^{1/2}2^{-\ell}$ and using that $\ell \leq \log N$ and $P_\ell \geq 1$ we can write $4^\ell P_\ell^\nu \log^\xi P_\ell = 4^\ell (N^{1/2}2^{-\ell})^\nu \log^\xi N^{1/2}2^{-\ell} =$ $O(4^\ell (N^{1/2}2^{-\ell})^\nu \log^\xi N)$. Accordingly, the total number of operations for the aggregation is $\sum_{\ell=1}^{\log N} 4^\ell (N^{1/2}2^{-\ell})^\nu \log^\xi N) = O(N^{\nu/2} \log^{1+\xi} N)$ if $\nu = 2$ or $O(N^{\nu/2} \log^\xi N)$ if $\nu > 2$

- **Translation:** Same as aggregation.

- **Disaggregation** Same as aggregation.

- **Leaf-Node Disaggregation:** Same as leaf-node aggregation. Note that the additional step proposed in Chapter 7 of converting the magnetic vector potential to electric and magnetic field is carried out in constant

Translation	Smooth Object		Complex Object	
complexity	SIE	VIE	SIE	VIE
$O(P^5)$	$O(N^{2.5})$	$O(N^{1.67})$	$O(N \log N)$	$O(N \log N)$
$O(P^4)$	$O(N^2)$	$O(N^{1.33})$	$O(N \log N)$	$O(N \log N)$
$O(P^3)$	$O(N^{1.5})$	$O(N \log N)$	$O(N \log N)$	$O(N \log N)$
$O(P^2 logP)$	$O(N \log^2 N)$	$O(N \log N)$	$O(N \log N)$	$O(N \log N)$

Table B.3: Complexities for the overall MLFMA for different translation algorithms, scatterers, and integral equations.

time for each box and therefore does not impact the complexity of this phase.

- **Near Field Summation:** Since we assume that each box contains a constant number of basis functions, the number of operations per box is also constant. The complexity for this phase is therefore $O(N)$.

As shown in Table B.3, the complexity of MLFMA is $O(N \log N)$ for electrically small objects regardless of the complexity of the translation method used. On the other hand, in order to effectively model smooth objects at high frequencies we require a $O(P^2 \log P)$ translation method for surface integral equation formulations and no worse than $O(P^3)$ for volume integral equation formulations. The implementation that we used for the numerical results in Chapter 7 was utilizing $O(P^3)$ translation and even though it is asymtopically $O(N^{1.5})$ for surface scatterers, it performed similar to $O(N \log N)$ implementation for a 110 wavelength scatterer. The reason for this behavior is that the predicted $O(N^{1.5})$ complexity is an asymptotics and at 110 wavelengths we were still close enough to the region where the method operate at $O(N \log N)$ complexity. Finally, we note that in a practical implementation, we would switch to either the High-Frequency MLFMA or to a $O(P^2 \log P)$ translation method as soon as they become numerically stable.

Bibliography

[ACB+08] F.P. Andriulli, K. Cools, H. Bagci, F. Olyslager, A. Buffa, S. Christiansen, and E. Michielssen. A multiplicative calderon preconditioner for the electric field integral equation. *Antennas and Propagation, IEEE Transactions on*, 56(8):2398–2412, 2008.

[AL08] Cheol-O Ahn and Sang Hwan Lee. A new treecode for long-range force calculation. *Computer Physics Communications*, 178(2):121 – 127, 2008.

[App85] Andrew W. Appel. An efficient program for many-body simulation. *SIAM Journal on Scientific and Statistical Computing*, 6(1):85–103, January 1985.

[AS64] Milton Abramowitz and Irene A. Stegun. *Handbook of Mathematical Functions with Formulas, Graphs, and Mathematical Tables*. Dover Publications, New York, 1964.

[BAD01] U. Becciani and V. Antonuccio-Delogu. Are you ready to fly in the universe? a multi-platform N-body tree code for parallel supercomputers. *Computer Physics Communications*, 136(1–2):54 – 63, 2001.

[BBJ94] E. Bleszynski, M. Bleszynski, and T. Jaroszewicz. A fast integral-equation solver for electromagnetic scattering problems. *An-*

tennas and Propagation Society International Symposium, 1994. AP-S. Digest, 1:416–419 vol.1, Jun 1994.

[BCPB90] W. Benz, A. G. W. Cameron, W. H. Press, and R. L. Bowers. Dynamic mass exchange in doubly degenerate binaries. I - 0.9 and 1.2 solar mass stars. *Astrophysical Journal, Part 1*, 348:647–667, Jan 1990.

[BGPZ12] Jeroen Bédorf, Evghenii Gaburov, and Simon Portegies Zwart. A sparse octree gravitational N-body code that runs entirely on the gpu processor. *J. Comput. Phys.*, 231(7):2825–2839, April 2012.

[BGS91] O. M. Bucci, C. Gennarelli, and C. Savarese. Optimal interpolation of radiated fields over a sphere. *IEEE Trans. Antennas Propag.*, 39:1633, 1991.

[BH86] J. Barnes and P. Hut. A hierarchical $o(nlogn)$ force-calculation algorithm. *Nature*, 324:446–449, December 1986.

[BH89] Joshua E. Barnes and Piet Hut. Error analysis of a tree code. *Astrophysical Journal Supplement Series*, 70:389–417, 1989.

[BO09a] Ignace Bogaert and Femke Olyslager. A low frequency stable plane wave addition theorem. *Journal of Computational Physics*, 228(4):1000 – 1016, 2009.

[BO09b] Ignace Bogaert and Femke Olyslager. New plane wave addition theorems. In *AIP Conf. Proc.*, volume 1106, pages 46–55. American Institute of Physics, 2009.

[Bou88] Lars Bouchet, Francois R.; Hernquist. Cosmological simulations using the hierarchical tree method. *Astrophysical Journal Supplement Series*, 68:521–538, 1988.

[BPO08] I. Bogaert, J. Peeters, and F. Olyslager. A nondirective plane wave MLFMA stable at low frequencies. *Antennas and Propagation, IEEE Transactions on*, 56(12):3752 –3767, dec. 2008.

[BPZ11] I. Bogaert, J. Peeters, and D. De Zutter. Error control of the vectorial nondirective stable plane wave multilevel fast multipole algorithm. *Progress In Electromagnetics Research*, 111:271–290, 2011.

[BWS+95] Ranganathan Bharadwaj, Andreas Windemuth, S. Sridharan, Barry Honig, and Anthony Nicholls. The fast multipole boundary element method for molecular electrostatics: An optimal approach for large systems. *Journal of Computational Chemistry*, 16(7):898–913, 1995.

[CAO10] M. Cwikla, J. Aronsson, and V. Okhmatovski. Low-frequency MLFMA on graphics processors. *Antennas and Wireless Propagation Letters, IEEE*, 9:8 –11, 2010.

[CB85] P. E. Cottrell and E. M. Buturla. Vlsi wiring capacitance. *IBM J. Res. Dev.*, 29(3):277–288, May 1985.

[CCG+06] Hongwei Cheng, William Y. Crutchfield, Zydrunas Gimbutas, Leslie F. Greengard, J. Frank Ethridge, Jingfang Huang, Vladimir Rokhlin, Norman Yarvin, and Junsheng Zhao. A wideband fast multipole method for the helmholtz equation in three dimensions. *Journal of Computational Physics*, 216(1):300 – 325, 2006.

[Che88] W.C. Chew. A quick way to approximate a Sommerfeld-Weyl-type integral [antenna far-field radiation]. *Antennas and Propagation, IEEE Transactions on*, 36(11):1654–1657, Nov 1988.

[Che07] W.C. Chew. Diagonalization of the vector addition theorem. In *Antennas and Propagation Society International Symposium, 2007 IEEE*, pages 3440 –3443, june 2007.

[Che08] W. C. Chew. Vector addition theorem and its diagonalization. *Commun. Comput. Phys.*, 3(2), 2008.

[CJMS01] W. C. Chew, J.-M. Jin, E. Michielssen, and J. Song. *Fast and Efficient Algorithms in Computational Electromagnetics*. Artech House, 2001.

[CRW93] Ronald Coifman, Vladimir Rokhlin, and Stephen Wandzura. Fast multiple method for the wave equation: a pedestrian prescription. *IEEE Antennas and Propagation Magazine*, 35(3):7–12, 1993. cited By (since 1996) 661.

[CTH08] Weng Cho Chew, Mei Song Tong, and Bin Hu. Integral equation methods for electromagnetic and elastic waves. *Synthesis Lectures on Computational Electromagnetics*, 3(1):1–241, 2008.

[CWD08] Roger Cocle, Grégoire Winckelmans, and Goéric Daeninck. Combining the vortex-in-cell and parallel fast multipole methods for efficient domain decomposition simulations. *J. Comput. Phys.*, 227(4):2263–2292, February 2008.

[Dar00a] Eric Darve. The fast multipole method I: Error analysis and asymptotic complexity. *SIAM J. Numer. Anal.*, 38(1):98–128, June 2000.

[Dar00b] Eric Darve. The fast multipole method: Numerical implementation. *Journal of Computational Physics*, 160(1):195 – 240, 2000.

[DH04] Eric Darve and Pascal Havé. Efficient fast multipole method for low-frequency scattering. *Journal of Computational Physics*, 197(1):341 – 363, 2004.

[DJV+01] K.C. Donepudi, Jian-Ming Jin, S. Velamparambil, J. Song, and Weng Cho Chew. A higher order parallelized multilevel fast multipole algorithm for 3-D scattering. *Antennas and Propagation, IEEE Transactions on*, 49(7):1069 –1078, jul 2001.

[DKG92] Hong-Qiang Ding, Naoki Karasawa, and William A. Goddard III. The reduced cell multipole method for coulomb interactions in periodic systems with million-atom unit cells. *Chemical Physics Letters*, 196(1–2):6 – 10, 1992.

[DS09] T. Dufva and J. Sarvas. Broadband MLFMA with plane wave expansions and optimal memory demand. *Antennas and Propagation, IEEE Transactions on*, 57(3):742 –753, march 2009.

[Dub96] John Dubinski. A parallel tree code. *New Astronomy*, 1(2):133 – 147, 1996.

[ED95] Michael A. Epton and Benjamin Dembart. Multipole translation theory for the three-dimensional laplace and helmholtz equations. *SIAM J. Sci. Comput.*, 16(4):865–897, July 1995.

[EG06a] O. Ergul and L. Gurel. Enhancing the accuracy of the interpolations and anterpolations in MLFMA. *Antennas and Wireless Propagation Letters, IEEE*, 5(1):467 –470, dec. 2006.

[EG06b] O. Ergul and L. Gurel. Optimal interpolation of translation operator in multilevel fast multipole algorithm. *Antennas and Propagation, IEEE Transactions on*, 54(12):3822 –3826, dec. 2006.

[EG09] O. Ergul and L. Gurel. A hierarchical partitioning strategy for an efficient parallelization of the multilevel fast multipole algorithm. *Antennas and Propagation, IEEE Transactions on*, 57(6):1740 – 1750, june 2009.

[EG11] O. Ergul and L. Gurel. Rigorous solutions of electromagnetic problems involving hundreds of millions of unknowns. *Antennas and Propagation Magazine, IEEE*, 53(1):18 –27, feb. 2011.

[EMRV92] N. Engheta, W.D. Murphy, V. Rokhlin, and M.S. Vassiliou. The fast multipole method (FMM) for electromagnetic scattering problems. *Antennas and Propagation, IEEE Transactions on*, 40(6):634 –641, jun 1992.

[ESM98] A.Arif Ergin, Balasubramaniam Shanker, and Eric Michielssen. Fast evaluation of three-dimensional transient wave fields using diagonal translation operators. *Journal of Computational Physics*, 146(1):157 – 180, 1998.

[ESM99] A.A. Ergin, B. Shanker, and E. Michielssen. The plane-wave time-domain algorithm for the fast analysis of transient wave phenomena. *Antennas and Propagation Magazine, IEEE*, 41(4):39 –52, sep 1999.

[EvdBG09] O. Ergul, I. van den Bosch, and L. Gurel. Two-step lagrange interpolation method for the multilevel fast multipole algorithm. *Antennas and Wireless Propagation Letters, IEEE*, 8:69 –71, 2009.

[Ewa21] P. Ewald. Die berechnung optischer und elektrostatischer gitterpotentiale. *Ann. Phys.*, 369:253–287, 1921.

[FO08a] J. Fostier and F. Olyslager. An asynchronous parallel MLFMA for scattering at multiple dielectric objects. *Antennas and Propagation, IEEE Transactions on*, 56(8):2346 –2355, aug. 2008.

[FO08b] J. Fostier and F. Olyslager. Provably scalable parallel multilevel fast multipole algorithm. *Electronics Letters*, 44(19):1111 –1113, 11 2008.

[GD05] N. A. Gumerov and R. Duraiswami. *Fast Multipole Methods for the Helmholtz Equation in Three Dimensions*. Elsevier, 2005.

[GD09] N. A. Gumerov and R. Duraiswami. A broadband fast multipole accelerated boundary element method for the three dimensional Helmholtz equation. *Acoustical Society of America Journal*, 125:191, 2009.

[GG09] Z. Gimbutas and L. Greengard. Short note: A fast and stable method for rotating spherical harmonic expansions. *J. Comput. Phys.*, 228(16):5621–5627, September 2009.

[GGM93] A. Greenbaum, L. Greengard, and G.B. McFadden. Laplace's equation and the dirichlet-neumann map in multiply connected domains. *Journal of Computational Physics*, 105(2):267 – 278, 1993.

[GH02] Leslie F. Greengard and Jingfang Huang. A new version of the fast multipole method for screened coulomb interactions in three dimensions. *Journal of Computational Physics*, 180(2):642 – 658, 2002.

[GHRW98] L. Greengard, Jingfang Huang, V. Rokhlin, and S. Wandzura. Accelerating fast multipole methods for the Helmholtz equation at low frequencies. *Computational Science Engineering, IEEE*, 5(3):32 –38, jul-sep 1998.

[Gib07] W.C. Gibson. *The Method of Moments in Electromagnetics*. Taylor & Francis, 2007.

[GJ04] Dipanjan Gope and Vikram Jandhyala. Pilot: A fast algorithm for enhanced 3d parasitic capacitance extraction efficiency. *Microwave and Optical Technology Letters*, 41(3):169–173, 2004.

[GR87] L. Greengard and V. Rokhlin. A fast algorithm for particle simulations. *J. Comput. Phys.*, 73(2):325–348, 1987.

[GR88] L. Greengard and V. Rokhlin. The rapid evaluation of potential fields in three dimensions. In *Vortex Methods*, Lecture Notes in Mathematics, pages 121–141. Springer Berlin / Heidelberg, 1988.

[HAS02] B. Hariharan, S. Aluru, and B. Shanker. A scalable parallel fast multipole method for analysis of scattering from perfect electrically conducting surfaces. In *Proceedings of the 2002 ACM/IEEE conference on Supercomputing*, page 42, nov. 2002.

[HB87] W.D. Hillis and J. Barnes. Programming a highly parallel computer. *Nature*, 326, May 1987.

[HBS91] Lars Hernquist, Francois R. Bouchet, and Yasushi Suto. Application of the ewald method to cosmological N-body simulations. *Astrophysical Journal Supplement Series*, 75:231–240, 1991.

[HNY+09] Tsuyoshi Hamada, Tetsu Narumi, Rio Yokota, Kenji Yasuoka, Keigo Nitadori, and Makoto Taiji. 42 TFlops hierarchical N-body simulations on GPUs with applications in both astrophysics and turbulence. In *Proceedings of the 2009 ACM/IEEE conference on Supercomputing*, pages 1–12, 2009.

[HOC03] Michael Larkin Hastriter, Shinichiro Ohnuki, and Weng Cho Chew. Error control of the translation operator in 3D MLFMA. *Microwave and Optical Technology Letters*, 37(3):184–188, 2003.

[HS08] I. Hanninen and J. Sarvas. Efficient evaluation of the rokhlin translator in multilevel fast multipole algorithm. *Antennas and Propagation, IEEE Transactions on*, 56(8):2356 –2362, aug. 2008.

[IMES90] Tomoyoshi Ito, Junichiro Makino, Toshikazu Ebisuzaki, and Daiichiro Sugimoto. A special-purpose N-body machine GRAPE-1. *Computer Physics Communications*, 60(2):187 – 194, 1990.

[JC04] L.J. Jiang and W.C. Chew. Low-frequency fast inhomogeneous plane-wave algorithm (LF-FIPWA). *Microwave and Optical Technology Letters*, 40(2):117–122, 2004.

[JC05] Li Jun Jiang and Weng Cho Chew. A mixed-form fast multipole algorithm. *Antennas and Propagation, IEEE Transactions on*, 53(12):4145 – 4156, dec. 2005.

[JCJ+92] John A. Board Jr., Jeffrey W. Causey, James F. Leathrum Jr., Andreas Windemuth, and Klaus Schulten. Accelerated molecular dynamics simulation with the parallel fast multipole algorithm. *Chemical Physics Letters*, 198(1–2):89 – 94, 1992.

[Jia04] Lijun Jiang. *Studies on low frequency fast multipole algorithms*. PhD thesis, University of Illinois at Urbana-Champaign, 2004.

[JMM95] V Jandhyala, E Michielssen, and R Mittra. Multipole-accelerated capacitance computation for 3-d structures in a stratified dielectric medium using a closed form green's function. *Int. J. Microwave and Millimeter-Wave Computer-Aided Eng*, (5):68–78, 1995.

[JMM96] Vikram Jandhyala, Eric Michielssen, and Raj Mittra. A memory-efficient, adaptive algorithm for multipole-accelerated capacitance computation in a stratified dielectric medium. *International Journal of Microwave and Millimeter-Wave Computer-Aided Engineering*, 6(6):381–390, 1996.

[JP89] J. Garrett Jernigan and David H. Porter. A tree code with logarithmic reduction of force terms, hierarchical regularization of all

variables, and explicit accuracy controls. *Astrophysical Journal Supplement Series*, 71:871–893, 1989.

[KFM99] A. Kawai, T. Fukushige, and J. Makino. $7.0/Mflops astrophysical N-body simulation with treecode on GRAPE-5. In *Proceedings of the 1999 ACM/IEEE conference on Supercomputing*, page 67, nov. 1999.

[KL97] Sharad Kapur and David E. Long. Ies3: a fast integral equation solver for efficient 3-dimensional extraction. In *ICCAD '97: Proceedings of the 1997 IEEE/ACM international conference on Computer-aided design*, pages 448–455, Washington, DC, USA, 1997. IEEE Computer Society.

[KP05a] Jakub Kurzak and B. Montgomery Pettitt. Communications overlapping in fast multipole particle dynamics methods. *Journal of Computational Physics*, 203(2):731 – 743, 2005.

[KP05b] Jakub Kurzak and B. Montgomery Pettitt. Massively parallel implementation of a fast multipole method for distributed memory machines. *Journal of Parallel and Distributed Computing*, 65(7):870 – 881, 2005.

[KSC99] S. Koc, Jiming Song, and W. C. Chew. Error analysis for the numerical evaluation of the diagonal forms of the scalar spherical addition theorem. *SIAM J. Numer. Anal.*, 36(3):906–921, March 1999.

[LC10] Y. G. Liu and W. C. Chew. A low frequency vector fast multipole algorithm with vector addition theorem. *Communications in Computational Physics*, 8(5):1183–1207, 2010.

[LCJQ12] Yang G. Liu, Weng Cho Chew, Lijun Jiang, and Zhiguo Qian. A memory saving fast A-EFIE solver for modeling low-frequency

large-scale problems. *Appl. Numer. Math.*, 62(6):682–698, June 2012.

[LK01] Keith Lindsay and Robert Krasny. A particle method and adaptive treecode for vortex sheet motion in three-dimensional flow. *Journal of Computational Physics*, 172(2):879 – 907, 2001.

[LLB03] Jin-Fa Lee, J. F Lee, and R.J. Burkholder. Loop star basis functions and a robust preconditioner for efie scattering problems. *Antennas and Propagation, IEEE Transactions on*, 51(8):1855–1863, 2003.

[Mak90] Junichiro Makino. Vectorization of a treecode. *Journal of Computational Physics*, 87(1):148 – 160, 1990.

[MG05] Youssef M. Marzouk and Ahmed F. Ghoniem. K-means clustering for optimal partitioning and dynamic load balancing of parallel hierarchical N-body simulations. *J. Comput. Phys.*, 207(2):493–528, August 2005.

[MH89] Junichiro Makino and Piet Hut. Gravitational N-body algorithms: A comparison between supercomputers and a highly parallel computer. *Computer Physics Reports*, 9(4):199 – 246, 1989.

[MTES94] J. Makino, M. Taiji, T. Ebisuzaki, and D. Sugimoto. GRAPE 4: a one-Tflops special-purpose computer for astrophysical N-body problem. In *Proceedings of the 1994 ACM/IEEE conference on Supercomputing*, pages 429 –438, nov 1994.

[Nil04] Martin Nilsson. Stability of the high frequency fast multipole method for Helmholtz equation in three dimensions. *BIT Numerical Mathematics*, 44:773–791, 2004. 10.1007/s10543-004-4412-8.

[NVI13] NVIDIA. Kepler gk110, 2013.

[NW91] K. Nabors and J. White. FastCap: a multipole accelerated 3-D capacitance extraction program. *Computer-Aided Design of Integrated Circuits and Systems, IEEE Transactions on*, 10(11):1447–1459, Nov 1991.

[OC01] S. Ohnuki and Weng Cho Chew. A study of the error controllability of MLFMA. In *Antennas and Propagation Society International Symposium, 2001. IEEE*, volume 3, pages 774 –777, 2001.

[OC03a] S. Ohnuki and Weng Cho Chew. Numerical accuracy of multipole expansion for 2D MLFMA. *Antennas and Propagation, IEEE Transactions on*, 51(8):1883 – 1890, aug. 2003.

[OC03b] Shinichiro Ohnuki and Weng Cho Chew. Numerical analysis of local interpolation error for 2D-MLFMA. *Microwave and Optical Technology Letters*, 36(1):8–12, 2003.

[OSVW99] J.J. Ottusch, M.A. Stalzer, J.L. Visher, and S.M. Wandzura. Scalable electromagnetic scattering calculations on the SGI Origin 2000. In *Proceedings of the 1999 ACM/IEEE conference on Supercomputing*, page 54, nov. 1999.

[PC04] Y. C. Pan and W. C. Chew. A fast multipole method for embedded structure in a stratified medium. *Progress In Electromagnetics Research*, 44:1–38, 2004.

[PPY+12] Xiao-Min Pan, Wei-Chao Pi, Ming-Lin Yang, Zhen Peng, and Xin-Qing Sheng. Solving problems with over one billion unknowns by the MLFMA. *Antennas and Propagation, IEEE Transactions on*, 60(5):2571 –2574, may 2012.

[PW97] J.R. Phillips and J.K. White. A precorrected-fft method for electrostatic analysis of complicated 3-d structures. *Computer-Aided Design of Integrated Circuits and Systems, IEEE Transactions on*, 16(10):1059–1072, Oct 1997.

[QC08] Zhi-Guo Qian and Weng Cho Chew. Packaging modeling using fast broadband surface integral equation method. In *Electrical Performance of Electronic Packaging, 2008 IEEE-EPEP*, pages 347–350, 2008.

[Rok90] V Rokhlin. Rapid solution of integral equations of scattering theory in two dimensions. *Journal of Computational Physics*, 86(2):414 – 439, 1990.

[Rok93] V. Rokhlin. Diagonal forms of translation operators for the helmholtz equation in three dimensions. *Applied and Computational Harmonic Analysis*, 1(1):82 – 93, 1993.

[RUP01] J.M. Rius, E. Ubeda, and J. Parron. On the testing of the magnetic field integral equation with rwg basis functions in method of moments. *Antennas and Propagation, IEEE Transactions on*, 49(11):1550–1553, 2001.

[RWG82] S.M. Rao, D. Wilton, and A.W. Glisson. Electromagnetic scattering by surfaces of arbitrary shape. *Antennas and Propagation, IEEE Transactions on*, 30(3):409–418, 1982.

[SAG11] R. Speck, L. Arnold, and P. Gibbon. Towards a petascale tree code: Scaling and efficiency of the PEPC library. *Journal of Computational Science*, 2(2):138 – 143, 2011.

[Sar03] Jukka Sarvas. Performing interpolation and anterpolation entirely by fast fourier transform in the 3-D multilevel fast multi-

pole algorithm. *SIAM J. Numer. Anal.*, 41(6):2180–2196, June 2003.

[SC95] J.M. Song and W.C. Chew. Multilevel fast-multipole algorithm for solving combined field integral equations of electromagnetic scattering. *Microwave and Optical Technology Letters*, 10(1):14–19, Sept. 1995.

[SC00] J.M. Song and W.C. Chew. Large scale computations using FISC. In *Antennas and Propagation Society International Symposium, 2000. IEEE*, volume 4, pages 1856 –1859 vol.4, 2000.

[SC01] Jiming Song and Weng Cho Chew. Interpolation of translation matrix in MLFMA. *Microwave and Optical Technology Letters*, 30(2):109–114, 2001.

[SH07] B. Shanker and H. Huang. Accelerated cartesian expansions - a fast method for computing of potentials of the form r^v for all real v. *Journal of Computational Physics*, 226(1):732–753, 2007. cited By (since 1996) 14.

[SKS+88] A. Seidl, H. Klose, M. Svoboda, J. Oberndorfer, and W. Rosner. Capcal-a 3-d capacitance solver for support of cad systems. *Computer-Aided Design of Integrated Circuits and Systems, IEEE Transactions on*, 7(5):549–556, 1988.

[SL91] K. E. Schmidt and Michael A. Lee. Implementing the fast multipole method in three dimensions. *Journal of Statistical Physics*, 63:1223–1235, 1991. 10.1007/BF01030008.

[SLCM13] Sheng Sun, Y.G. Liu, Weng Cho Chew, and Zuhui Ma. Calderon multiplicative preconditioned efie with perturbation method. *Antennas and Propagation, IEEE Transactions on*, 61(1):247–255, 2013.

[Ste61] S. Stein. Addition theorems for spherical wave functions. *Quart. Appl. Math.*, 19:15–24, 1961.

[SW94] John K. Salmon and Michael S. Warren. Skeletons from the treecode closet. *Journal of Computational Physics*, 111(1):136 – 155, 1994.

[TG08] Anna-Karin Tornberg and Leslie Greengard. A fast multipole method for the three-dimensional Stokes equations. *J. Comput. Phys.*, 227(3):1613–1619, January 2008.

[TYO06] M. Taskinen and P. Yla-Oijala. Current and charge integral equation formulation. *Antennas and Propagation, IEEE Transactions on*, 54(1):58–67, 2006.

[VC01] Sanjay Velamparambil and Weng Cho Chew. A fast polynomial representation for the translation operators of an MLFMA. *Microwave and Optical Technology Letters*, 28(5):298–303, 2001.

[VC05] S. Velamparambil and W.C. Chew. Analysis and performance of a distributed memory multilevel fast multipole algorithm. *Antennas and Propagation, IEEE Transactions on*, 53(8):2719 – 2727, aug. 2005.

[VCS03] S. Velamparambil, Weng Cho Chew, and Jiming Song. 10 million unknowns: is it that big? [computational electromagnetics]. *Antennas and Propagation Magazine, IEEE*, 45(2):43 –58, april 2003.

[Vec99] G. Vecchi. Loop-star decomposition of basis functions in the discretization of the efie. *Antennas and Propagation, IEEE Transactions on*, 47(2):339–346, 1999.

[VGHS07] M. Vikram, H. Griffith, He Huang, and B. Shanker. Accelerated cartesian harmonics for fast computation of time and frequency domain low-frequency kernels. In *Antennas and Propagation Society International Symposium, 2007 IEEE*, pages 5607 –5610, june 2007.

[VGMO+04] D. Vande Ginste, E. Michielssen, F. Olyslager, D. De Zutter, L. Xuan, A. Zhu, R.J. Adams, and S.D. Gedney. Towards a PML-based MLFMA for planar microwave circuits. In *Antennas and Propagation Society International Symposium, 2004. IEEE*, volume 2, pages 1191 –1194 Vol.2, june 2004.

[VHSV09] M. Vikram, He Huang, B. Shanker, and T. Van. A novel wideband FMM for fast integral equation solution of multiscale problems in electromagnetics. *Antennas and Propagation, IEEE Transactions on*, 57(7):2094 –2104, july 2009.

[VSA09] M. Vikram, B. Shanker, and S. Aluru. Provably scalable parallel FMM algorithm for multiscale electromagnetic simulations. In *Antennas and Propagation Society International Symposium, 2009. APSURSI '09. IEEE*, pages 1 –4, june 2009.

[VSV08] M. Vikram, B. Shanker, and T. Van. Fast solvers for electromagnetic simulation of mixed-scale structures. In *Antennas and Propagation Society International Symposium, 2008. AP-S 2008. IEEE*, pages 1 –4, july 2008.

[WJGHG96] Christopher A. White, Benny G. Johnson, Peter M.W. Gill, and Martin Head-Gordon. Linear scaling density functional calculations via the continuous fast multipole method. *Chemical Physics Letters*, 253(3–4):268 – 278, 1996.

[WPM+02] J. Waltz, G.L. Page, S.D. Milder, J. Wallin, and A. Antunes. A performance comparison of tree data structures for N-body simulation. *Journal of Computational Physics*, 178(1):1 – 14, 2002.

[WS92] Michael S. Warren and John K. Salmon. Astrophysical N-body simulations using hierarchical tree data structures. In *Proceedings of the 1992 ACM/IEEE conference on Supercomputing*, pages 570–576, 1992.

[WS93] M. S. Warren and J. K. Salmon. A parallel hashed oct-tree N-body algorithm. In *Proceedings of the 1993 ACM/IEEE conference on Supercomputing*, pages 12–21, 1993.

[WS05] H. Wallen and J. Sarvas. Translation procedures for broadband MLFMA. *Progress In Electromagnetics Research*, 55:47–78, 2005.

[WSH+12] Mathias Winkel, Robert Speck, Helge Hübner, Lukas Arnold, Rolf Krause, and Paul Gibbon. A massively parallel, multi-disciplinary barnes-hut tree code for extreme-scale N-body simulations. *Computer Physics Communications*, 183(4):880 – 889, 2012.

[XZAG04] L. Xuan, A. Zhu, R. J. Adams, and S. D. Gedney. A broadband multilevel fast multipole algorithm. In *Proceedings of the IEEE AP-S International Symposium and USNC/URSI National Radio Science Meeting*, volume 2, pages 1195–1198, 2004.

[YBZ04] Lexing Ying, George Biros, and Denis Zorin. A kernel-independent adaptive fast multipole algorithm in two and three dimensions. *J. Comput. Phys.*, 196(2):591–626, May 2004.

[YJN10] Su Yan, Jian-Ming Jin, and Zaiping Nie. Efie analysis of low-frequency problems with loop-star decomposition and calderon

multiplicative preconditioner. *Antennas and Propagation, IEEE Transactions on*, 58(3):857–867, 2010.

[YR98] N. Yarvin and V. Rokhlin. Generalized gaussian quadratures and singular value decompositions of integral operators. *SIAM J. Sci. Comput.*, 20(2):699–718, December 1998.

[YR99] Norman Yarvin and Vladimir Rokhlin. An improved fast multipole algorithm for potential fields on the line. *SIAM J. Numer. Anal.*, 36(2):629–666, February 1999.

[ZCCZ03] Yunhua Zhang, Tie-Jun Cui, Weng Cho Chew, and Jun-Sheng Zhao. Magnetic field integral equation at very low frequencies. *Antennas and Propagation, IEEE Transactions on*, 51(8):1864–1871, 2003.